Institut für Festkörperphysik

FRIEDRICH-SCHILLER-UNIVERSITÄT JENA

Annual Report 2007

Institut für Festkörperphysik

Friedrich-Schiller-Universität Jena

Annual Report 2007

Editors: Prof. Dr. Paul Seidel
Dr. Christian Hülsen
Uta Bornkessel

Institut für Festkörperphysik
Friedrich-Schiller-Universität Jena
Max-Wien-Platz 1
D-07743 JENA

Tel.:   +49 (0) 3641 / 947301, 947411
Fax: +49 (0) 3641 / 947412, 947302
e-mail: Paul.Seidel@uni-jena.de
home page: http://www.physik.uni-jena.de/exp_phys/

Prof. Dr. Paul Seidel   Tel.:   +49 (0) 3641 / 947410, 947411
director   Fax: +49 (0) 3641 / 947412
                               e-mail: Paul.Seidel@uni-jena.de
                               home page: http://www.physik.uni-jena.de/~tief

Prof. Dr. Wolfgang Richter   Tel.:   +49 (0) 3641 / 947440, 947411
                               Fax: +49 (0) 3641 / 947442
                               e-mail: Wolfgang.Richter@uni-jena.de
                               home page: http://www.physik.uni-jena.de/~layer/

Prof. Dr. Werner Wesch   Tel.:   +49 (0) 3641 / 947330, 947301
                               Fax: +49 (0) 3641 / 947302
                               e-mail: Werner.Wesch@uni-jena.de
                               home page: http://www.physik.uni-jena.de/~exphys/

Prof. Dr. Wolfgang Witthuhn   Tel.:   +49 (0) 3641 / 947309, 947301
                               Fax: +49 (0) 3641 / 947302
                               e-mail: Wolfgang.Witthuhn@uni-jena.de
                               home page: http://www.physik.uni-jena.de/~exphys/

Prof. Dr. Friedrich Huisken   Tel.:   +49 (0) 3641 / 947354, 947301
                               Fax: +49 (0) 3641 947308
                               e-mail: Friedrich.Huisken@uni-jena.de
                               home page: http://www.physik.uni-jena.de/~exphys/astrolab/

Preface

Since 1996 there is the annual report of the Institute of Solid-State Physics at the Friedrich Schiller University Jena. The research and teaching activities achieved in 2007 will be summarized in this issue. As the preceding reports it again is addressed to the interested scientific community and to our colleagues within the university and from outside. We also document the use of the financial support and we would like to take the opportunity to thank all institutions for this support.

The research topics of the IFK cover different fields of solid state physics and range from fundamental questions to largely applied developments. The nuclear solid state physics groups employ electrical, optical and nuclear physics methods based on radioactive isotopes as well as ion beam techniques. The investigations are concentrated on semiconductors and optical materials. Research activities on chalcopyrit-semiconductors for thin film solar cells and optoelectronic devices are performed in the CIS-lab of the institute. In the low temperature department essentially high-T_c superconducting layers and superconducting devices like SQUIDs are studied and applied. This includes the cooling technology with self made cryocoolers as well as ultra-low temperature research. The SFB/TR7 "Gravitational wave astronomy" investigated within the last years optical components at low temperatures, too. Thin films of SiC, III-nitrides and III-arsenides are deposited by molecular beam epitaxy and are characterized by a variety of surface physics methods in the thin solid films group. As a common interest within our institute investigations on carbon and silicon nanotubes were forced within the last years. The research group on laboratory astrophysics/cluster physics is devoted to fundamental astrophysical questions that can be answered by laboratory experiments, with particular emphasis on spectroscopy.

The permanent scientific staff of the IFK is strongly involved in teaching duties. The modularisation of the physics courses and the new bachelor and master studies instead of the physics diploma give rise to strong enhancement of effort but also the chance of a new quality. The solid state physics in combination with the materials science will play an important role within this education. As an important activity the institute took part in the "Long night og sciences" where about 1000 people visit the lectures and laboratories.

Prof. W. Witthuhn was retired and we like to thank him because he determined the profile of the institute during the last years. 2007 was also the last active year of Prof. W. Richter, and we like to thank him for his excellent work since the foundation of the IFK.

In 2007 Prof. W. Wesch was appointed to the international Materials Research Program Advisory Committee (MAT-PAC) at the Gesellschaft für Schwerionenforschung (GSI) Darmstadt. PD Dr. F. Schmidl obtained a call for a professorship at the FH Jena but finally remained in our institute.

Many institutions contributed to the scientific output of the institute. The activities would be impossible without substantial financial support - equipment as well as additional scientific and technical staff - by: Thüringer Kultusministerium (TKM), Bundesministerium für Bildung und Forschung (BMBF), Bundesministerium für Wirtschaft und Technologie (BMWi), Bundesministerium für Umwelt, Naturschutz und Reaktorsicherheit (BMU), Deutsche Forschungsgemeinschaft (DFG), Europäische Gemeinschaft (EU), Nagelschneider-Stiftung, Hahn-Meitner-Institut Berlin, industrial partners and - last but not least- the Friedrich-Schiller-Universität. We express our gratitude to all these institutions.
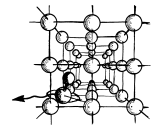
Prof. Dr. Paul Seidel

Contents

Departments of the institute

Solid State Physics

Prof. Dr. W. Witthuhn

- Structure and dynamics of impurities, defect-clusters and nanocrystals in semiconductors
- Preparation and characterization of heterogeneous thin layers for optoelectronic and photovoltaic devices; thin-film solarcells
- 3D-microstructures and material modifications by energetic ion beams

---

- The research of the *solid state-/semiconductor-physics* group is directed to three different fields:

- Investigation of structure and dynamics of local perturbations and internal fields in solid states with emphasis on atomic and electronic structures of deep intrinsic and impurity-related levels in wide-band-gap compound semiconductors. The research is part of the "Verbundforschungs-Programm" of the German BMBF, carried out at large research centres (like ISOLDE/CERN or HMI, Berlin). There exist a close cooperation with research groups at Berlin (HMI), Genf (ISOLDE/CERN), Universities at Konstanz, Saarbrücken, Freiberg, and Bonn. Furthermore, cooperations exist with the University of Oslo, Norway, and the Paul-Scherrer-Institute, Villingen, Switzerland.

- Formation and characterisation of buried metallic and/or ferromagnetic nanocrystals in wide-band-gap semiconductors for applications in optoelectronics and spintronics. Cooperation exists with groups at the Jena IPHT, the Technical University Ilmenau, the Technical University Dresden, University Ulm, University of Pittsbourgh, and the Cornell University, USA.

- Growth and characterisation of single- and polycrystalline thin layers of chalcopyrit-based semiconductors for optoelectronic and photovoltaic applications. Processing of complete solar-cells with emphasis on the systems [Cu(In,Ga)(S$_2$,Se$_2$)] and CdTe/CdS. Hetero-layers for applications in future high-efficient solar-cells. The research on CdTe/CdS-thin-film solar-cells is performed in close cooperation with the industrial partner "Antec-Solar Energy" at Rudisleben/Arnstadt. The IFK-group is member of the Thuringian "Solar Input" e.V. and of the German "PV-Uni-Netz", in which 12 German universities coordinate their research on photovoltaics.
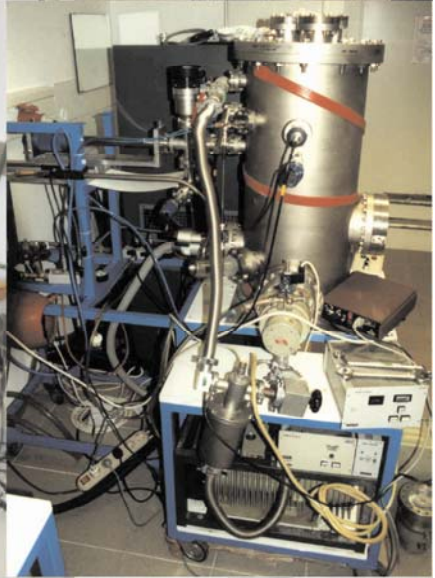
Ion Beam Physics
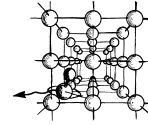
Prof. Dr. W. Wesch
- Modification of solid layers by ion implantation and succeeding processes and ion beam analysis (RBS, PIXE, ERD, NRA)
- Ion beam synthesis of buried nanostructures
- Investigation of the effect of high electronic excitation on structural midification of crystalline and amorphous semiconductors
- Simulation of processes of ion-solid interaction

The *Ion Beam Physics* Group deals with problems of modification of solids and synthesis of buried nanostructures by means of ion beams and combined secondary processes. The studies cover fundamental processes of ion-beam induced structural modification in new semiconductors and insulators being relevant for future electronic, optoelectronic and photonic device technologies, as e.g. ternary III-V semiconductors wide gap semiconductors and isolators (collaborations with the Australian National University Canberra, the University of Pretoria, South Africa and the University Lisboa, Portugal). The structural changes in AlGaAs and Si caused by ion irradiation are also investigated by classical molecular dynamics computer simulations. At the same time the formation of ferromagnetic nanocrystals and layers in Si and GaAs by ion-beam induced non-equilibrium processes (collaboration with the University Aveiro, Portugal) and the specific modification of optical materials as $LiNbO_3$ and $KTiOPO_4$ as well as ion beam enhanced chemical etching to produce high aspect ratio microstructures for optical application of these materials (collaboration with the Institute of Applied Physics, Jena) are studied.

Beside these activities on materials modification utilizing ion beams with conventional energies (several 10 keV to several MeV), the effect of high electronic excitation under swift heavy ion irradiation (several 100 MeV) on structural modification of crystalline semiconductors (ion track formation) as well as on plastic deformation in amorphous semiconductors is studied (collaboration with the Hahn-Meitner-Institute Berlin, Australian National University Canberra).

Low Temperature Physics

Prof. Dr. P. Seidel

- Superconductivity within thin layers and layer systems
- Josephson effects, proximity effect, tunnel effects and quantum effects in superconducting devices
- DC-SQUID's and their application in measurement, e.g. biomagnetism, NDE, MRX
- cryogenic measurements on optical components (mechanical quality factor)
- Dynamics of superconducting Josephsonarrays and qubits
- cryogenic engineering (cryocoolers, cryogenic storage)

The *low temperature physics* group works on the following fields:
- preparation, characterization, modelling and application of Josephson junctions and SQUIDs (precision and magnetorelaxation measurements with LTS SQUIDs, non-destructive evaluation and biomagnetism with HTS SQUIDs, intrinsic Josephson junctions)
- low temperature physics and cryogenic engineering (development of new kinds of pulse tube cryocoolers, investigations on a new concept for regenerators, cryogenic storage)
- experimental work within the SFB/TR on cryogenic measurements of the Q-factor of optical components including grating optics
- thin film technologies for insulators and other materials

The research is carried out in cooperations with other research groups in Thuringia (TU Ilmenau, IPHT Jena, SQUID GmbH Jena, SUPRACON Jena, Polyoptik Bad Blankenburg, Innovent e.V. Jena). Within common activities the group works together with the Gesellschaft für Schwerionenforschung Darmstadt, DESY Hamburg, TARGET Systemelectronic GmbH Solingen and the Zentrum für Raumfahrttechnologie und Mikrogravitation Bremen.

With industrial partners there exist some resarch activies e.g. with Air Liquide (France), Northrop Gruman (USA), AEG Infrared Moduls GmbH Heilbronn and the TransMIT center for adaptive cryotechniques Gießen. A long tradition of cooperation exists with the Institute of Electrical Engineering (IEE) of the Slovak Academy of Sciences Bratislava, the Universities of Moscow (Russia), Kharkov (Ukraine), Glasgow (U.K.) and Vienna (Austria), the Tohoku University Sendai and the University of Osaka (both in Japan).

Paul Seidel

Vortrag am 16.11.2007 zur „Langen Nacht der Wissenschaften"
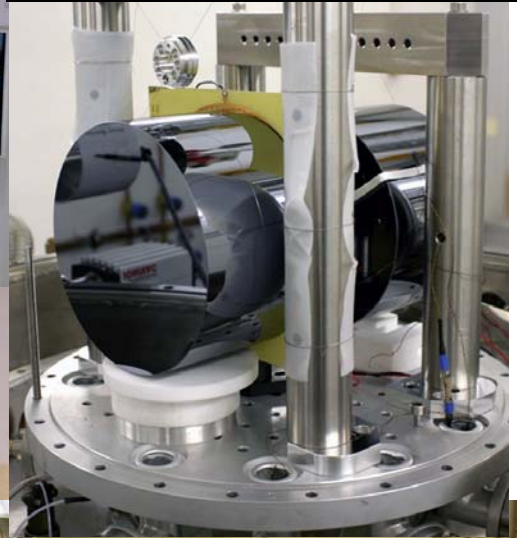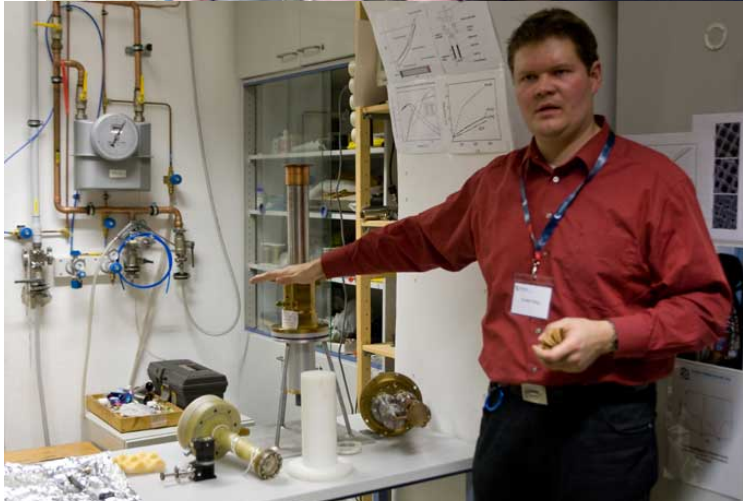
Physics of Thin Films
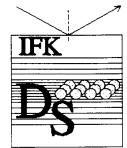
Prof. Dr. W. Richter
- Deposition of thin films of semiconductors and of metallic nanoparticles using molecular beams at ultrahigh vacuum conditions
- Chemical vapor deposition of carbon nanotubes
- Growth of graphene and carbon nanotubes on silicon carbide
- Epitaxy of GaAs-based III-V compounds
- Analyses of surfaces, layers and nanostructures using AES, XPS, LEED, RHEED, XPD, STM, AFM, and SEM

The group „**Physics of thin films**" at the institute of solid-state physics is engaged in the research on nanostructures, solid surfaces and thin films of semiconductor materials like silicon carbide and gallium aluminum arsenide as well as on carbon nanotubes and organic molecules on semiconductor surfaces.

For analyses of the chemical composition and bonding at surfaces and in thin films we use surface analysis methods like photoelectron spectroscopy (XPS, UPS) and Auger electron spectroscopy (AES). The crystalline structure can be determined by electron diffraction (LEED, XPD, and electron channeling). Scanning tunneling microscopy (STM), atomic force microscopy (AFM) and scanning electron microscopy (SEM) are used for high-resolution imaging of nanostructures and surfaces.

Molecular beam epitaxy (MBE) in ultra-high vacuum (UHV) is the preferred technique to grow nanostructures and semiconductor heterostructures (Si, Ge, SiC, GaAs, AlAs, and In-GaAs) for electronic and optoelectronic applications. Our particular interest is to understand and to control the impact of the substrate surface preparation and of the growth conditions on the structure and the properties of thin films and nanostructures.

Carbon nanotubes have been produced on solid substrates by chemical vapour deposition (CVD) using methane and ethanol as precursor gas. Metallic nanoparticles acting as catalyst have been prepared by physical vapor deposition of Fe, Co or Ni in UHV utilizing our in-situ surface characterization methods.

Extensive characterization of the CVD samples by SEM, AFM and Raman spectroscopy revealed high-quality single-wall carbon nanotubes of diameters between 1 and 2 nm. The amount of residual catalyst and amorphous carbon species has been determined to be very low. Post-growth purification techniques like heating in vacuum, in air or in hydrogen atmosphere could further improve the nanotube material. Successful experiments to functionalize nanotubes by organic molecules have been the first step to investigations on future biochemical sensors.

Our long-time experience in silicon carbide research has been used to grow graphene as well as carbon nanotubes on single-crystalline SiC substrates.

The carbon nanotube research is strongly supported by the cooperation with the Astrophysics Institute, the Institute of Applied Physics and the Institute of Photonic Technologies.

Friedrich-Schiller-Universität Jena

Institut für Festkörperphysik
AG Physik Dünner Schichten

IFK
AG
Dünne
Schichten
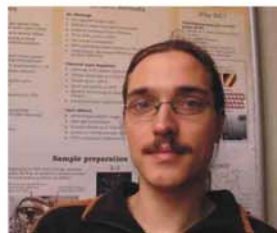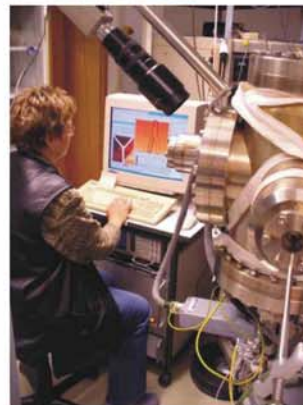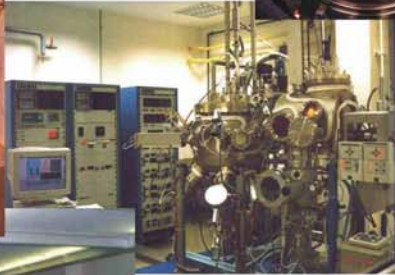
Laboratory Astrophysics/Cluster Physics

Prof. Dr. F. Huisken
- Cavity ring-down spectroscopy of neutral and ionized polycyclic aromatic hydrocarbons in supersonic jets
- UV spectroscopy of polycyclic aromatic hydrocarbons (PAHs) embedded in liquid helium nanodroplets
- Photoluminescence studies of silicon nanocrystals produced by CO_2 laser pyrolysis and Si ion implantation

The Joint *Laboratory Astrophysics/Cluster Physics* Group at the Institute of Solid State Physics results from a cooperation between the Max-Planck-Institute for Astronomy, Heidelberg, and the Friedrich-Schiller-University, Jena. Inaugurated in February 2003, it is conducted by Prof. Dr. Thomas Henning and Prof. Dr. Friedrich Huisken.

The research of the Joint Laboratory Astrophysics and Cluster Physics Group is devoted to fundamental astrophysical questions that can be answered by laboratory experiments, with particular emphasis on spectroscopy. The electromagnetic radiation reaching us from stellar objects is modified in a characteristic manner by interstellar molecules and dust particles. Many of these "fingerprints" are still far from being understood. In order to determine the species causing the modification of the electromagnetic signals detected by telescopes and satellites, comprehensive laboratory studies are urgently needed.

The laboratory is equipped with modern molecular and cluster beam machines as well as laser systems to contribute to the clarification of such fundamental questions. For this purpose, the molecules, clusters, and nanoparticles of interest are prepared in vacuum chambers under conditions coming close to those encountered in the interstellar space (low temperature and low density).
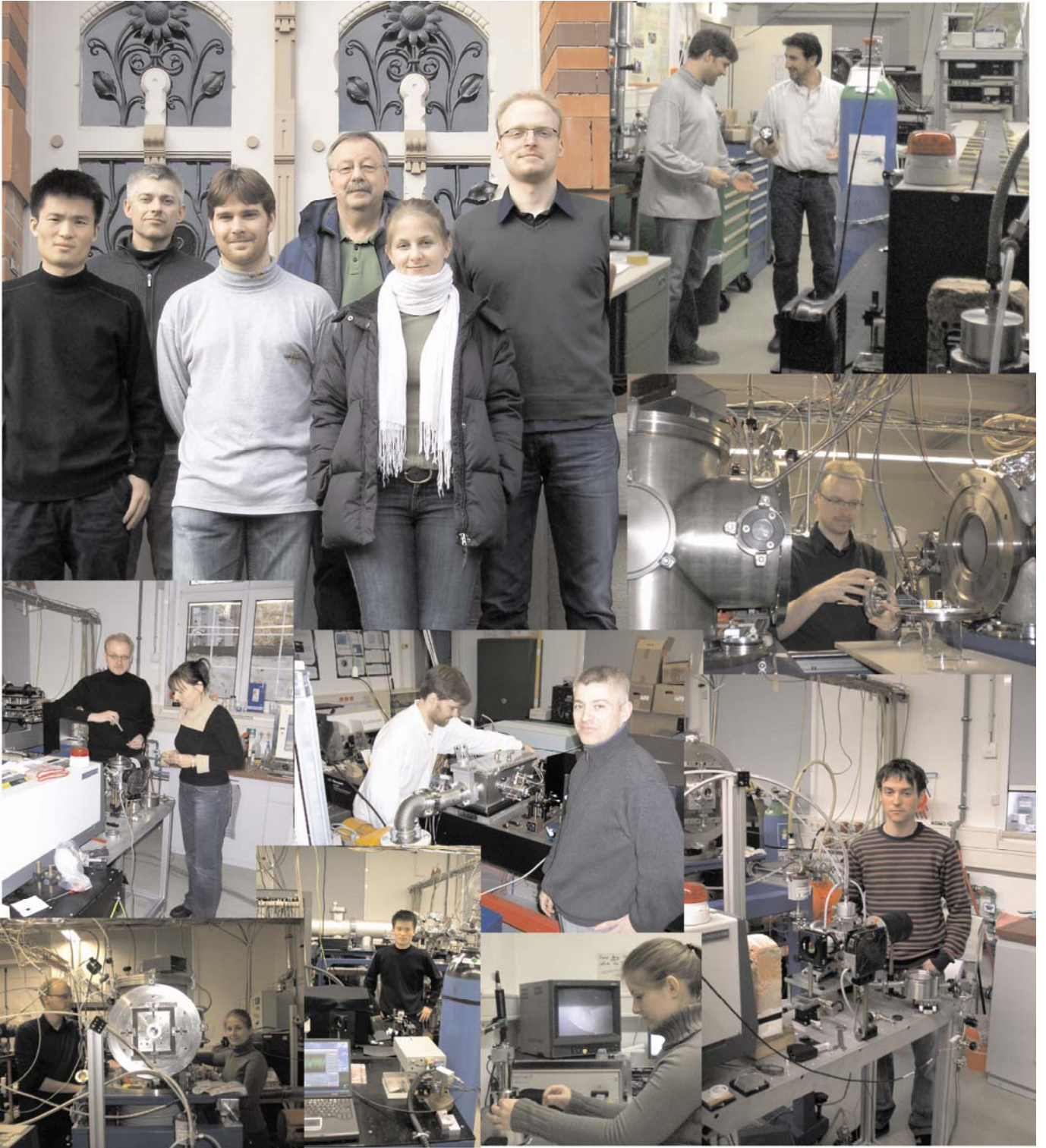
Structural modification of swift heavy ion irradiated amorphous Ge layers

W. Wesch, C.S. Schnohr*, P. Kluth*, Z.S. Hussain[*], L.L. Araujo[*], R. Giulian[*], D.J. Sprouster[*], A.P. Byrne*, M.C. Ridgway*

[*]Australian National University, Department of Electronic Materials Engineering

We have previously shown that swift heavy ion irradiation of amorphous Si layers at 80 K and oblique incidence results in plastic deformation as a consequence of the high electronic energy deposition. The results clearly illustrate that amorphous Si behaves like conventional glasses /1,2/. Room temperature irradiation at higher fluences additionally yields a remarkable swelling due to the formation of voids subsequently resulting in a porous structure at still higher fluences. To study the effect of high electronic energy deposition on amorphous Ge layers for which no data existed, crystalline Ge wafers were amorphised at the 1.7 MV accelerator of the Department of Electronic Materials Engineering of the Australian National University (ANU). The implantation of Ge ions with energies ranging from 80 keV to 6.7 MeV and ion fluences of 4.9×10^{13} cm^{-2} to 2.8×10^{14} cm^{-2} at 80 K resulted in the formation of a homogeneous amorphous layer with a thickness of 3.2 μm. The amorphised samples were then irradiated with 185 MeV Au ions at the (14 UD) Heavy-Ion Accelerator Facility of the ANU. The irradiations were performed at room temperature and an angle of incidence of 45° with respect to the surface normal. The Au ion fluence was varied between 3×10^{13} cm^{-2} and 7×10^{14} cm^{-2}. The irradiated samples were analysed by surface profilometry and scanning electron microscopy (SEM).

In Fig. 1 the depth dependencies of electronic and nuclear energy deposition, S_e and S_n, per ion and unit length as calculated with the SRIM-2003.26 /3/ code are depicted. The electronic energy loss near the surface clearly dominates the nuclear component (by approximately three orders of magnitude).
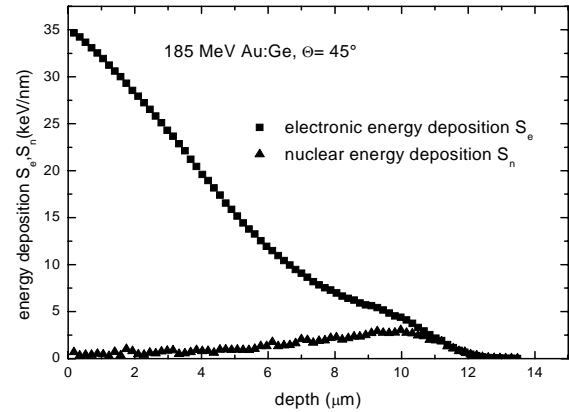
Fig. 1: Electronic and nuclear energy deposition per ion and unit length.
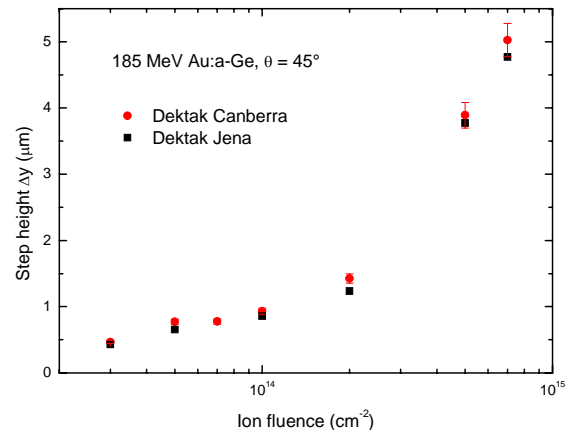
Fig. 2: Swelling of Au irradiated amorphous Ge as a function of the Au ion fluence.

Subsequent to irradiation, a change in sample surface colour from light brown to black with increasing ion fluence was readily apparent. The change of colour was accompanied with swelling of the amorphous layer, the latter also increasing with ion fluence. This is illustrated in Fig. 2 which shows the step height as a function of ion fluence. SEM measurements established that the swelling was a consequence of void formation within the amorphous layer, which transformed into a sponge-like porous structure at higher ion fluences. Figs. 3 and 4 show, as examples, SEM images of the cross section of two

samples irradiated with 3×10^{13} Au cm^{-2} and 2×10^{14} Au cm^{-2}, respectively.
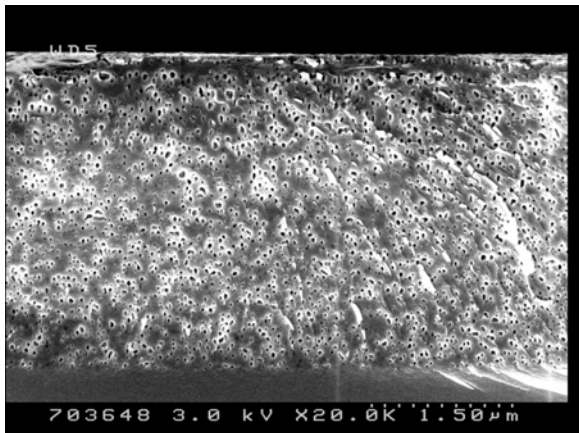
Fig. 3: Cross-section SEM image of a sample irradiated with 3×10^{13} Au cm^{-2}.
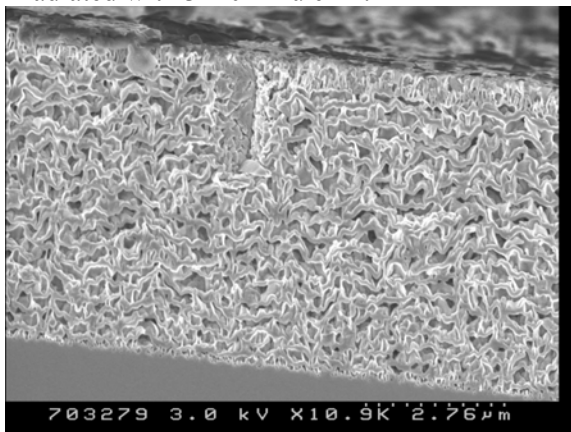
Fig. 4: Cross section SEM image of a sample irradiated with 2×10^{14} Au cm^{-2}.

Whereas the formation of porous structures in Ge in the nuclear energy deposition regime has been previously demonstrated, the amorphous-to-porous transformation due to high electronic energy deposition is shown here for the first time.

/1/ A. Hedler, S. Klaumünzer, W. Wesch, Nature Materials 3 (2004) 804
/2/ A. Hedler, S. Klaumünzer, W. Wesch, Annual Reports 2004, 2005
/3/ J.F. Ziegler, J.P. Biersack,U. Littmark, The Stopping and Ranges of Ions in Solids, Pergamon, New York, 2003

Interaction potential for fast Ne atoms in front of LiF(001) surface

A. Schüller*, K. Gärtner and H. Winter*

*Institut für Physik, Humboldt Universität zu Berlin

Fast neutral Ne atoms with energies E_0 (~ keV) are scattered under a grazing angle of incidence Φ_{in} from a flat and clean LiF(001) surface (seeFig.1.) For scattering
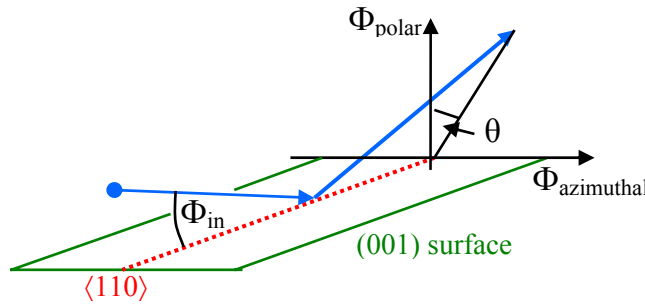
Fig.1. Scattering geometry

along a low index direction (axial surface channeling, $\langle 110 \rangle$ in Fig.1), pronounced peaks in the two-dimensional angular distribution (Φ_{polar}, $\Phi_{azimuthal}$) of the scattered projectiles are observed. This is due to rainbow scattering as e.g. explained in Ref.[1]. For the example of 25 keV Ne atoms with Φ_{in} = 1.2 deg, the distribution of the scattered Ne atoms is shown in Fig.2.
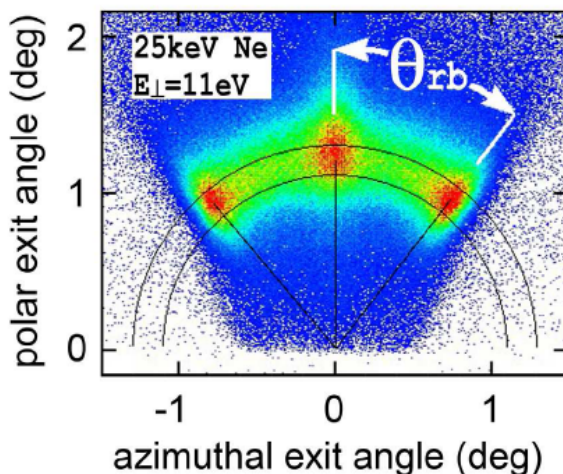
Fig.2. 2D plot of the angular distribution of the scattered Ne atoms (E_0 = 25 keV, Φ_{in} = 1.2 deg, red/blue: high/low intensity)

There is a peak (red) at $\Phi_{azimuthal}$ = 0 and two outer peaks (red) all positioned on a circle. The position θ (see Fig.1) of one of the outer peaks is called rainbow angle θ_{rb} (see Fig.2).

The dependence of the rainbow angle θ_{rb} on the energy E_0 and angle of incidence Φ_{in} of the Ne atom has been investigated experimentally for energies E_0 from 3 keV to 70 keV and for angles Φ_{in} from 0.5 deg to 2.0 deg. The results show that in a very good approximation θ_{rb} depends only on the transverse energy $E_\perp = E_0 \sin^2\Phi_{in}$ and not on E_0 and Φ_{in} separately. For two surface channeling directions $\langle 110 \rangle$ and $\langle 100 \rangle$ the results are presented in Fig.3 by the symbols. As can be seen, the rainbow angles θ_{rb} measured for different energies lay on one line when depicted as a function of the transverse energy $E_\perp$. For small transverse energies up to about 10 eV, θ_{rb} increases rapidly and for higher $E_\perp$ the slope becomes smaller. Therefore, the low $E_\perp$ regions are zoomed and shown in addition in the left parts of Fig.3.

For the calculation of the rainbow angle θ_{rb}, the interaction of the Ne atom with the LiF(001) surface can be approximated by the sum of the interatomic interaction potentials of the Ne atom with all Li and F atoms (or ions) of the LiF surface, averaged along the surface channeling direction. This requires the interatomic He-Li and He-F potentials. Using the frequently applied generalized ZBL potential [2] or OCB potential [3] the results do not agree with experimental data (see Fig.3) which means that a generalized potential cannot be used. Therefore, the He-Li and He-F potentials were calculated individually (individual potentials) according to the procedure given in Ref.[4]. As can be seen in Fig.3, the results obtained with the individual potential for
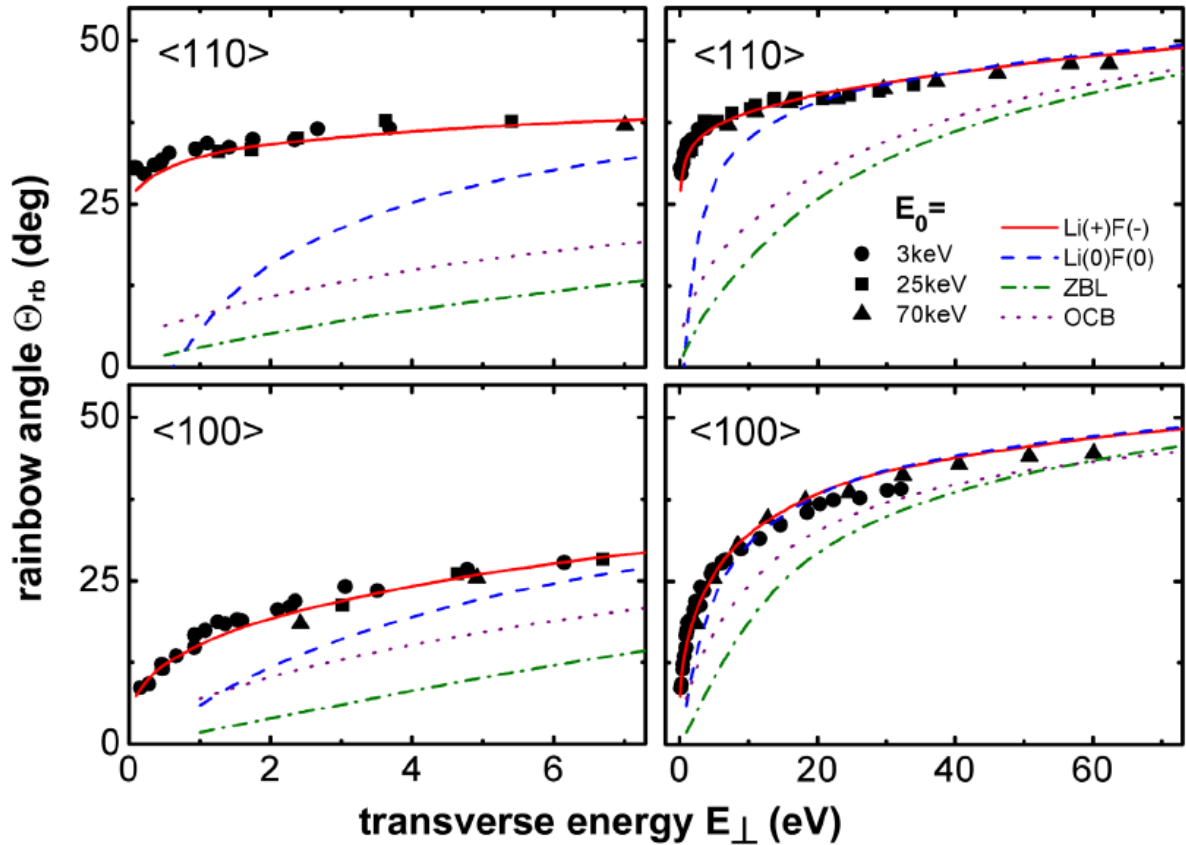
Fig.3. The rainbow angle θ_{rb} as function of the transverse energy $E_\perp$ for the surface channeling directions $\langle 110 \rangle$ and $\langle 100 \rangle$. The symbols represent the experimental data and the lines give the theoretical results obtained with different potentials (see text, left sides: focus on low $E_\perp$ regions)

the interaction of the He atom with neutral Li and F atoms (blue dashed line) provide good results for $E_\perp > 20$ eV but they show still remarkable deviations for $E_\perp < 20$ eV. However, using the individual potentials for the interaction of neutral He atoms with **Li$^+$ and F$^-$ ions** (red line), an excellent overall agreement with the experimental data is achieved. This shows that the experimental results can only be understood by taking into account the ionic nature of the LiF crystal and the individual electronic structure of the Ne atom and the Li$^+$ and F$^-$ ions.

[1] D.M. Danailov, R. Pfandzelter, T. Igel, H.Winter, and K. Gärtner, Appl. Surf. Sci.171 (2001)113.
[2] J.F. Ziegler, J.P. Biersack, and U. Littmark, The Stopping and Range of Ions in Solids, Vol. I, Pergamon Press, New York 1985.
[3] D.J. O'Connor and J.P. Biersack Nucl. Instrum. Meth. B15 (1986)14.
[4] K. Gärtner, K. Hehl, Phys. Stat. Sol. (B) 94{1979)231.

Ion beam induced effects at 15 K in LiNbO₃

Th. Gischkat, F. Schrempel, W. Wesch

To study the primary effects of damage production and accumulation in LiNbO₃, experiments have to be carried out at very low temperatures to avoid thermally induced annealing of defects. However investigations of the defect formation in sapphire at 15 K showed damage annealing during the Rutherford backscattering spectrometry (RBS) [1]. This was explained by the electronic energy deposition of the analyzing He-ions. Similar annealing effects due to the measurement may also occur in other insulators like LiNbO₃. Therefore, a careful study of the influence of the analyzing He-beam on the defect concentration to be measured was performed. In order to study the He-beam induced effects on damage formation in LiNbO₃, z-cut samples were irradiated with various ion species at 15 K and subsequently investigated stepwise in portions of equal He fluence providing a series of sub-spectra.

Commercial optical grade z-cut LiNbO₃ crystals were irradiated with 30 keV H-, 50 keV Li-, 160 keV O- and 350 keV Ar-ions at 15 K. The ion energies were chosen in such a way that the maximum of the damage distribution for each ion species is expected at a depth of about 200 nm. The analysis of the defect formation was done by means of RBS-measurements in channeling configuration using 1.4 MeV He-ions. All experiments were performed in a double beam target chamber allowing a stepwise irradiation and RBS-measurement at 15 K without changing the temperature of the sample.

From the Nb-part of the RBS spectra the difference in minimum yield $\Delta\chi_{min} = (Y_{al,dam} - Y_{al,perf})/Y_{ra}$ was taken as a measure for the amount of damage produced nearly corresponding to the relative defect concentration. $Y_{al,dam}$ and $Y_{al,perf}$ are the backscattering yield in channeling direction for the perfect and the damaged crystal, respectively, and Y_{ra} is the yield measured in random direction.

It was found, that the minimum yields decrease with increasing number of sub-spectra. The reduction of $\Delta\chi_{min}^{subspectra}$ was fitted by an exponential function which gives the undisturbed difference in minimum yield $\Delta\chi_{min}^{sim}$ and the annealed value $\Delta\chi_{min}^{ann}$ (for details see [2]). The RBS-induced annealed fraction $\delta^{ann} = \Delta\chi_{min}^{sim} - \Delta\chi_{min}^{ann} / \Delta\chi_{min}^{sim}$ was calculated and describes the percentage by which the initial value $\Delta\chi_{min}^{sim}$ is reduced to the annealed value $\Delta\chi_{min}^{ann}$. The calculated values of δ^{ann} are shown in Fig. 1 as a function $\Delta\chi_{min}^{sim}$ for the irradiation with H-, Li-, O- and Ar-ions. The amount of annealing depends on the concentration of defects formed after irradiation and, additionally, on chemical effects in the case of H- and Li-ions.

The fluence dependence of $\Delta\chi_{min}$ was described by an analytical formula which consists of two coupled differential equations
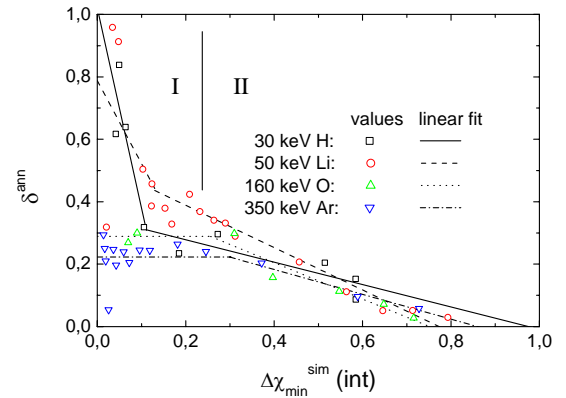
Fig. 1: RBS-induced annealing fraction δ^{ann} versus the undisturbed difference in minimum yield $\Delta\chi_{min}^{sim}$ obtained from the exponential decay for the irradiation with 30 keV H-, 50 keV Li-, 160 keV O- and 350 keV Ar-ions. The linear fits for the calculated values are also included.

with a set of free parameters. For the determination of the undisturbed fluence dependence of the damage accumulation the He-beam induced annealing was taken into account using a special simulation procedure. The free parameters of the analytical formula were chosen in such a way that the calculated reduced values for the full He-

charge agree with the measured experimental values.
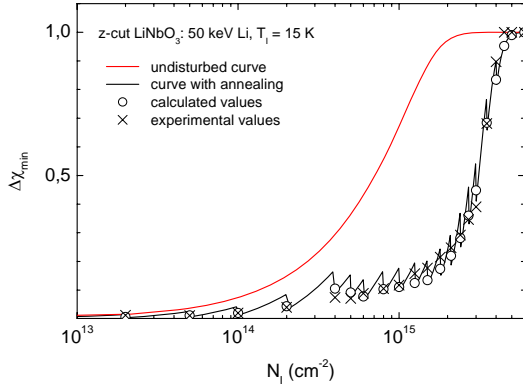
Fig. 2: Undisturbed fluence dependence of $\Delta\chi_{min}$ (dashed line) after the simulation procedure for the irradiation with 50 keV Li-ions. The curve with annealing (solid line), the calculated values (circle) and the experimental values (cross) are also included.

As an example, in Fig. 2 the undisturbed fluence dependence (red line) and the fluence dependence of the damage accumulation with He-beam induced defect annealing (black line) are shown for the irradiation with 50 keV Li-ions. For low ion fluences the gap between the undisturbed curve and the curve influenced by the He-beam induced defect annealing is small but adds up to a significant deviation with increasing ion fluence. As a consequence, without any influence of the He-beam during the measurement the amorphisation fluence for the irradiation of $LiNbO_3$ with 50 keV Li-ions is about 3×10^{15} cm^{-2} which is significantly lower than that obtained from the experimental data (4.5×10^{15} cm^{-2}).

In Fig. 3 the undisturbed fluence dependences of $\Delta\chi_{min}$ are summarized for the irradiation with H-, Li-, O- and Ar-ions at 15 K. For normalized ion fluences below 0.03 dpa the defect concentration increases almost linearly with increasing fluence due to the production of isolated point defects. Normally light ions produce the same or less defects compared to the irradiation with heavier ions but in the case of H and Li the defect concentration for a given ion fluence is higher. Therefore it is expected that chemical reactions between these implants and the host atoms of $LiNbO_3$ influence the defect formation and lead to a higher back-

scattering yield in contrast to the point defects produced by the irradiation with O- and Ar-ions. For normalized ion fluences above 0.03 dpa the defect concentration increases drastically with increasing ion fluence indicating the growth of amorphous
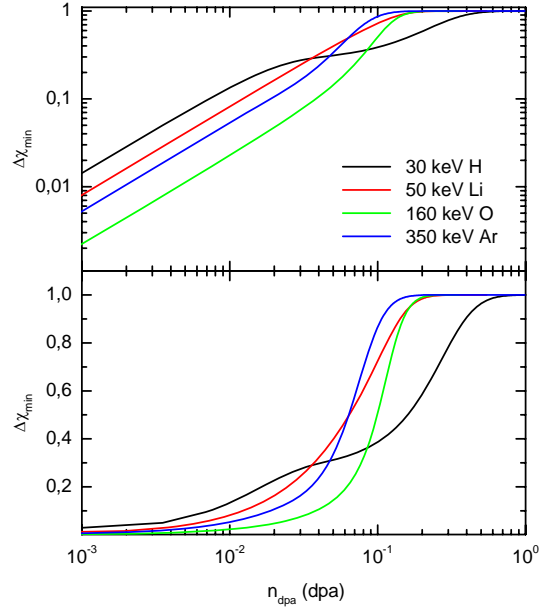
Fig. 3: Results of the undisturbed fluence dependence of $\Delta\chi_{min}$ versus the normalized ion fluence n_{dpa} for the irradiation with H-, Li-, O- and Ar-ions. For better visibility the curves are given in double and half logarithmic scale.

material. Considering the undisturbed fluence dependence, the amorphization fluence is the lowest for the heaviest ion (Ar) and increases with decreasing ion mass, i.e. with decreasing number of displacements per ion and unit path length. This is explained by the dilution of the collision cascades for decreasing ion mass. Contrary, for the irradiation with Li-ions the amorphization fluence is very small and nearly the same as for the irradiation with O-ions. This small amorphization fluence is probably also caused by the fact that Li is a host atom.

References:

[1] C.S. Schnohr, E. Wendler, K. Gärtner, W. Wesch, J. Appl. Phys. 99 (2006) 123511.

Channeling irradiation of LiNbO₃

F. Schrempel, T. Steinbach, Th. Gischkat, W. Wesch

Recently it was shown that Ion Beam Enhanced Etching (IBEE) is a powerful patterning technology for the fabrication of novel photonic devices in LiNbO$_3$ [1,2]. Thereby it is utilized, that the defects formed due to ion irradiation reduce the chemical resistance of the crystal. Thus the irradiated regions can easily be removed by means of wet chemical etching in a HF-solution. However, the damage formation is influenced by the crystal orientation with respect to the direction of the incident ions.

Fig. 1: Relative defect concentration versus depth (a) and peak shift as well as ratio of the maximum defect concentration between on- and off-axis irradiation versus the ion fluence (b) of x-cut LiNbO$_3$ irradiated with 550 keV Si-ions.

Commercial x-cut ([11$\underline{2}$0]) and z-cut ([0001]) optical grade LiNbO$_3$ crystals were irradiated with 550 and 750 keV Si-ions, respectively. The irradiation was done at room temperature with ion fluences between 1×10^{13} and 6×10^{14} cm^{-2}. The experiments were performed in a chamber allowing stepwise ion implantation and sub-

sequent RBS analysis without removing the sample and guaranteeing a beam divergence less than 0.1°. The irradiation was performed at tilt angles between 0° and 1° with respect to the axis. The random irradiation was carried out 7° off axis. To investigate the damage accumulation, Rutherford Backscattering Spectrometry (RBS) in channeling configuration was applied using 1.8 MeV H-ions. From the Nb part of the RBS spectra the relative concentration of displaced lattice atoms n_{da} (defect concentration) was calculated. Subsequently, selected samples were etched in a HF-solution and the etched depth relative to the surface was measured with a Sloan DEK-TAK surface profilometer.

Figure 1a shows the defect concentration as a function of depth for x-cut LiNbO$_3$ irradiated with 550 keV Si-ions at different ion fluences. For the off-axis irradiation the maximum of the defect distribution is located at a depth of 365 nm. If the irradiation is carried out in axial direction the defect distribution is shifted to larger depths. Additionally, less damage is created by on-axis than by off-axis irradiation. Figure 1b gives the shift of the damage peak and the ratio of the defect concentration taken in the maximum of the distribution of the on- and the off-axis irradiation as a function of the ion fluence. The peak shift decreases and the damage ratio increases with increasing ion fluence, i.e. with increasing defect concentration.

Considering the off-axis irradiation, x- and z-cut LiNbO$_3$ show identical etching behavior. For both crystal cuts the final etched depth amounts to 765 nm excellently agreeing with the calculated distribution of displaced lattice atoms. In the case of the on-axis irradiated samples the finally etched depth is higher compared to that of the off-axis irradiation, but the shift strongly depends on the crystal orientation. The shift amounts to 310 and 175 nm for the irradia-
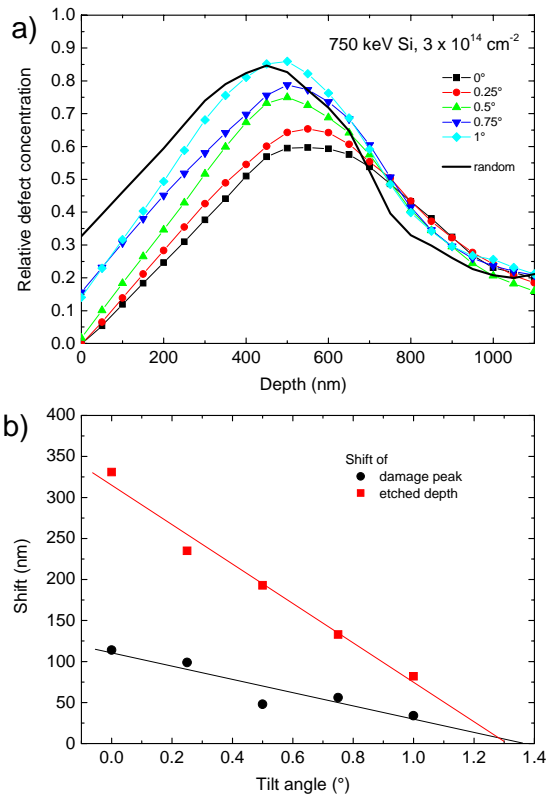
Fig. 2: Relative defect concentration versus depth (a) and shift of the damage peak and the maximum etched depth as a function of the angle of incidence of 750 keV Si-ions with respect to the crystal axis of x-cut LiNbO$_3$ (b).

tion along the x- and the z-axis, respectively. Compared to the off-axis irradiation the etched depth increases by a factor of 1.4 and 1.2 if the irradiation is carried out along the x- and the z-axis, respectively. With respect to the patterning of LiNbO$_3$ by means of Ion Beam Enhanced Etching the channeling irradiation offers the possibility to increase the depth of a structure compared to that of a random irradiation.

The reduced defect concentration and the shift of the damage peak as well as that of the etched depth to larger depths for the on-axis compared to the off-axis irradiation can be explained as follows. If the irradiation is performed along a low index crystallographic direction, the ions are prevented from close collisions with the target atoms (channeling). Consequently, an ideally channeled ion does not displace target atoms and experiences a reduced energy loss not only for elastic nuclear collisions but also for electronic interactions. Therefore the

irradiation induced defects occur at larger depths compared to an off-axis irradiation. Actually the channeled ions experience multiple scattering by various defects and by vibrating lattice atoms until they are de-channeled. Due to these processes defects are created at depths which are still larger compared to the defect distribution of an off-axis irradiation, but lower than that of the well channeled ions. The well channeled ions dominate the defect formation at very low fluences. Because the defect concentration increases with increasing ion fluence, the de-channeling probability increases and the de-channeled component is the dominating fraction. As a consequence the peak of the total distribution shifts toward lower depths with increasing ion fluence. At a sufficiently high defect concentration the channeling irradiation turns similar to a random irradiation explaining the saturation of the peak shift and the damage ratio at high ion fluences.

The influence of the tilt angle between the direction of the incident ions and the crystal axis on the defect formation is given in Fig. 2a. With increasing tilt angle the damage peak gradually shifts toward the surface and the maximum defect concentration increases. For an angle of incidence of 1° the maximum defect concentration reaches the value of the off-axis irradiation. Figure 2b shows the shift of the damage peak as well as of the depth obtained after etching in the 40% HF-solution as a function of the tilt angle. Both shifts decrease linearly with increasing tilt angle. The extrapolation of the regression line yields a tilt angle of about 1.35° for a zero shift which gives the critical angle to avoid channeling of the ions.

References:
[1] F. Schrempel, Th. Gischkat, H. Hartung, E.B. Kley, W. Wesch, Nucl. Instr. and Meth. B 250 (2006) 164.
[2] F. Schrempel, Th. Gischkat, H. Hartung, E.B. Kley, W. Wesch, A. Tünnermann, Mater. Res. Soc. Symp. Proc. 0908-OO16-01.1 (2005).

Etching of ion irradiated LiNbO$_3$ in aqueous HF solutions

J. Reinisch, F. Schrempel, Th. Gischkat, W. Wesch

In order to obtain a better understanding of the etching of ion damaged LiNbO$_3$, which is an important process step of ion beam enhanced etching (IBEE) for the fabrication of high-aspect ratio microstructures [1,2], congruent x-cut LiNbO$_3$ crystals were partially irradiated with Ar$^+$-ions at room temperature. Irradiation was performed with fluences ranging from 0.1 to 0.8 dpa. Subsequently the samples were etched stepwise in HF solutions with total concentrations c_0 ranging from 1 to 14% at temperatures of 24, 40 and 55°C, respectively. The etching rate was determined from the height difference between the masked and the unmasked region after each etching step.
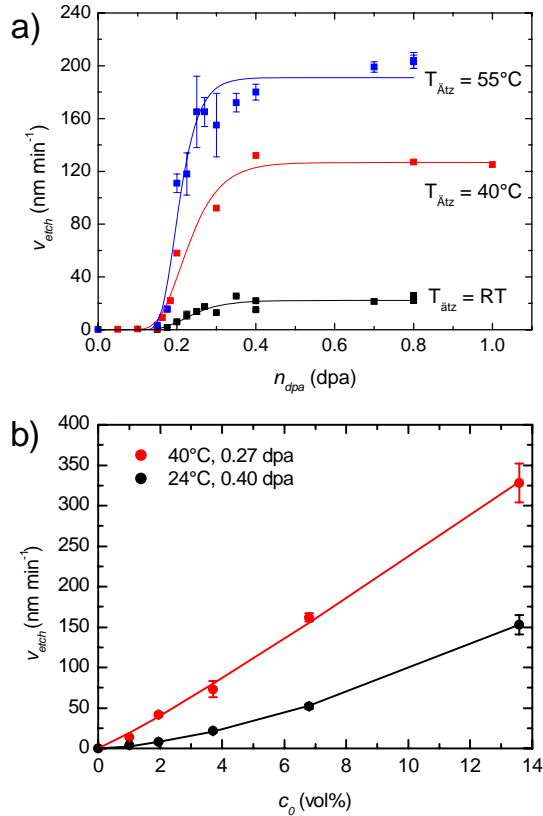
Fig. 1: Etching rate v_{etch} as a function of the normalized fluence n_{dpa} (a) and versus total HF concentration c_0 (b).

The etching rates are shown in Fig. 1a as a function of the fluence for etching in 3.7% HF at temperatures of 24, 40 and 55°C, respectively. The etching rate shows the same dependence for all three temperatures: The etching rate of the perfect LiNbO$_3$ crystal is below 0.1 nm min^{-1}, it increases rapidly at a normalized fluence of approximately 0.15 dpa and saturates at around 0.4 dpa. The maximum etching rate clearly increases with increasing temperature and the average increase amounts to 5.7 nm min^{-1} K^{-1} in the range of temperature investigated.

Apart from a high etching rate, the contrast of the applied technique is the key parameter for the fabrication of high aspect-ratio microstructures. The contrast is the better the steeper the etching rate increases with increasing fluence. Normalized to the corresponding maximum etching rate this increase is basically the same for all three temperatures and amounts to about 8 ± 3 dpa^{-1}. This is to say that in this range of temperature an acceleration of the etching process by the use of higher temperatures does not diminish the contrast.

In Fig. 1b the etching rate is shown as a function of the total HF concentration for LiNbO$_3$ irradiated at ion fluences of 0.27 and 0.40 dpa and etched at temperatures of 40 and 24°C, respectively. Apparently the etching rate increases with increasing total concentration and at a concentration of 13.6% etching rates of 150 nm min^{-1} and 320 nm min^{-1} are reached at temperatures of 24 and 40°C, respectively.

To find a kinetic expression that allows to describe the etching process, two questions have to be answered: Which molecules are present in the acidic solution and how do they participate in the etching reaction? The dissociation of HF in aqueous solutions up to a concentration of 14% at an acid temperature of 25°C can be explained considering only three dissociation equilibria

$$HF \longleftrightarrow H^+ + F^- \qquad (1)$$

$$HF + F^- \longleftrightarrow HF_2^- \qquad (2)$$

$$HF_2^- + HF \longleftrightarrow H_2F_3^- \qquad (3)$$
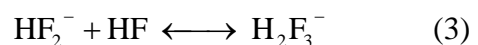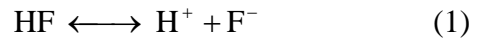
with the equilibrium constants $K_1 = 6.84 \times 10^{-4}$ mol l^{-1}, $K_2 = 5$ mol l^{-1} and $K_3 = 0.58$ mol l^{-1} [3]. Figure 2a displays the concentration of the corresponding ions calculated as a function of the total HF concentration.
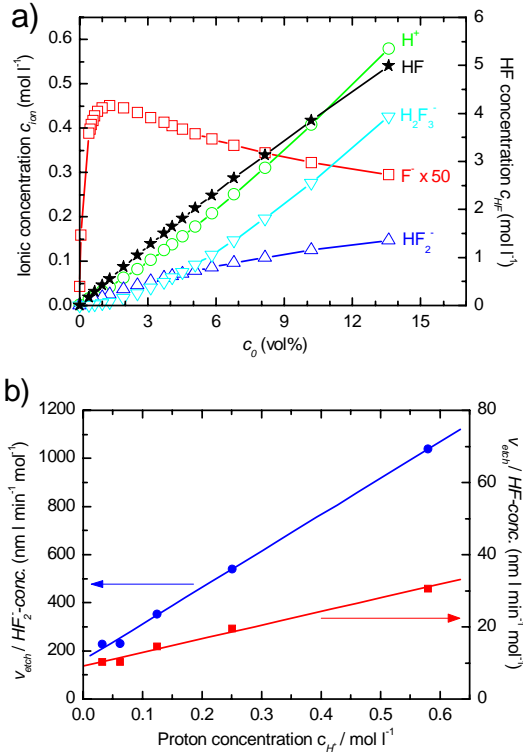
Fig. 2: Composition of aqueous HF solutions calculated from Eqs. 1-3 and depicted as a function of the total HF concentration c_0 (a) and description of the catalytic process by linear regression of the ratio of the etching rate v_{etch} and the concentration of the primary active molecule (HF or HF_2^-) c_1 as a function of the proton concentration according to Eq. 6.

Based on this model of dissociation, a kinetic model of the chemical reaction has to be found which yields a mathematical description of the relationship between the ionic composition and the measured etching rate. Referring to studies of HF etching of SiO$_2$ the etching mechanism is assumed to contain two steps: the dissolution of the oxygen atoms by adsorption of H$^+$-ions (activation) and of the metal atoms by fluoride species (substitution). Generally three types of reactions have to be distinguished

(i) reaction without protonation step

$$v_{etch} = k_1 \cdot c_1 \qquad (4)$$

(ii) protonation step as obligatory

$$v_{etch} = k_1 \cdot c_1 \cdot c_2 \qquad (5)$$

(iii) or catalytically accelerating

$$v_{etch} = k_1 \cdot c_1 + k_2 \cdot c_1 \cdot c_2 \qquad (6)$$

with c_1 and c_2 being the concentrations of the active fluoride and the H$^+$-ions, respectively.

That way only two reaction models are found to describe the experimental dependence of the etching rate on the HF concentration appropriately. In both cases it is described as a catalytic reaction (Eq. 6) with H$^+$ acting as a catalyst in the activation of the process ($c_2 = c_{H^+}$). The substitution step can be assigned to an attack of either HF ($c_1 = c_{HF}$) or HF$_2^-$ ($c_1 = c_{HF_2^-}$) molecules. Figure 2b shows the linear approximations using Eq. 6 for HF and HF$_2^-$ being the primary active molecule, respectively, which are both in good agreement with the results obtained.

Interpreting the rate laws obtained the surface interactions can be described as follows: At first the negatively charged free bonds of oxygen atoms at the surface are saturated with H$^+$-ions very rapidly by electrostatic attraction. Now the oxygen can desorb from the surface in the shape of an OH$^-$-molecule or as H$_2$O after a further complex formation by another H$^+$-ion. These two alternative reaction paths cause the additive ansatz of the catalytic reaction. In a second step the metallic (Li and Nb) atoms can be removed by an attack from either HF or HF$_2^-$, leaving behind free oxygen bonds at the new surface.

References:
[1] F. Schrempel, Th. Gischkat, H. Hartung, E.-B. Kley, W. Wesch, Nucl. Instr. and Meth. B 250 (2006) 164.
[2] F. Schrempel, Th. Gischkat, H. Hartung, E.-B. Kley, W. Wesch, A. Tünnermann, Mater. Res. Soc. Symp. Proc. 0908-OO16-01.1 (2005).
[3] K.W. Kolasinski, J. Electrochem. Soc. J99 152(9) (2005).

Comparison of ion-induced damage formation in <110> and <100> MgO

E. Wendler, G. Gärtner, W. Wesch

In this work the defect production in Ar and Xe irradiated MgO is studied at 15 K over a wide range of ion fluences from several 1×10^{12} to 1×10^{16} cm^{-2} and for two different orientations of the MgO crystal (<110> and <100>) [1]. Special attention is directed to the range of very low ion fluences at which the collision cascades of individual ions do almost not overlap. For this range nearly no data can be found in literature so far. Furthermore the effect of high ion fluences is studied in detail, where the defect concentration saturates.

For implantation and subsequent analysis with Rutherford backscattering spectrometry (RBS, 1.4 MeV He, $\Theta = 170°$) our two-beam chamber was used, which allows one to perform the two processes at 15 K without changing the environment of the sample.

The RBS channelling data were analysed using the computer code DICADA [2] assuming a random distribution of the displaced lattice atoms within the lattice cell.

Fig. 1 shows the number of displaced lattice atoms in the maximum of the distribution, n_{da}^{max}, averaged over the region of maximum nuclear energy for the two ion species (in the following referred to as defect concentration n_{da}^{max}). For low ion fluences n_{da}^{max} increases almost linearly with N_I in all cases investigated (referred to as region I). For larger ion fluences ($N_I > 2\times10^{14}$ Ar cm^{-2} and $> 5\times10^{13}$ Xe cm^{-2}, respectively) n_{da}^{max} increases super-linear with N_I (referred to as region II), reaching a maximum value. This maximum value of n_{da}^{max} is higher for the <100> oriented than for the <110> oriented samples. At even higher fluences ($N_I > 8\times10^{14}$ Ar cm^{-2} and $> 3\times10^{14}$ Xe cm^{-2}, respectively) n_{da}^{max} decreases with rising ion fluence at the corresponding depth region (referred to as region III). This effect is stronger in <110> than in <100> direction.

To analyse the range of low damage within region I for the various implantation conditions, the defect concentration at the depth of maximum nuclear energy deposition, n_{da}^{max}, is plotted in Fig. 2 versus the number of displacements per lattice atom n_{dpa}, which is proportional to the ion fluence. From Fig. 2 it is

Fig. 1: Relative defect concentration, n_{da}^{max}, at the depth of maximum nuclear energy deposition versus ion fluence N_I for Ar ions (upper part) and Xe ions (lower part) implanted in <110> and <100> MgO. The linear dependence in region 1 is visualized by the solid lines.

obvious that all data points fall on one line independent of ion species, implantation energy and crystal axes. This means that the defect production is determined by the energy deposited into nuclear collision processes. The slope of the line is 0.5. This means that only 50% of the primarily displaced lattice atoms survive the relaxation of the collision cascades. This result is in agreement with the surviving defect fraction of 0.15 and 0.40 given in ref. [3] (for details see [1]). The slope of the line in Fig. 2 yields the cross section of defect production per ion P which is given by $n_{da}^{max} = P N_I$. Assuming each ion to produce an amorphous cluster, P is the area damaged by one ion (projected to the surface). Replacing N_I by n_{dpa} provides $P = (n_{da}^{max} / n_{dpa}) (N_{displ}^* / N_0) \approx 0.5 N_{displ}^*/N_0$. From that the diameter of the amorphous clusters $d = (4P/\pi)^{1/2}$ can be

estimated to 0.19 nm and 0.35 nm for Ar and Xe ions, respectively. These values are smaller than the lattice constant of MgO of 0.413 nm. Therefore this estimation demonstrates that Ar
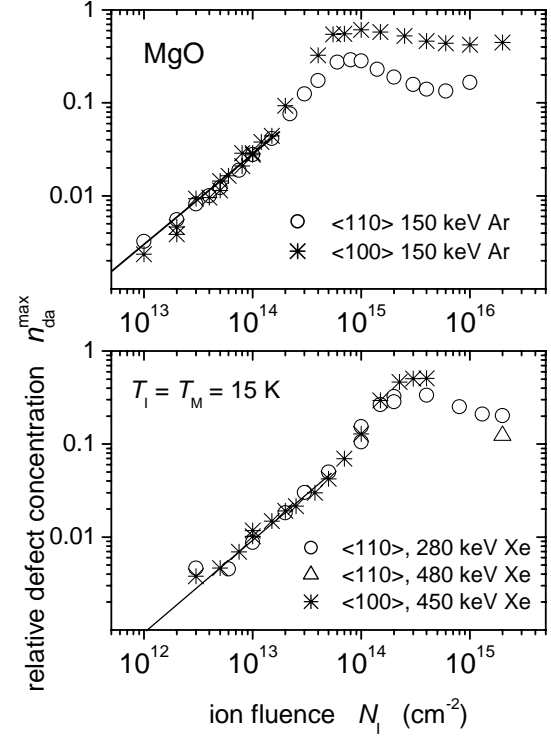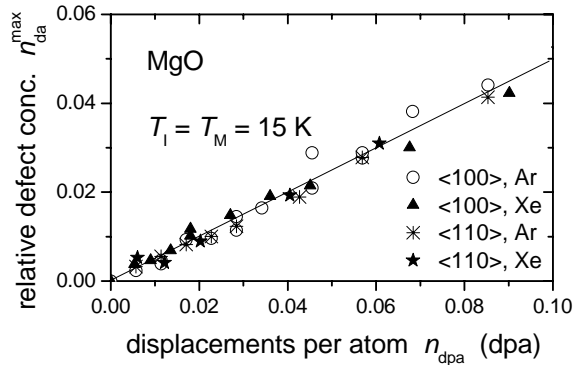

Fig. 2: Relative defect concentration, n_{da}^{max}, at the depth of maximum nuclear energy deposition versus number of displacements per lattice atom for various implantation conditions applied. The line is a linear fit to the data.

or Xe ions implanted in MgO at 15 K do not produce amorphous zones, but only point defects or complexes of point defects which are - because of the agreement for the two crystal axes within region I - randomly distributed within the lattice cell. For fluences within region II in which a super-linear increase of the defect concentration with rising ion fluence is observed and the collision cascades start to overlap, a complex defect structure is formed which exhibits a different defect concentration along the two different axes (at least in the case of Ar implantation; see Fig. 1). The super-linear increase of the defect concentration suggests that some kind of defects is growing rapidly. Most probably the defect structure formed consists of a mixture of defect clusters and extended defects (correlated displaced lattice atoms; see [1]). In region III in the case of Ar implantation the damage concentration saturates at $n_{da}^{max} \approx 0.35$ for <110> and ≈ 0.6 for <100> MgO. Furthermore, distributions (not shown, see [1]) show a strong reduction of the defect concentration near the surface and an extension of defects into larger depths, which is at least partially caused by the high ion concentration which can give rise to the generation of defects. To get more information about the structure of defects formed in region III, energy dependent RBS channelling studies were performed at 15 K and 295 K for a <100> oriented sample implanted with 1×10^{16} Ar cm^{-2}. Fig. 3 depicts the minimum yield χ_{min} versus the energy of the

analysing He ions E_M for two different depth regions: close to the surface and behind the damaged layer. In the near-surface region χ_{min} increases with E_M. This behaviour applies up to depths of about 0.1 µm (not shown). Behind the damaged layer χ_{min} remains constant. The result that χ_{min} increases with increasing energy indicates that also dislocations or dislocation loops must exist in the layer which compensate the negative energy dependence of χ_{min} due to point defects (see [1]). Summarising we can say that at very low ion fluences where the collision cascades do not overlap, point defects as well as point defect clusters are formed. Further implantation to higher fluences results in a defect transformation and produces a mixture of point defects and dislocations or dislocation loops
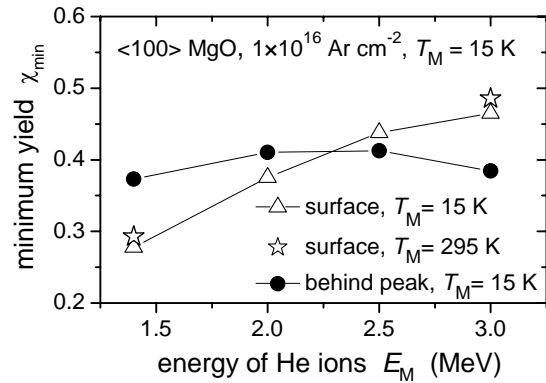
Fig. 3: Minimum yield χ_{min} of <100> MgO versus the energy of analysing He ions E_M for two different depth regions measured at two different temperatures.

[1] E. Wendler, K. Gärtner, W. Wesch, Nucl. Instr. and Methods B 2008, in press.
[2] K. Gärtner, Nucl. Instr. and Solids B 227 (2005) 522.
[3] S.J. Zinkle, C. Kinoshita, J. of Nucl. Mater. 251 (1997) 200.

Structural and stoichiometric properties of $Cu(In,Ga)Se_2$ thin films deposited by a non-vacuum process

J. Cieslak, Th. Hahn, B. Poppinga*, H. Metzner, and W. Witthuhn
Rudi Schaller Metalltechnik GmbH, Steinach 39, 96264 Mitwitz

The chalcopyrite semiconductor $Cu(In,Ga)Se_2$ is successfully used as absorber material in thin film solar cells both in laboratory scale and in commercial modules. The advantages of the thin film technique are lower costs as well as lower energy payback time in relation to manufacturing of single crystalline silicon solar cells. $Cu(In,Ga)Se_2$ absorbers are processed most commonly by either the co-evaporation of the elements [1] or the stacked elemental layer rapid thermal processing [2]. Both methods are vacuum processes. The Avoidance of vacuum processes could lead to further cost reduction of photovoltaic devices.

Within the framework of a cooperation project, the company Metallbau Schaller (Mitwitz) is establishing a non-vacuum process for thin $Cu(In,Ga)Se_2$ absorber layers. In the first step, on the substrate, a thin molybdenum foil, layers of Cu, In and Ga were electrochemical deposited. In a second step, the metallic precursors were annealed in a $Se/H_2/N_2$ atmosphere at temperatures of typical 600°C.

At the Institute for Solid State Physics in Jena, the samples were characterized concerning morphology, chemical and phase composition. For that purpose, scanning electron microscopy (SEM), energy dispersive x-ray detection (EDX) and x-ray diffraction (XRD) with following Rietvelt analysis were employed.

A. Morphology
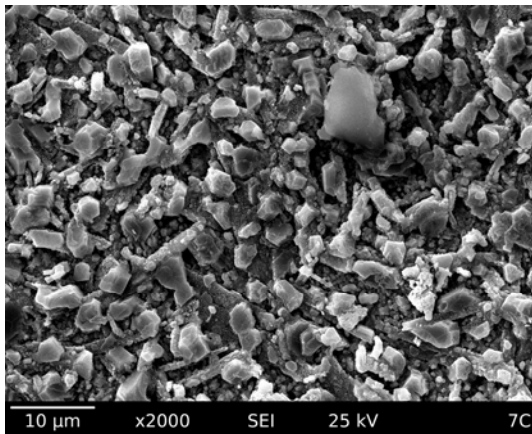
Fig. 1: SEM image of a $CuInSe_2$ absorber layer.

From the SEM image of a typical $CuInSe_2$ film, shown in fig. 1, we can obtain several morphological attributes. First, the crystallites are statistically oriented, which reveals the polycrystalline nature of the layer. Second, the sample comes up with a large variability of grain shapes and sizes. This already suggests a coexistence of different crystalline phases in the film. Third, the film seems to contain holes and forms no compact layer.

B. Composition

From EDX mappings (fig. 2), the lateral variation of the chemical composition of the $CuInSe_2$ sample was determined. Due to the penetration depth of the electron beam of about one micrometer, signals from the layer as well as the substrate were obtained. So, a higher EDX signal of molybdenum means a lower thickness of the layer above at the respective position. Figure 2 reveals that both thickness and chemical composition of the absorber layer are not constant. Three regions can be distinguished. The relative amounts of the substrate and layer materials in these regions are summarized in table I. Region I contains only very small amounts of the layer elements Cu, In and Se. Region II is very Cu rich and region III slightly Cu rich.
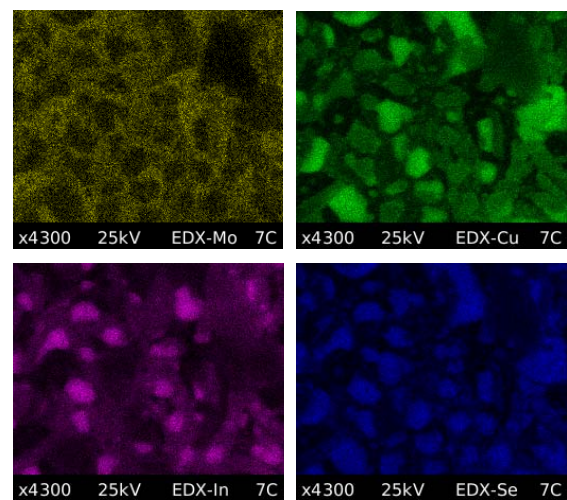
Fig. 2: EDX mappings of the elements Mo (substrate material), Cu, In and Se of a 31x24 µm sized region of a $CuInSe_2$ thin film.

region	Mo	Cu	In	Se
I	40,9%	2,3%	0,6%	1,8%
II	11,3%	22,7%	0,7%	16,2%
III	9,3%	6,7%	5,4%	12,5%

Tab. I: Amount of elements in three regions of $CuInSe_2$ sample from EDX measurement

Thus the substrate is not completely covered by the film, which consists of separated grains with different chemical composition.

C. Phase analysis

The results of the phase analysis by Rietvelt analysis of the x-ray diffraction pattern, shown in fig. 3 confirm and specify the findings from SEM and EDX measurements. The thin film mainly consists of CuSe and $CuIn_3Se_5$, whereas the binary CuSe is dominating. The chalcopyrite phase $CuInSe_2$ is not significant.
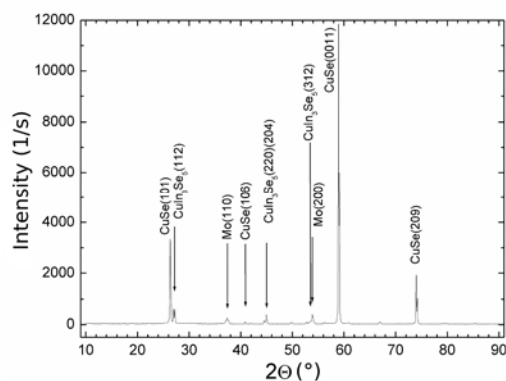
Fig. 3: X-ray diffraction pattern of a $CuInSe_2$ thin film, detected in Bragg-Brentano geometry.

D. Discussion

The experimental results lead to two questions. First, starting from a nearly stoichiometric CuIn precursor, why is the selenized film very In poor? Second, why isn't the chalcopyrite phase during the selenization process formed?

The formation of $Cu(In,Ga)Se_2$ from elements occurs in three main phases. Starting from the elements, in the early reaction steps binary selenides are formed [3,4], i.e. In_2Se, In_2Se_3, InSe, Cu_2Se, CuSe, $CuSe_2$, GaSe, Ga_2Se_3. Later in the reaction path, in the second phase, copper selenides and group III selenides compound to the ternary $CuInSe_2$ and $CuGaSe_2$. The quaternary $Cu(In,Ga)Se_2$ forms from the ternary compounds in the last phase. Because of the high amount of CuSe in the samples investigated, the reaction from the elements to $CuInSe_2$ was aborted at the beginning of the second phase. So, a higher selenization time should be favorable to form the ternary $CuInSe_2$.

The In loss during the selenization is a well known phenomenon [5]. It is caused by a re-evaporation of the volatile In_2Se that can form during an early stage of the process. To avoid the In loss, it is necessary to pass the critical temperature range from 300°C to 350°C very fast.

In conclusion, we examined structural and compositional properties of $Cu(In,Ga)Se_2$ thin films deposited by a non-vacuum process. The films are polyphase and form no compact layer. The main phase is CuSe. The results of our investigations may help to improve the deposition process for the next phase of the project.

References
[1] M.A. Contreras, J. Tuttle, A. Gabor, A. Tennant, K. Ramanathan, S. Asher, A. Franz, J. Keane, L. Wang, R. Noufi, Sol. Energ. Mat. Sol. C. 41-2 (1996) 231
[2] A. Brummer, V. Honkimäki, P. Berwian, V. Probst, J. Palm, R. Hock, Thin Solid Films 437 (2003) 297
[3] H. Matsushita, H. Jitsukawa, T. Takizawa, J. Cryst. Growth 166 (1996) 712
[4] F. Hergert, S. Jost, R. Hock, M. Purwins, J. Sol. State Chem 179 (2006) 2394
[5] J. Schmidt, H.H. Roscher, R. Labusch, Thin Solid Films 251 (1994) 116

Optical properties of strained polycrystalline CuInS$_2$ layers

J. Eberhardt, H. Metzner, R. Goldhahn[*], F. Hudert[*], K. Schulz, U. Reislöhner, Th. Hahn,
J. Cieslak, and W. Witthuhn

[*]*Institut für Physik, Technische Universität Ilmenau, PF 100565, 98684 Ilmenau*

In a thin-film solar cell which is a multi-layer structure, strain is a very common phenomenon and will thus also effect the light absorber layer as the most crucial part of the solar cell. Investigations of strain induced phenomena in CuInS$_2$ (CIS) solar-cell material have not been reported to date. In this work, different amounts of strain are imposed to CIS layers by a thick silicon substrate with or without a molybdenum buffer layer of various thickness. Additionally, the internal strain of these layers depends on the CIS film thickness.

Polycrystalline CIS films were grown by means of molecular beams on top of Si(001) wafers with 4 inch diameter covered with a Mo buffer layer of 200 or 500 nm thickness. The Mo layers were deposited on the untreated Si substrates by radio frequency magnetron sputtering. Some CIS films were grown directly on untreated Si wafers without Mo. Details of all investigated samples are given in table I.

Table 1: Investigated samples: s.c. = single crystal, p.c. = polycrystalline.

Sample	CIS Structure	Layer sequence	Layer thicknesses: Si/Mo/CIS (μm)
#1	s. c.[a]	-	-
#2	p. c.	Si/Mo/CIS	500/0.2/2.5
#3	p. c.	Si/Mo/CIS	500/0.2/2.2
#4	p. c.	Si/Mo/CIS	500/0.2/1.5
#5	p. c.	Si/CIS	500/0/0.2
#6	p. c.	Si/Mo/CIS	500/0.2/0.2
#7	p. c.	Si/Mo/CIS	500/0.5/0.2

[a] Data taken from Ref. 1.

The substrate temperature during film growth was kept at 825 K. All polycrystalline samples were grown slightly copper rich. The Cu to In atomic ratio changed from 1.8 for the as-grown state to nearly stoichiometric after a wet-chemical KCN etching step, which was applied to all investigated samples. Photoluminescence (PL) was excited by the 514-nm line of a continuous wave Ar$^+$ laser with a typical power of 150 mW on the sample. Light of a 150 W Xe arc lamp dispersed by a monochromator served as the probe beam for the photoreflectance (PR) studies. The internal electric fields of the samples were modulated by the 514-nm line of the Ar$^+$ laser chopped at 360 Hz. A Si-photodiode in combination with a lock-in amplifier were used for signal detection.

All samples of the present investigation were characterized by PL measurements at various temperatures and in all cases excitonic emissions were observed which were discussed elsewhere [2]. In order to supplement the PL data, also PR measurements were performed on the polycrystalline samples. However, the reflectance signal was only detectable for samples #5 and #7 which had the smoothest surfaces. Figure 1 shows the respective PR spectra measured at 80 K on these two polycrystalline CIS samples with a thickness of 200 nm. Sample #5 of figure 1(a) was grown directly on Si without Mo buffer layer, whereas sample #7 of figure 1(b) was grown on Si covered with 500 nm Mo. The PR spectra are compared to PL measurements recorded at 5 and 80 K. The solid lines represent least squares fits to the data (dots) yielding the positions of FX^A, FX^B, and FX^C as indicated. In the case of the PR spectrum of sample #5 in figure 1(a), this fit leads for FX^A to an unreasonably broad line width combined with a oscillator strength which is 25 times higher than that for FX^B and FX^C.

However, it was shown by means of X-ray diffraction (XRD) measurements that the CIS crystallites in the investigated polycrystalline samples grow in random orientations without a noticeable texture [3] (data not shown). In this case, the oscillator strengths are equal for all three excitonic transitions and independent of strain. This condition is satisfied by the least-squares fit of the PR spectrum of sample #7 in figure 1(b) where the line widths as well as the oscillator strengths, respectively, are identical for FX^A, FX^B, and FX^C. The dashed line in figure 1(a) shows a fit with identical oscillator strengths and line widths for the three excitonic transitions. The obvious deviation of this fit curve from the measured data is discussed below. First we focus on the measured excitonic energies.
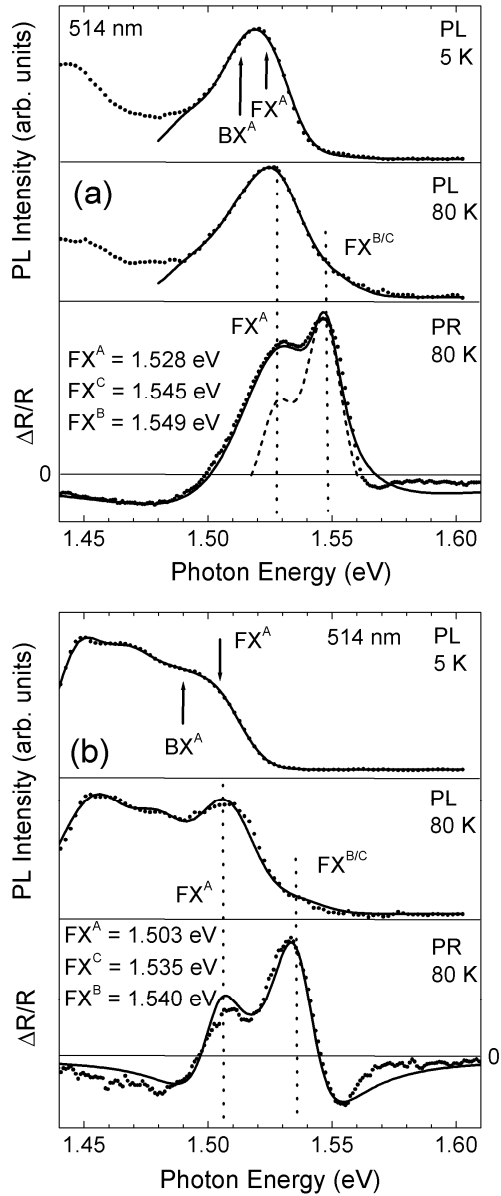
Figure. 1: Comparison of PR and PL spectra measured on sample #5 [figure 1(a)] and sample #7 [figure 1(b)], respectively. For sample #5, 200 nm polycrystalline CIS was grown directly on Si, whereas in sample #7, the 200 nm CIS was grown on Si covered with 500 nm Mo. The solid lines represent least squares fits to the data, yielding the positions of FX^A, FX^B, and FX^C. The solid line in figure 1(b) and the dashed line in figure 1(a) show fits with identical oscillator strengths and line widths for FX^A, FX^B, and FX^C. PL measurements were performed with an excitation power of 150 mW.

Comparing the results of the PR measurements, the transition energy of FX^A is shifting from 1.528 eV for sample #5 [figure 1(a)] without Mo buffer to 1.503 eV for sample #7 [figure 1(b)] with Mo buffer layer at a constant thickness of the CIS film. Assuming a decreasing transition energy with increasing tensile strain [4, 5], this behavior can be explained by an additional tensile strain which is introduced by the Mo buffer layer. Considering the indicated transition energies, it can be seen that the decrease of the absolute energy of FX^A is accompanied by an increase of the splittings between FX^A, FX^B, and FX^C. So, the splitting FX^C-FX^A increases from 17 to 32 meV and FX^B-FX^C from 4 to 5 meV for the samples #5 and #7, respectively.

The deviation between the measured data and the dashed line in figure 1(a) leads to the assumption of an inhomogeneous strain distribution in sample #5. The increased line broadening of FX^A accompanied by the apparent increased oscillator strength is likely due to contributions from regions in the sample with stronger tensile strain. The occurrence of different amounts of strain in this sample is thus explained by spatial inhomogeneities. The reason, why the CIS layer without Mo buffer appears to be inhomogeneous with respect to strain, while the CIS layer with Mo buffer shows an uniform strain field, remain obscure at present. Due to the consistent results of PR and PL measurements, the transition energies at 80 K are directly comparable. In a previous publication [6], it was shown that the apparent blue shift of the excitonic emission at 1.53 eV between 5 and 80 K can be explained by the transition from the bound (BX^A) to the free A-exciton (FX^A) with increasing temperature. At temperatures below 80 K, FX^A only appears as a weak shoulder on the high energy tail of BX^A.

In conclusion, for the first time a detailed and consistent investigation of strain in CIS thin-films by means of PL and PR could be presented. The results show a pronounced impact of the layer thicknesses in a solar cell on the strain in the absorber layer.

[1] S. Shirakata and H. Miyake, J. Phys. Chem. Solids **64**, 2021 (2003).

[2] J. Eberhardt, H. Metzner, R. Goldhahn, F. Hudert, K. Schulz, U. Reislöhner, Th. Hahn, J. Cieslak, and W. Witthuhn, Mater. Res. Soc. Symp. Proc. Vol. **1012**, 419 (2007).

[3] J. Eberhardt, H. Metzner, K. Schulz, U. Reislöhner, Th. Hahn, J. Cieslak, R. Goldhahn, F. Hudert, J. Kräußlich ,and W. Witthuhn, J. Appl. Phys. **102**, 033503 (2007).

[4] B. Gil, O. Briot, and R.-L. Aulombard, Phys. Rev. B **52**, R17028 (1995).

[5] B. Gil, F. Hamdany, and H. Morkoç, Phys. Rev. B **54**, 7678 (1996).

[6] J. Eberhardt, K. Schulz, H. Metzner, J. Cieslak, Th. Hahn, U. Reislöhner, M. Gossla, F. Hudert, R. Goldhahn, and W. Witthuhn, Thin Solid Films **515**, 6147 (2007).

CdTe solar cells with thin absorbers

M. Hädrich, C. Löffler, C. Kraft, S. Mack, H. Metzner, U. Reislöhner, W. Witthuhn

CdTe is an attractive solar cell material which has entered mass production only some years ago. The potential for improvement of the solar cell stacks and of the process techniques is still high. On the one hand, the typical efficiency of CdTe modules is below 10% while laboratory cells reach conversion efficiencies of more than 16% [1]. On the other hand, the employed CdTe layers have to be much thicker than physically necessary for light absorption in order to avoid pinholes in the films. Thickness reduction of the absorber layer is not only useful to minimize the material costs in the production process but can also yield better solar cell properties [2]. In particular, thinner films allow more carriers to pass the material within their lifetime without recombination [3]. To this end, the films must be compact and free of pinholes. A critical point for that is the formation of a low-ohmic back contact. Usually a wet-chemical etch with nitric and phosphoric acid (NP-etch) is applied to obtain a tellurium rich intermediate layer at the CdTe surface. However the etching especially affects the grain boundaries and leads to voids when thin absorber films are employed. Therefore alternative ways for back contact formation are required.

We used an approach which abandons any etching. Instead a thin bilayer of copper and gold was applied to obtain the primary contact at the CdTe surface. First, our results show a slight improvement of the solar cell properties when thick absorber layers were employed. Second, when using this back contact, thin absorber layers yielded better solar cells than thick absorber layers.

All solar cells in these experiments were produced in our own laboratory. Our baseline for CdTe solar cell production is described elsewhere [4]. We deposited the CdS and the CdTe layers sequentially on commercially available TCO coated soda-lime glass using the close-space-sublimation (CSS) technique. The temperature during deposition was 500°C for CdS and 470°C for CdTe. Samples with different CdTe film thicknesses were prepared and the layer thicknesses were measured with a step profilometer. The stacks were subjected to thermal post-deposition treatment with $CdCl_2$ in air (activation) and a subsequent cleaning step.

Copper and gold were sequentially deposited by physical vapour deposition without breaking the vacuum. The primary back contact was finished by annealing in air. Reference samples were prepared identically applying a wet etching instead of the copper-gold bilayer. All samples were covered with a 0.5µm molybdenum layer deposited by ion sputtering to extract the photocurrent. Solar cell characteristics were measured under standard AM1.5 illumination conditions.

In Fig. 1, the cross-section SEM micrograph of a typical solar cell structure from our laboratory without back contact is shown.
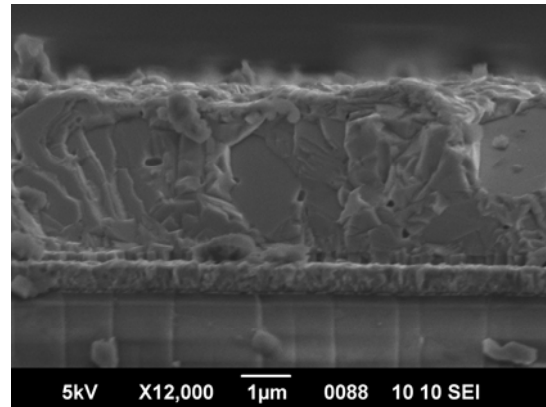

Fig.1: Cross-section SEM micrograph of a solar cell structure without back contact. From bottom to top, the glass substrate, TCO, CdS and CdTe films are visible.

On top of the glass substrate, the 500nm TCO layer and the 200nm CdS layer are visible. The CdTe film is about 3.7µm thick and appears dense and compact.
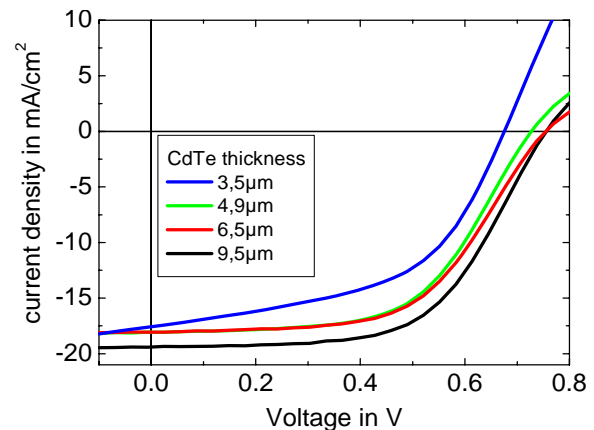
Fig.2: J-V-characteristics of solar cells with different absorber thicknesses. All absorbers were etched for back contact formation.

In Fig.2, the current-voltage characteristics of solar cells with different absorber thicknesses are shown. All absorbers were wet-chemically etched for back contact formation. In Table 1, the properties of the solar cells are listed.

CdTe thickness [µm]	3.5	4.9	6.5	9.5
V_{oc} [mV]	677	728	755	756
J_{sc} [mA/cm^2]	17.6	18.1	18.1	19.5
R_s [Ωcm^2]	10	12	13	12
R_p in [kΩcm^2]	0.16	1.19	1.33	1.76
FF	0.52	0.57	0.57	0.59
η [%]	6.2	7.6	7.7	8.6

Table 1: Properties of solar cells with different absorber thicknesses. All absorbers were etched for back contact formation.

The results show that the cells with the thickest absorber layers yield the best properties. All cell parameters degrade when thinner absorbers are employed and the wet etching step is applied. The etching leads to voids and shunts which become pronounced in the parallel resistance diminishing by an order of magnitude from the cell with the thickest absorber to the cell with the thinnest absorber. Reduced open-circuit voltage, fill factor and efficiency are the consequence.

In Fig. 3, the current-voltage characteristics of other solar cells with different absorber thicknesses are shown.
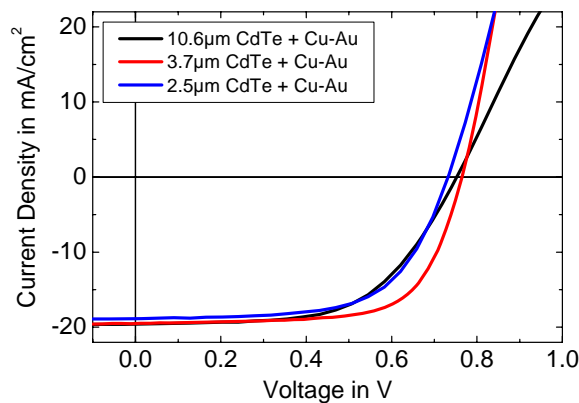
Fig.2: J-V-characteristics of solar cells with different absorber thicknesses. A thin copper-gold bilayer was used as back contact.

However the absorbers of these cells were not etched but a copper-gold bilayer was used as primary back contact.

In Table 2, the properties of these cells are listed.

CdTe thickness [µm]	2.5	3.7	10.6
V_{oc} [mV]	735	762	753
J_{sc} [mA/cm^2]	18.9	20.4	19.1
R_s [Ωcm^2]	5.5	6.1	9.2
R_p in [kΩcm^2]	1.15	1.60	1.46
FF	0.63	0.66	0.58
η [%]	8.7	10.2	8.6

Table 2: Properties of solar cells with different absorber thicknesses. A thin copper-gold bilayer was used as back contact.

Cells with a thick absorber layer (10.6µm) and Cu-Au back contact yield slightly better properties than cells with thick (9.5µm, see table 1) etched absorber layers. The improvement thereby is a reduction of the series resistance and the vanishing of the roll-over in the I-V-characteristics for otherwise similar solar cell properties. Solar cells with a 3.7µm thin absorber layer have considerably better properties especially with respect to series resistance, fill factor and efficiency. For further reduction of the absorber thickness the open-circuit voltage and the efficiency decrease.

In order to proceed to yet thinner absorbers, the film morphology and the post-deposition treatment must be further adapted and optimized.

Our results show that employing back contacts without wet etching is a pathway to admit thickness reduction of the CdTe absorber layers. Thinner absorbers are beneficial to save material in the manufacturing process and can yield better solar cell properties.

References:

[1] C.S Ferekides, D. Marinskiy, V. Viswanathan, B. Tetali, V. Palekis, P. Selvaraj, D.L. Morel, Thin Solid Films 361-362 (2000), 520.
[2] N. Amin, T. Isaka, T. Okamoto, A. Yamada, M. Konagai, Jpn. J. Appl. Phys. 38 (1999) 4666.
[3] K. Taretto, U. Rau, Prog. Photovolt: Res. Appl. 12 (2004), 573.
[4] M. Hädrich, N. Lorenz, H. Metzner, U. Reislöhner, S. Mack, M. Gossla, W. Witthuhn, Thin Solid Films 515 (2007)

The New Scanning Electron Microscope at the IFK

Th. Hahn, M. Hädrich, C. Voigt, and W. Witthuhn

Scanning electron microscopy (SEM) and energy dispersive X-Ray spectroscopy (EDS) are well established and powerful tools in solid state physics and materials research which allow for a fast and non-destructive investigation of the morphology, structure, and chemistry of solid state samples with a high spatial resolution [1].

Since May 2007 a JEOL JSM-6490 SEM is running at the IFK. It is equipped with a thermal LaB_6 emitter as an electron source, which offers higher resolutions, higher beam current densities and higher uptimes as compared to conventional thermal Tungsten emitters. The large specimen chamber and stage of the microscope gives access to the whole area of large $100\times100mm^2$ samples, the target substrate size of all three photovoltaic process lines at the IFK. An additional advantage of the large microscope chamber is the existence of numerous extension ports, allowing the simultaneous integration of a broad range of additional analytical techniques, such as EDS, wavelength dispersive X-Ray spectroscopy (WDS), cathodoluminescence (CL), electron backscattering diffraction (EBSD), and electron beam induced current (EBIC). So far, an EDS system Genesis 4000 is integrated which was supplied by EDAX/Ametek. Its ultra-thin polymer foil window allows for the detection of light elements down to boron and its Li-drifted Si-detector has a tested energetic resolution of 128.8eV.

The resolution of the microscope is specified with 2.5nm at an electron energy of 30keV and 7nm at 3keV. It was verified during installation of the microscope with a sample consisting of gold nanoclusters on a graphite substrate (Fig. 2).

The elemental composition and distribution of a sample can be investigated in the SEM by various methods. The most obvious way is by employing the attached EDS-system. As an example, Fig. 3 depicts the EDS line-scan of a cross-section of a $CuInSe_2$ thin film solar cell together with the respective SEM picture. Details on the samples composition and preparation are described in the paper by M. Oertel et al. [2]. Here, one significant element from each layer of the solar cell was chosen to keep track of the layer sequence: Si from the glass substrate, Mo

Fig. 1: The new SEM at the IFK.
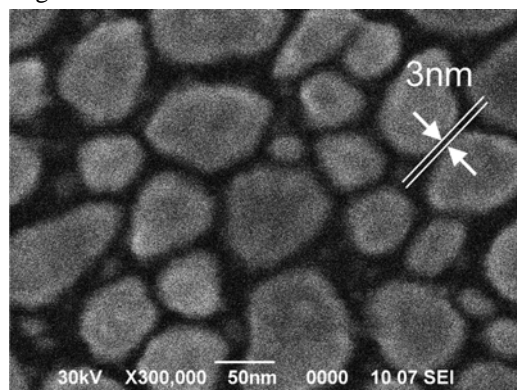
Fig. 2: SEM picture of Au-nanoclusters on a graphite substrate taken at 30keV incident electron energy in high resolution mode. Structures down to a few nanometers (here: 3nm distance between two Au clusters) can easily be detected.
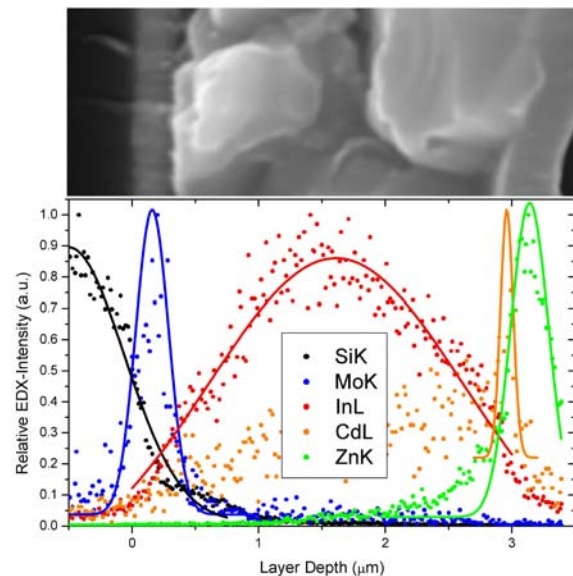
Fig. 3: SEM cross-section picture (above) and EDS line-scan (below) of an $CuInSe_2$ thin film solar cell. For the elements, the $K\alpha$- or $L\alpha$-lines were chosen for detection, respectively. The solid lines in the line scan are guides to the eyes only.
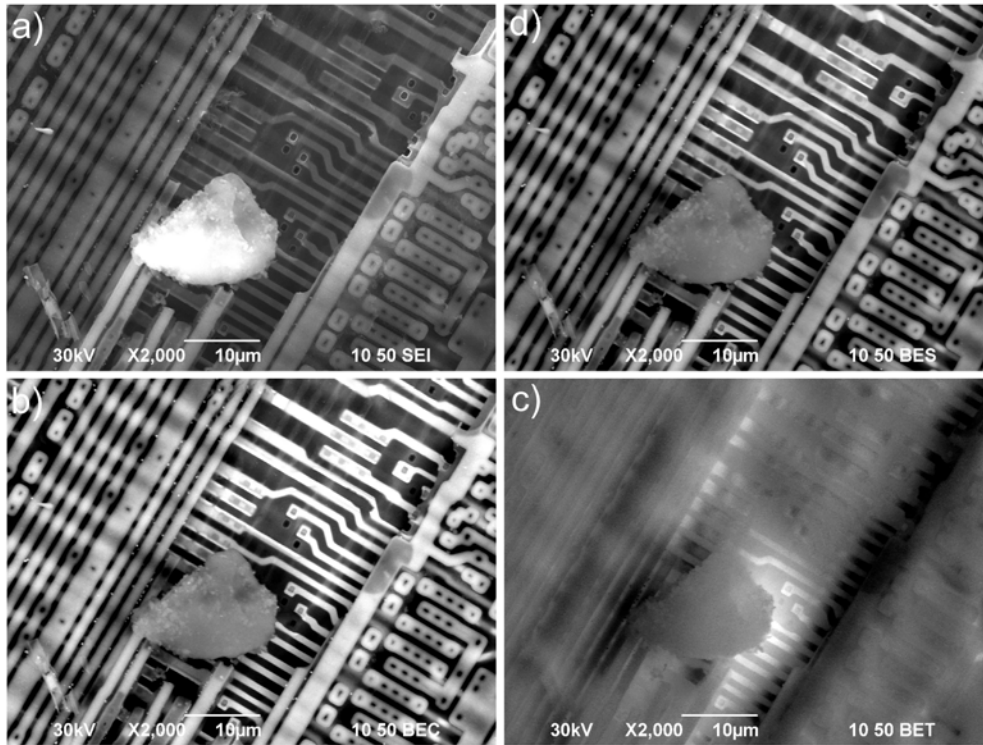
Fig. 4: SEM pictures of a DRAM (Fa. Siemens). The pictures were taken with different detector setups. Counter clockwise the detectors used were: (a) secondary electron detector (SEI), (b) backscattered electron detector in compositional mode (BEC), (c) backscattered electron detector in topographical mode (BET), and (d) backscattered electron detector in shadow mode (BES). While the SEI image gives the highest resolution and the highest surface sensitivity, the BEC image gives an high elemental contrast (light elements in the dust particle and the SiO_2 insulating base-layer, heavier elements in the conductor paths). The BET image is very sensitive to topographical variations, as can be seen by the shadowing effect of the dust particle. The BES image combines features of both, BEC and BET.

from the back contact, In from the $CuInSe_2$-absorber, Cd from the CdS buffer layer, and Zn from the TCO window layer.

Another way of investigating the composition of a sample in contrast to its morphology is to employ the detection of the two different types of electrons emitted from a sample during investigation (Fig. 4). While the secondary electrons detected in the secondary electron detector (SEI) are low in energy (E < 50eV) and therefore are only emitted from the first monolayers of a sample and additionally are easily shadowed by topographical variations, the amount of backscattered electrons (E >> 50eV) is highly sensitive on the atomic number of the elements in a sample and therefore give a pronounced picture of the elemental distribution within a sample. The backscattered electrons detector (BED) consists of three independent segments. While two of them work like in a conventional BED, either by adding or subtracting the two detector signals to get compositional or topographical sensitive images, respectively, the third segment is used for a JEOL-unique shadow-mode, which gives images resembling both, compositional as well as topographical features of a sample.

In conclusion, a new SEM has been installed at the IFK. It allows for the investigation of large area samples either by observation of secondary or backscattered electrons as well as a compositional quantification by means of EDS.

References

[1] L. Reimer, Scanning Electron Microscopy – Physics of Image Formation and Microanalysis, Springer (Heidelberg), ISBN 3540639764 (1998).

[2] M. Oertel et al., this report.

Manganese related deep level centers detected by DLTS

J. Bollmann[(1)], C. Hülsen, M. Thieme[(2)], W. Witthuhn

[(1)] ESM, Technische Universität Bergakademie Freiberg, 50937 Freiberg, Germany
[(2)] FZ Rossendorf, D-01314 Rossendorf, Germany

Introduction

By means of capacitance spectroscopy the formation of Manganese related point defects in silicon and germanium by radioactive transmutation of ^{56}Mn isotopes are studied. In comparison to shallow dopant impurities 3d transition-metals in silicon are characterized by deep levels, high diffusivities and show low solubility. An interstitial diffusion mechanism of neutral atoms could have been found for chromium, manganese and iron [1, 2].

Interstitial positions of Manganese in silicon introduces deep level centers with energy levels at E_V+0.30 eV ($Mn_i^{+/++}$), E_C−0.45 eV ($Mn_i^{0/+}$) and E_C−0.13eV ($Mn_i^{-/0}$) [3]. Manganese in Germanium introduces two levels at E_V+0.16(1) eV and E_C−0.37(2) eV [4].

Transmuting atoms undergo recoils resulting from emitted particles and radiation. It is of most relevance for experimental conclusions whether recoils may effect or change the lattice position or the defect configuration or not.

The basic idea in defect spectroscopy on materials doped with unstable atoms is to interpret the time dependencies of detected signals in terms of known half-life [5, 6]. This way one gets straight forward a knowledge what kind and how many atoms give rise to the defect spectroscopic signal. In capacitance spectroscopy (DLTS) the amplitude of the signals reflects straight forward the concentration of deep level centers while the peak temperature is related to the thermal activation energy of the center.

Experimental

Phosphorus-doped n-type, float zone refined and dislocation-free silicon crystals with a nominal free carrier density of (3-5) $\times 10^{15}$ cm^{-3} were implanted with radioactive ^{56}Mn isotopes using the facilities of the on-line isotope separator ISOLDE at CERN. Depending on to the isotope yield, implantation times from minutes up to one hour give fluxes in the order of 10^{12} cm^{-2}; which are suitable limits for radiation safety considerations.

The annealing were carried out under He atmosphere in sealed quartz ampoules at 850 °C (20min) both for silicon and germanium. After standard chemical cleaning procedures, finished by a short dip into HF (10 %) Au-Schottky contacts were evaporated under HV-conditions.

Results

^{56}Mn in n-type Silicon

The spectra taken at the beginning of the transmutation show two acceptor-like deep level centers. The further time evaluation of there concentration yields well defined that one manganese atom is involved in the defect.

As mentioned the occurring recoil energies should favorite the formation of vacancy related defects - but we do not find any evidence for the formation of vacancy related defects (A-center, divacancy) as well as daughter related defects (iron).

From the decay of ^{56}Mn (half-life 2.578h) into ^{56}Fe (stable) in n-type silicon two Mn-related acceptor-like traps at E_C−0.463(2) eV and E_C−0.142(2) eV could be determined; while both the vacancy-related A-

center and the divacancy complex could not be detected with ongoing transmutation.
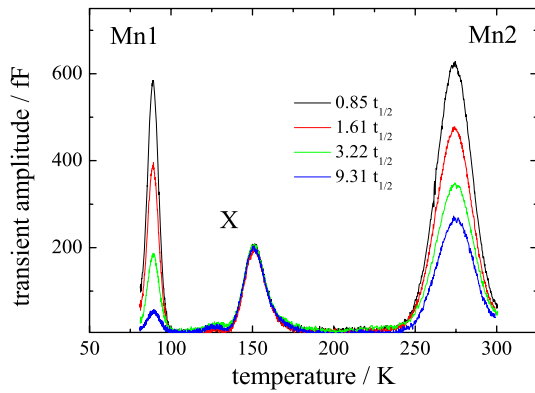
Fig. 1: Time evaluation of DLTS-spectra on n-type silicon implanted with [56]Mn.

That means that the local generated Frenkel-pairs completely recombine. Iron is known to introduce donor like deep level centers in particular to form iron-boron pairs having states in the lower part of silicon band gap [7].

In Fig. 2 the time evaluation of both levels are presented. For both levels a stable background is observed which is due to stable Mn. The mass separation on the GPS target station does not completely suppress close-by masses.
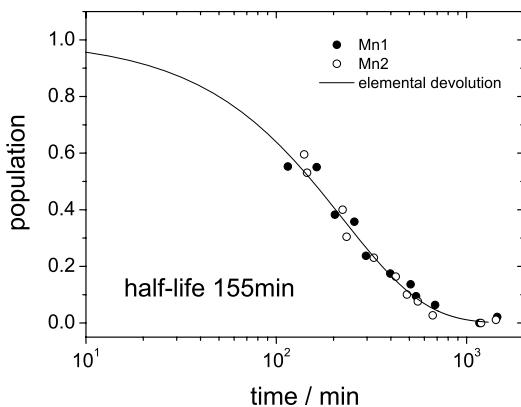
Fig. 2: Time evolution of defect concentration of [56]Mn related defects in n-type silicon detected by DLTS

The Arrhenius plots are given in Fig. 3. The defect energies refer to the conduction band edge and the frequencies are the pre-exponential factor according to

$$e_n = S_n \times exp - \{(E_C - E_T) / kT\}.$$
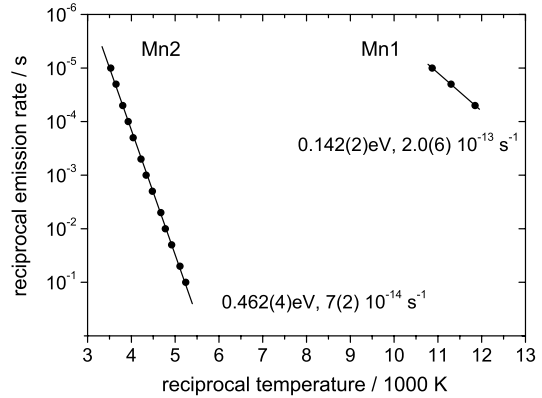
Fig. 3: Arrhenius plot of the thermal emission rates fort he two detected manganese related deep level centers in silicon.

[56]Mn in n-type Germanium

For n-type germanium we do not find any defect level in correspondence to the decay of [56]Mn. The spectra taken at the beginning of the transmutation process showed no significant defect signals. Thus we have no hint for the formation of a manganese related deep level center in the upper half of the energy gap in n-type germanium under our experimental conditions. Although the recoil energies would again suggest the generation of a few vacancies no level where observed.

References
[1] E. R. Weber: Appl. Phys. **A30**, 1-20 (1983).
[2] D. Gilles, W. Bergholz, W. Schröter: J. Appl. Phys. **59**, 3590 (1986).
[3] R. Czaputa, H. Feichtinger J. Oswald: Solid State Commun. **47**, 223 (1983).
[4] H. H. Woodbury, W. W. Tyler: Phys. Rev. **100**, 659 (1954).
[5] J. W. Peterson, J. Nielson: Nucl. Instr. and Meth. B **63**, 186 (1992).
[6] J. Bollmann: Physica B **273-274**, 433 (1999).
[7] A. A. Istratov, H. Hieslmair, E. R. Weber: Appl. Phys. A **69**, 13 (1999).

Investigation of CdTe Thin Film Solar Cells using different Transparent Conducting Oxides

C. Kraft, M. Hädrich, C. Löffler, U. Reislöhner, H. Metzner, W. Witthuhn

CdTe with a direct band gap of 1.45eV is an excellent absorber material for thin film solar cells. It grows p-type and highly stoichiometric forming a heterojunction with n-type CdS. Various deposition techniques using inexpensive substrates allow a low-cost large-scale production [1]. The highest conversion efficiencies of about 16% for laboratory cells have been obtained using close space sublimation (CSS) [2] and about 19% appear to be possible middle-term [3]. As the efficiencies of industrial modules are still less than 10%, improving CdTe thin film technology is essential.

We investigated the influence of different substrates with different transparent conducting oxides (TCO) on the properties of CdTe solar cells and optimized our solar cell production procedure for certain substrates. The choice of the substrate-glass and TCO influences several parameters such as transmission, light scattering, conductivity and is furthermore essential for the growth of the buffer and absorber layer [4]. To investigate the crystal growth we used Scanning Electron Microscopy (SEM) and Atomic Force Microscopy (AFM). To quantify the solar cell properties, we used external quantum efficiency (EQE) and current-voltage (I-V) characteristics measurements.

The cells were produced in our own baseline using $10 \times 10 cm^2$ glass substrates. For CdS- and CdTe-layer deposition we used the CSS technique. We employed a wet chemical treatment with a $CdCl_2$ solution for activation before annealing at about 380°C for 20 minutes. Afterwards we applied a standard nitric-phosphoric (NP) acid etching procedure. As back contact material molybdenum was applied. The glasses that were used had different thicknesses and chemical compositions, i.e. borosilicate- and soda-lime-glass was used. As TCO, indium doped (ITO) and fluorine doped (FTO) tin oxide with different sheet resistances were used. For industrial production borosilicate-glass and ITO appear to be less suitable due to high costs. The FTO-coated glass-substrates additionally had light scattering attributes which is described by its haze-value and showed higher transmission in a wavelength range of 600-900nm [5]. A summary of the glass attributes is given in Fig. 1.

glass	thickness	TCO	haze	sheetres.
borosilicate	2mm	ITO	0	8,5Ω/sq
soda-lime	4mm	ITO	0	9,3Ω/sq
soda-lime	3mm	FTO	3-5%	7,0Ω/sq
soda-lime	2,3mm	FTO	8-10%	7,6Ω/sq
soda-lime	3,2mm	FTO	12-16%	15,4Ω/sq

Fig. 1: *Substrate materials used for the experiments and their properties.*

By comparing CdS buffer layers on different substrates grown under equal conditions, a dependence of the roughness of the CdS-layer on the TCO becomes apparent. CdS grown on ITO has a considerably smaller average surface finish (measured with AFM analysis software) and the CdS-layer is twice as thick (110nm) as those grown on FTO (50nm). SEM-images of CdS grown on different TCOs are shown in Fig. 2. Differences in the surface roughness are clearly visible there.
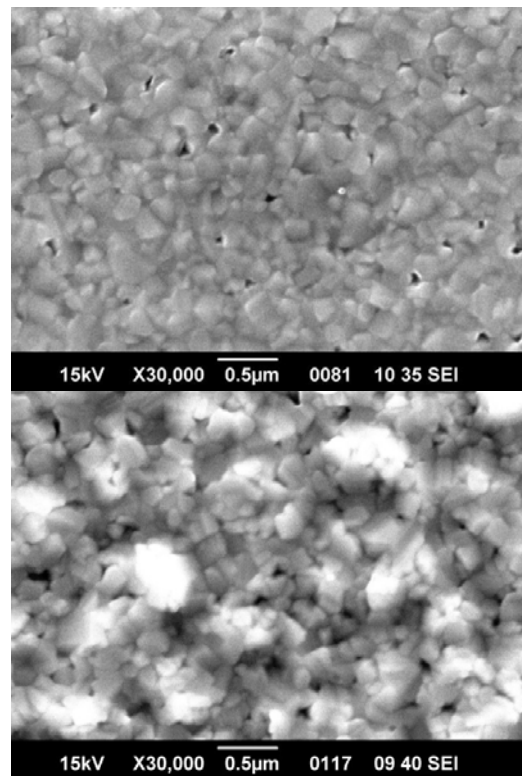
Fig. 2: *CdS on ITO-coated soda-lime glass (top) and CdS on FTO-coated soda-lime glass (bottom).*

When regarding CdTe-layers on TCO/CdS no dependence of the CdTe-morphology on the TCO can be seen. Layer properties such as grain size and layer roughness are equal on all substrates, while the CdTe layer thickness increases with increasing substrate thickness. This is an effect of heat capacity and made it necessary to establish a new heating regime for thinner substrate-glasses. Optimization of CdTe-layer thickness as well as CdS-layer thickness on thin substrates for the new regime was implemented.

Using thicker CdS-layers leads to more absorption of short-wavelength light (300nm – 500nm) which is shown in fig. 3. Higher absorption means less short-circuit current but more stable solar cells with increasing fill factors.
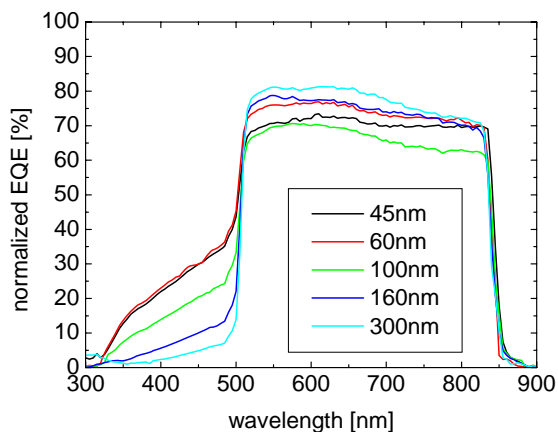
Fig. 3: *Normalized EQE spectra of solar cells with increasing CdS-layer thickness.*

Using thicker CdTe-layers (up to 10µm) leads to more stable solar cells, too. Those Solar cells produced with the new heating regime on thin (3mm) FTO-coated soda-lime glass finally showed excellent properties with conversion efficiencies of more than 8%. Especially the open circuit voltage reached more than 780mV which is 10% more than in former experiments. In a final step, activation with CdCl$_2$ for the thin (3mm) FTO coated glasses was varied to optimize CdS/CdTe intermixing. In comparison to the usual process a longer activation (40 minutes) and activation at a higher temperature (400°C) were utilized. Current-voltage measurements showed the best solar cell properties for an activation temperature of 380°C for 40 minutes (fig. 4).
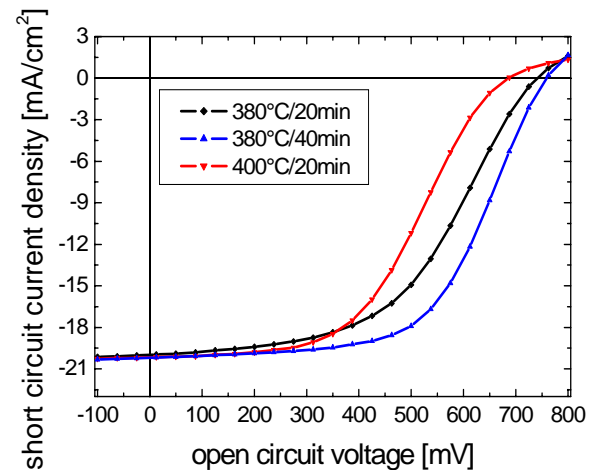
Fig. 4: *I-V characteristics of different activated solar cells on FTO coated soda-lime glass.*

Activation at temperatures of more than 400°C causes a degradation of the current-voltage characteristics while longer activation leads to better solar cell properties. After optimizing the activation step, solar cells on 3mm soda-lime-glass with FTO coating and optimized CdS/CdTe-layers yielded more than 9% conversion efficiency.

In conclusion, a new processing regime was established based on a new substrate/TCO combination. By optimizing certain process steps such as CdS-layer, CdTe-layer and activation procedure a standard was achieved that leads to reproducible solar cells with conversion efficiencies of about 9% in a low-cost close-to-industry process. Further progress should be possible using a different back contact material and an alternative for the NP-etching procedure.

References

[1] Bonnet, P. Meyers., J. Mater. Res. 13 (1998) 2740.

[2] X. Wu, J.C. Keane, R.G. Dhere, C. DeHart, D.S. Albin, A. Duda, T.A. Gessert, S. Asher, D.H. Levi, P. Sheldon, Proc. of the 17th Europ. Photov. Sol. En. Conf., Munich, Germany, October 22-26 2001, p. 995.

[3] B.E. McCandless, J.R. Sites, PV Handbook Chapter15: Cadmium Telluride Solar Cells, Wiley and Sons, 2002.

[4] A. Romeo, A.N. Tiwari, H. Zogg, M. Wagner, J.R. Günter, 2nd world conf. and Exh. on Photov. Sol. En. Conv., Wien 1998, 1105-1108.

[5] S. Mack, Herstellung und Charakterisierung von CdTe-Dünnschicht-Solarzellen, Diplomarbeit, Universität Jena, 2006

Methods for the preparation of CdTe thin film solar cells suitable for vacuum processing

C. Löffler, M. Hädrich, C. Kraft, H. Metzner, U. Reislöhner, W. Witthuhn

CdTe is a promising material for large scale manufacturing of thin film solar cells. Even though efficiencies of CdTe thin film modules do not reach the values of crystalline silicon based solar cells, they offer the great advantage of comparatively easy and low cost manufacturing in large scales. In addition to the important goal of enhancing the efficiency of solar cells, it is also of great interest to simplify the manufacturing process and thus reduce the costs.

At the Institut für Festkörperphysik (IFK) we use a baseline for CdTe thin film solar cell production which is based on an industrially applied process. As heterojunction partner for the p-doped CdTe we use n-doped CdS. CdS as well as CdTe are deposited using close space sublimation (CSS). The completion of CdS/CdTe thin films to solar cells takes two essential steps: the activation and the preparation of the back contact.

Both process steps, activation and back contact preparation, can be carried out either wet chemically or in a vacuum process. Vacuum suited processes are preferable for industrial manufacturing, as wet chemical steps require an interruption of vacuum. Therefore we investigated the performance of CdTe solar cells which where manufactured with vacuum suited methods and compared them to wet chemically manufactured samples. Morphology and chemical composition were investigated by electron microscopy (SEM) and energy dispersive X-ray spectroscopy (EDX). Solar cell characteristics were investigated employing current-voltage measurements. In the activation step the CdS/CdTe films are thermally annealed in an atmosphere containing a chlorine compound at elevated temperatures of approximately 380°C. This step is assumed to cause grain growth, doping and an intermixing at the interface between CdS and CdTe [1]. The activation using gaseous HCl takes place in a heatable glass tube (figure 1). The reactive gas consists of synthesized air (containing about 20% oxygen and 80% nitrogen) and HCl with a partial pressure of 0,1 to 1%. The samples are preheated in argon and subjected to the HCl gas as soon as the process temperature is adjusted. After the HCl process the glass tube is evacuated and the sample cools down in an argon atmosphere at about 1mbar.
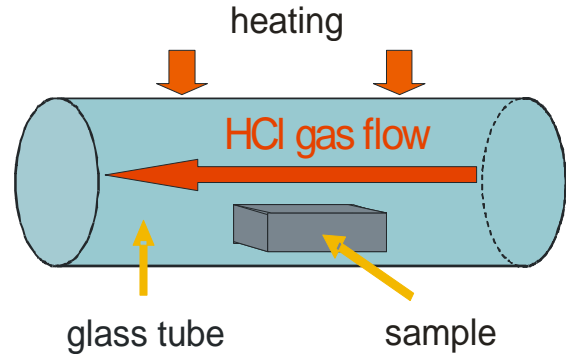
Figure 1: Heatable glass tube for HCl gas activation. The sample is subjected to reactive gas flow at elevated temperatures.

Employing EDX measurements metallic contaminations were identified and eliminated from the activation process. The samples which are discussed furthermore showed no more contaminations at the surface. For the investigation of the activation in HCl gas, different temperatures, annealing times and HCl partial pressures in the reactive gas were studied.
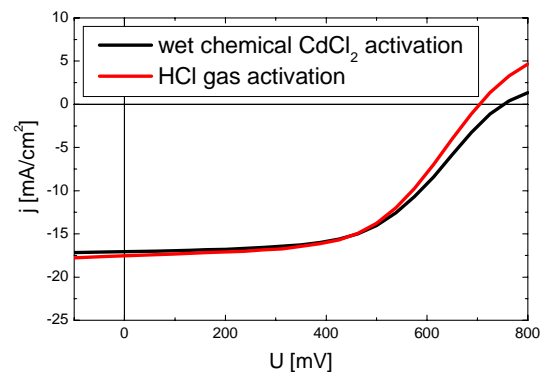
Figure 2: Current-voltage characteristics of a wet chemically activated and a HCl gas activated sample. The latter shows a lower fill factor but a higher open circuit voltage.

activation	U_{OC} [mV]	j_{SC} [mA/cm^2]	FF	η [%]
CdCl$_2$	755	18,8	0,58	8,2
HCl gas	705	18,3	0,60	7,7

Table 1: Solar cell characteristics of a CdCl$_2$ activated sample compared to a HCl gas activated sample.

Applied temperatures were varied between 360 and 410°C. The annealing time was investigated in a range from 5 to 30 minutes.

The solar cell characteristics showed the best results at about 380°C. The performance of the solar cells was only slightly dependent of the annealing time and reached a maximum at 10 minutes. The obtained solar cell performance is very similar to that of wet chemically activated samples, as shown in figure 2. The HCl gas activated sample shows a higher fill factor but a lower open circuit voltage compared to the wet chemically activated sample. By varying the partial pressure of HCl in the reactive gas, it could be concluded that with lower HCl partial pressure and longer annealing times an increased open circuit voltage can be obtained.

Due to the high work function of CdTe, the surface has to be prepared prior to the deposition of the back contact material. To achieve a good ohmic contact between the semiconductor and the metal used for the back contact, the CdTe surface is heavily p-doped or degenerated [2]. Different approaches lead to that goal. The CdTe film can be covered with a tellurium layer, either by vacuum deposition of Te or by removing the cadmium atoms using a selective etching. Alternatively, the surface can be doped with impurities like copper or by creating defect states. Plasma etching is assumed to create defect states and to remove the native oxide film located on the CdTe surface after exposure to an oxidizing atmosphere [3]. During plasma etching accelerated particles hit the surface and cause defect states and material removal. The plasma etching process was carried out as follows: The activated samples were brought into vacuum. Argon was used as etching gas at pressures between 5 and 400mbar. The etching time was varied from 3 to 20 minutes. After etching, the back contact material (molybdenum) was deposited without breaking the vacuum.

The plasma etching had a strong influence on the solar cell performance. Too long or too heavy etching respectively caused destruction of the solar cells. The properties of the etched samples depended on etching time, pressure and geometry of the setup. It was shown that it is possible to achieve a solar cell performance

in the range of that of wet chemically etched samples (figure 3 and table 2).
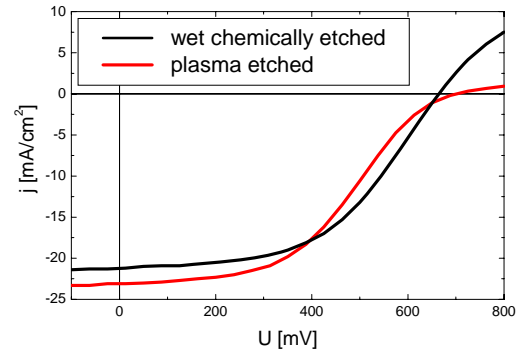
Figure 3: Current voltage characteristics of a wet chemically etched and a plasma etched sample. Both samples show a similar efficiency.

etching	U_{OC} [mV]	j_{SC} [mA/cm^2]	FF	η [%]
wet	665	21,2	0,51	7,2
plasma	700	23,1	0,44	7,1

Table 2: Solar cell characteristics of a plasma etched sample compared to a wet chemically etched sample.

In addition to only plasma etched samples we investigated a combination of wet chemical and plasma etching. Therefore we treated wet chemically etched samples with a supplementary plasma etching step. We found increased open circuit voltages when the additional plasma etching step was applied.

By EDX measurements the chemical composition of the plasma etched surface was investigated. The plasma treated CdTe surface was contaminated with oxygen, molybdenum, zinc and aluminium, which is explained by the use of these elements for other processes in the same chamber. We assume that avoiding these contaminations will lead to improved solar cell properties.

[1] M.H. Aslan, W. Song, J. Tang, D. Mao, R.T. Collins, D.H. Levi, R.K. Ahrenkiel, S.C. Lindstrom, M.B. Johnson, Mat. Res. Soc. Symp. Proc., vol. 485, AIP press [1998] 203.
[2] D. Bonnet, P. Meyers., J. Mater. Res. 13 (1998) 2740.
[3] V.Viswanathan, Studies of Cu free back contacts to thin film CdTe solar cells, PhD thesis, University of South Florida (2004)

A sequential process for manufacturing CuInSe$_2$ absorber layers for thin film solar cells

M. Oertel, Th. Hahn, H. Metzner, W. Witthuhn

With a direct band gap of 1.04 eV which can be increased by the partial substitution of In with Ga, CuInSe$_2$ is a very promising material for thin film solar cells. Actually, the best thin film solar cells with efficiencies near 20 % [1] were made of Cu(In,Ga)Se$_2$ absorber layers so far.

As cheap substrate for the solar cells molybdenum coated Soda Lime Glass (SLG) is used. The polycrystalline CuInSe$_2$ grows p-type under slightly Cu-poor and Se-rich conditions and the formation of a very thin n-type ordered vacancy compound (OVC) with slightly widened band gap (1.3 eV) on top of the layer [2] occurs which mainly forms the p-n-heterojunction. Because of the little difference of the band gaps of these layers one requires a second heteropartner with larger band gap to increase the electrical field of the junction which supports the carrier transport processes. Hence a thin CdS-layer (50 nm) is deposited on the absorber layer by chemical bath deposition (CBD). As window layer and front contact a transparent ZnO layer is deposited by RF-Sputtering. It consists of a thin intrinsic one (100 nm) and a thicker Al-doped one (350 nm).

The advantage of a sequential process of absorber manufacturing is the easy scalability of the used deposition processes, sputtering and furnace processes, to industrial scales.

Hence at IFK Jena we have set up a sputter system for sputtering Cu-In-multilayer on 50x50 mm² molybdenum coated SLG at room temperature. The number of single layers reaches up to 21 at total layer thickness of around 900 nm. The standard values of sputter parameters are 200 W sputter power and an Ar-pressure of $1.0 \cdot 10^{-2}$ mbar. Pieces of these precursor layers with 7,5x25 mm² in size are melted off in fused silica tubes with typically 50 mg of selenium under inert gas atmosphere and heated in a tube furnace up to 550 °C for 5 min 30 s whereby CuInSe$_2$ formation occurs. The investigation of the precursor and absorber layers is done by SEM-microscopy, EDX- and XRD-analysis.

In first step of establishing a base line for CuInSe$_2$ solar cell manufacturing investigation of precursor formation and influences of the sputter parameters was performed to find ideal parameters for precursor sputtering.

In Fig. 1 a cross section image of a precursor layer sputtered with standard parameters is presented. One can't see any single layers, so the assumption stands to reason that they have reacted with each other which were already reported by other workers [3]. Therefore XRD-measurements were performed which clearly show the formation of the binary CuIn-phases CuIn$_2$ and Cu$_{11}$In$_9$ during and/or immediate after sputtering (Fig.2). Single phase Cu or In exists no longer in range of traceability.
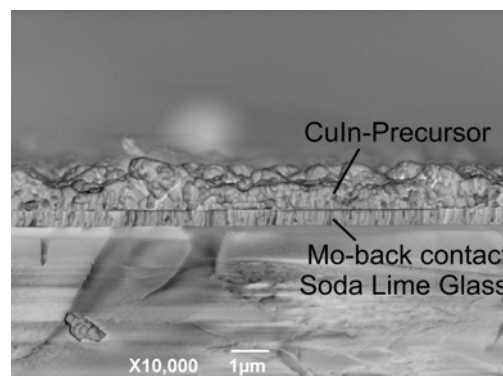
Figure 1 Cross section SEM-image of multilayer precursor composed of four Cu/In double layers and one Cu single layer on Mo-coated SLG sputtered with standard parameters.
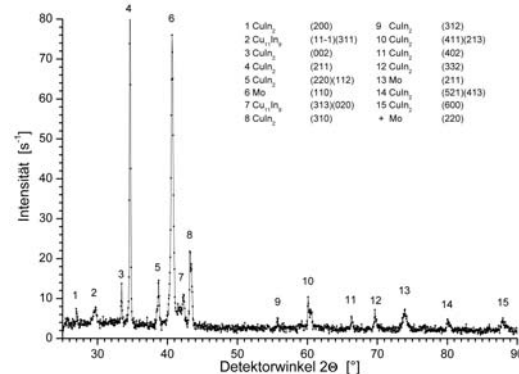
Figure 2 XRD-data of precursor presented in fig. 2.

Furthermore one can demonstrate a strong dependence of precursor morphology on sputter parameters. For investigation one parameter was changed while others were kept to standard values. A variation of pressure leads to a variation of the general multilayer morphology. It changes from a porous with large grain size distribution (300 nm to around 2 µm) on top at $6 \cdot 10^{-3}$ mbar to a closed-packed one with column-like growth with small grain sizes and a narrow distribution (200 nm to 350 nm) on top

at $1.5 \cdot 10^{-2}$ mbar. A smaller sputter power reduces the width of the grain size distribution and an increasing number of single layers lead to a higher density of the multilayer while the absolute number of atomic fraction keeps constant.

At the following selenization step both porous and column-like precursors have a high tendency to peal off the molybdenum coated SLG-substrate. So precursors with 21 single layers sputtered at standard parameters are today the optimum for $CuInSe_2$ manufacturing at the IFK.

The selenization of the precursor layers takes place in a tube furnace. The melted off fused silica tubes are moved into the heated furnace to assure high probe heating rates (around 5 °C/s). This is necessary to avoid loss of In during $CuInSe_2$ formation process by appearance of volatile InSe-phases in the temperature range between 300 and 350 °C. So, the CuInSe2 absorber layers retain the stoichiometry of the precursors. By the means of XRD-measurements (Fig. 3) one detects clearly the chalcopyrite phase of $CuInSe_2$ with strong (112)- and smaller (220)/(204)-orientation after selenization. SEM-investigation of manufactured absorber layers (fig. 4) shows large closed-packed grains with relatively plane surfaces.
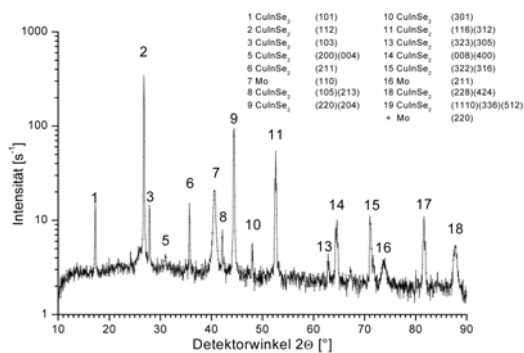
Figure 3 XRD-data of selenized standard precursor on Mo-coated SLG substrate. (The intensity is on a logarithmic scale)

Although this process line delivers promising outcomes there still are some problems to be tackled in the future. One is the reproducibility of the selenization process which is caused by sensibility of the chalcopyrite phase formation to temperature inhomogeneities and the kinetics of phase formation. Especially the kinetic of phase formation seems to be a very critical issue. This is shown by the existence of very little fraction of binary Cu_xSe_y in some manufactured absorber layers detected by the means of XRD-measurements (not shown). With a high probability these are localized at grain surfaces and boundaries. Furthermore due to volume expansion and different thermal expansion coefficients between Mo-coated SLG substrate and $CuInSe_2$ chalcopyrite phase there appear some lateral strain which causes pinholes in the absorber layers. These pinholes and the metallic binary metal-Se phases localised at grain boundaries causes short current paths in the solar cell structure which highly decrease solar cell performance (Fig. 5). In conclusion, a fast and simple process for the preparation of $CuInSe_2$ thin film absorber layers has been established. It is based on the subsequent selenization of sputtered metallic precursors with elemental Se. In face of difficulties in the process by the temperature gradients in the tube furnace the process delivers first promising results. Solar cell efficiencies near to 3 % were reached.
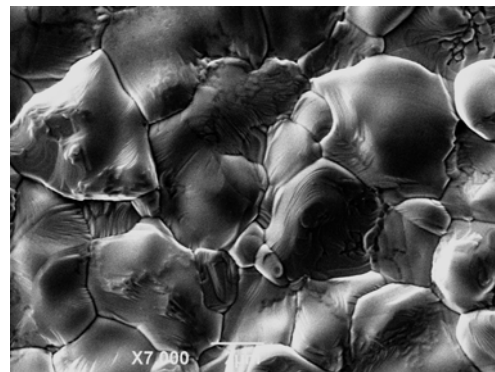
Figure 4 SEM-image of $CuInSe_2$-layer
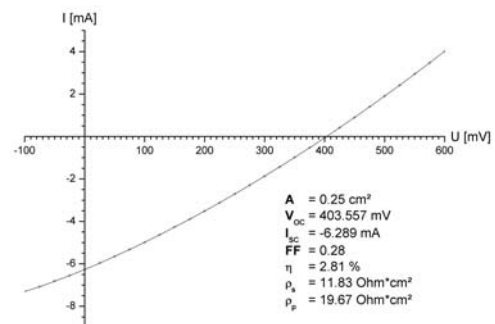
Figure 5 I-U-curve of a manufactured cell

[1] K. Ramanathan, G. Teeter, J.C. Keane, R. Noufi, Thin Solid Films 480-481 (2005), p. 499.
[2] D. Schmid, M. Ruckh, F. Grunwald, H.W. Schock, JAP 73(6) (1993), p. 2902
[3] M. Gossla, H.Metzner, H.-E. Mahnke, JAP 86(7) (1999), p. 3624

Defects in Solar Silicon (DefiS-Project)

U. Reislöhner, H. Metzner, W. Witthuhn, in collaboration with SolarZentrum Erfurt

The production of silicon based solar cells requires pure silicon. Worldwide, great efforts are made to produce silicon for solar cells in a less complex and cheaper process. A very promising possibility is the processing of metallurgical silicon. To get more insight in the quality of silicon wafers produced by different processes the project „Defects in Solar Silicon" has been started at the SolarZentrum Erfurt. In our part of the collaboration, we assumed the electrical characterization, mainly to be performed by DLTS-measurements. In addition, we carried out the implantation task using our implanter Romeo. Implantations are necessary in order to achieve defined impurity contaminations, e.g. iron, for comparative measurements. A main task of the project is to analyse the consequence of relevant processes, in particular the influence of gettering processes and hydrogen passivation, to reduce the impact of remaining defects on the efficiency of the resulting solar cells.

The following samples (all boron doped) were used for the measurements presented here:

A) Cz-Si raw wafer, not annealed.
B) Cz-Si raw wafer, annealed 30min at 850°C.
C) Cz-Si raw wafer, Fe-implanted and subsequently annealed 30min at 850°C.
D) Cz-Si raw wafer, contaminated with iron during growth, not annealed.
E) Polished commercial Fz- and Cz-Si as reference (stock material IFK).
F) Material E, Fe-implanted and annealed.

The silicon samples were cleaned in organic solvents, etched in CP6 and HF. The Schottky-contacts were produced by evaporating titanium (thickness 150nm) through a hole mask (Ø=0.5mm). A liquid InGa alloy was put onto the surface to achieve an ohmic back contact. The use of InGa results in a 10-fold higher forward current with respect to the widespread and before used Al-contacts. All samples were boron doped and admittance measurements revealed for the shallowest uncompensated acceptor level the energy $E_V+45meV$ which equals the known boron level in silicon.

Untreated samples of type A possess only an electrically active shallow acceptor concentration of $2 \cdot 10^{14} cm^{-3}$ as shown by C-V measurements. This small value is responsible for a larger series resistance R_S which causes a higher freeze-out-temperature in samples of type A (see fig. 1), when the condition $R_S \approx 1/\omega C$ is fulfilled. The less effective doping is explained by the compensating effect of thermal donors, inherent in not annealed Cz-Si. After annealing (sample type B) a doping around $2 \cdot 10^{15} cm^{-3}$ is obtained.
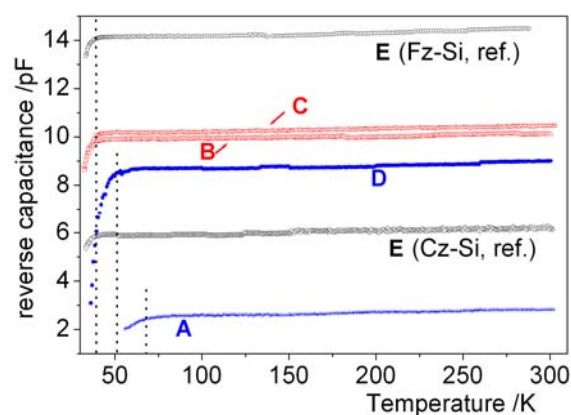
Fig. 1: The freeze out of shallow acceptors (break-down of capacitance) prevents DLTS-measurements at around 50K on samples of type A.

It is well known that a binding of iron with boron acceptors takes place during storage at room temperature after a diffusion of iron at high temperatures was performed. The resulting Fe-B pairs are stable at room temperature but start to dissociate even at
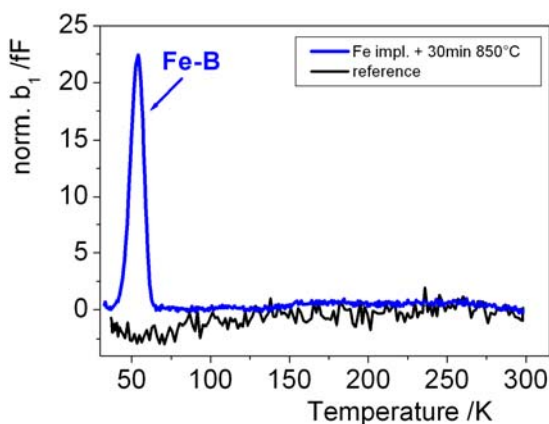
Fig. 2: The not contaminated reference sample (type E, black line) does not show any significant DLTS signal. This proves the clean contact preparation conditions at the IFK.

slightly increased temperatures. At 300°C the pairs are totally dissolved and interstitial Fe_i can be detected, if the samples are cooled down fast enough to prevent a complete reorganization into Fe-B pairs.

Using DLTS, iron was proven to be present in samples of type B, C, D, and F by the detection of a defect level at $E=E_V+80meV$ above the valence band, which fits well to energy levels published for iron-boron pairs [1]. As an example, Fig. 2 shows the DLTS signal of iron-boron pairs in a sample of type F (blue curve). The Fe-B pair concentration in samples B, C, D, and F is about $2\text{-}3\cdot10^{12}cm^{-3}$, which is the maximum value reported in literature. This indicates that the solubility limit of iron was reached. It was not yet possible to check whether iron is already present in the not annealed samples of type A, too, because the shallow doping freezes out at temperatures distinctly above 50K as demonstrated by the freeze-out step of the reverse bias capacitance shown in fig. 1.
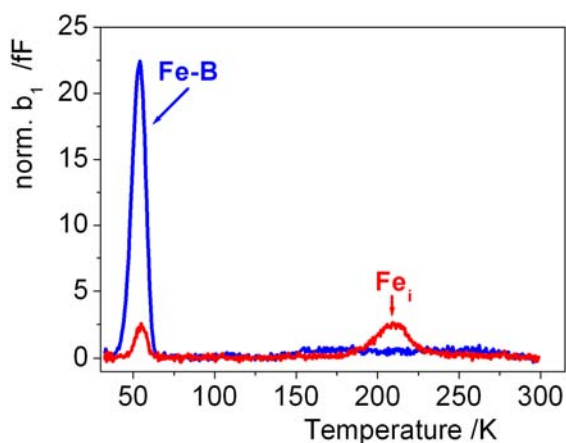
Fig. 3: The reduction of the DLTS signal at 50K and the appearance of interstitial iron after an annealing step at 300°C terminated by fast cooling to room temperature (red line) demonstrates the correct assignment to Fe-B pairs.

To further confirm the described detection of Fe-B pairs, we repeated the experiment with Fz-Si samples of type E, for which no iron contamination is expected. Indeed, no defect at all could be detected in this material, as shown in Fig. 2. This clearly demonstrates that no contamination is brought in during contact preparation at the IFK. A sample of type F, that showed again the defect level at 80meV attributed to Fe-B pairs, was annealed 10 min at 300°C in a quartz ampoule, which was filled with argon to prevent contact oxidation. The annealing was terminated by pushing the

ampoule into water to realize a fast cooling of the sample. As fig. 3 shows, the concentration of Fe-B pairs gets distinctly reduced and another DLTS-peak appears which is identified as interstitial iron.

Fig. 4 shows the DLTS-spectra of a sample type B which was annealed at 850°C at the SolarZentrum in order to suppress thermal donors and after additional annealing at 180°C for 3 min, terminated by cooling the sample to room temperature slowly within one minute. The Fe-B peak is thereby increased and further levels (not discussed here) appear. As there is no other peak correspondingly reduced in height, there has to be a source for iron beyond the visibility by DLTS which emits iron even at low temperatures.
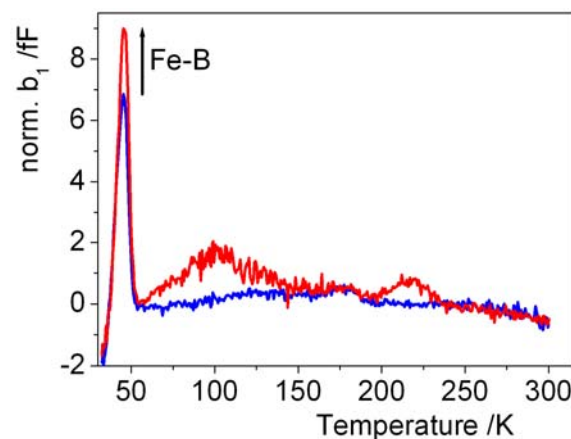
Fig. 4: After initial annealing at 850°C (blue) and after additional 3 minutes at 180°C and slow cooling to room temperature (red).

In this project we have shown the annealing step for CZ-silicon, which suppresses compensation by thermal donors, to be necessary prior to DLTS measurements in order to enable the detection of Fe-B pairs. Additionally even a short annealing step (3 min 180°C) causes a substantial rise of the Fe-B concentration. Hence, the additional iron is emitted by reservoirs which are not observed by DLTS. Therefore, all previous annealing steps have to be taken into account for comparative contamination measurements. We proved the identification of Fe-B pairs by observing the well known annealing behaviour.

[1] A. A. Istratov, H. Hieselmair, E. R. Weber, Appl. Phys. A69 (1999) 13-44

Detection of Sodium in Thin Film Layers by Nuclear Resonance Analysis

U. Reislöhner, Th. Hahn, W. Witthuhn

The most efficient thin-film solar cells are based on Cu(In,Ga)Se$_2$ (CIGS) absorber layers. A well known necessity for achieving high efficient CIGS absorbers is the incorporation of a small amount of Na with typical concentrations of 0.1 at%. However, a high concentration of sodium yields small grain sizes, porous films and is thereby damaging the cell performance [1]. Evidently, the sodium profile should routinely be measured, especially when the diffusion of sodium is influenced due to changes in growth parameters of the CIGS-layers. Such monitoring is usually performed by secondary ion mass spectroscopy (SIMS). We have tested a quite different method, first, because we haven't SIMS permanently on-hand and external routine measurements are quite expensive, second, sodium is an ideal candidate for Nuclear Resonance Analysis (NRA) as it appears naturally as isotopic pure Na-23 and several proper nuclear reactions enable a quantitative sodium analysis. We are able to generate these reactions with our own ion accelerator *JULIA* and may perform these measurements routinely. In this report, we give an account of proton induced γ-emissions, which are

A: ^{23}Na(p,p‘γ)^{23}Na   Eγ=439 keV
B: ^{23}Na(p,γ)^{24}Mg   Eγ=1368 keV
C: ^{23}Na(p,α γ)^{20}Ne   Eγ=1634 keV
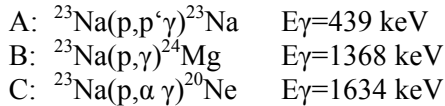
The detection of emitted particles instead of γ-quanta is also very promising but goes well beyond the scope of the experiments presented in this report.
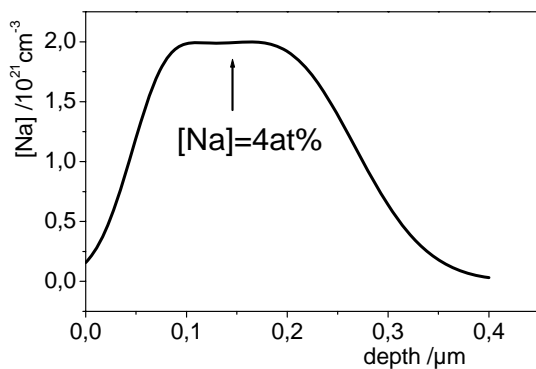
Fig. 1: Implantation profile of Na in silicon.

We used silicon samples with implanted sodium as well as NaCl on Si-substrates. The implantation profile, which is shown in fig. 1, was theoretically built up by three implantation steps with different doses and particle energies, using stopping powers calculated by the simulation software *SRIM-2006*. The implantation was finally performed with our ion accelerator *ROMEO*.
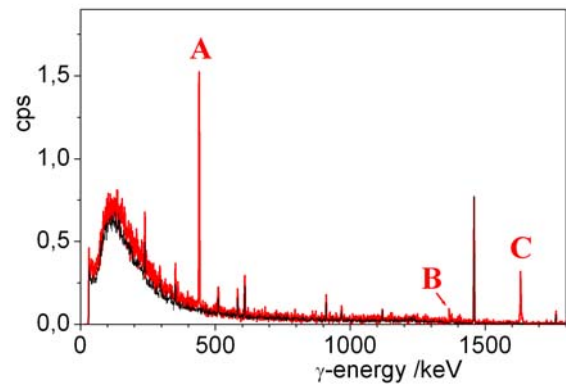
Fig. 2: γ-spectra taken during 1340keV proton irradiation (red) of NaCl on Si and without beam (black).

The samples were mounted onto the end flange of the beam line and a HP-Ge detector was positioned directly behind the flange. A typical γ-spectrum is shown in fig. 2. The largest signal is caused by reaction 'A', reaction 'B' is barely detectable and therefore useless for our purpose, and reaction 'C' reveals only a less pronounced signal due to the small detection efficiency at such high γ-energies. Bodard et al. [2] had already investigated reaction 'A' in detail and gave the number of γ-quanta as a function of the incident protons' energy for the case of a thick target, where all protons are stopped within (see fig. 3). Each step indicates the occurrence of a resonance reaction which takes place at the target surface, where the protons still posses their initial energy.

For our purpose of depth profiling we need the cross section as a function of the proton energy. Since the graph shown in fig. 3 gives in each point the integral over all γ-emissions due to (p,p'γ) reactions with proton energies below this point, we have to differentiate it to get the response for a thin sample, which is propor-

tional to the cross section we are looking for. The differentiated spectrum is depicted as dotted line in fig. 4.
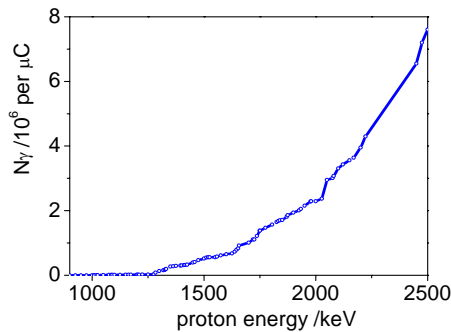
Fig. 3: Number of 439keV γ-quanta in a thick sample as a function of the incident proton energy (taken from Bodard et al [2]).

The differentiated spectrum is convoluted with the depth profile (fig. 1) to achieve the theoretically expected yield of γ-quanta for the implanted sample. The depth in the concentration profile is calculated into incident proton energy by using the stopping powers calculated by SRIM2006. The convoluted spectrum is shown in fig. 4 (blue line).
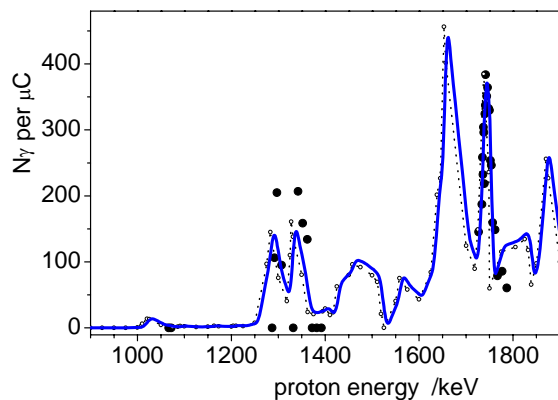
Fig. 4: Number of events of type "A" with E_γ=439keV. The dotted line is the differentiated spectrum, which is proportional to the cross section. Its convolution with the Na-profile (fig. 1) gives the blue graph. The black squares are measured results, where the proton energy was increased by 42keV which is an obvious offset of our accelerator with respect to the accelerator used by Bodard et al. [2].

Since neither the proportional constant between the cross section and the differentiated spectrum nor the normalisation of the convoluted spectrum is known, the theoretical spectra are normalised in height to the measured points

around 1700keV. The difference between the differentiated spectrum and its convolution with the depth profile is quite small, because the profile width is small compared to the width of the resonance peaks. The convolution equals in this case approximately a scanning of the cross section by a delta function. The theoretically expected number of γ-quanta fits very well to the measured results, as shown in more detail in fig 5.

The indicated shift between cross section and
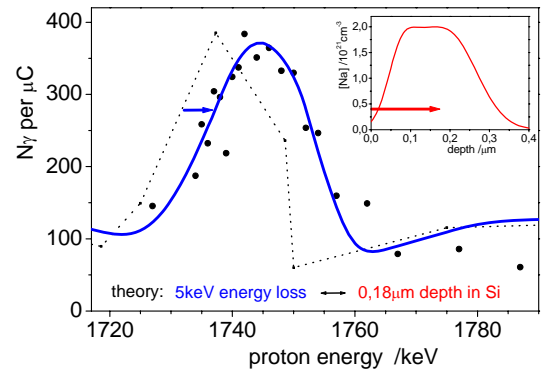
Fig. 5: Enlarged part of fig. 4 compared with depth profile (red).

its convolution with the implantation profile is generated by the energy loss of the protons until they reach the Na-profile. The shift is about 5 keV corresponding to an energy loss in 0.18μm silicon and fits well to the implantation parameters.

The detection limit could be taken from the γ-spectra. Without any optimization we achieved [Na]$_{min}$=0.1at% which equals the typical sodium concentration in CIGS layers. As our implanter is specially designed for high beam currents we can expect to get a 100-fold proton beam current after proper optimisation of the ion source. With the resulting detection limit of a hundredth of the typical Na-concentration, the sodium concentration in thin CIGS-layers could reliably be quantified. These measurements could routinely be performed, because the time for one measurement takes only about 15 minutes.

[1] D. Rudmann, thesis, University of Basel, 2004 *"Effects of sodium on growth and properties of Cu(In,Ga)Se2 thin films and solar cells"*

[2] Bodard, Deconninck, Demortier, J. Radioanal. Chem. 35 (1977) 95

Gas-phase condensation of nanometer- and subnanometer-sized carbon grains and characterization of the by-products of the condensation process

C. Jäger, I. Llamas, H. Mutschke, and F. Huisken

Nanometer- and subnanometer-sized carbonaceous materials, such as soot and polycyclic aromatic hydrocarbons (PAHs), are mainly formed via gas-phase condensation in circumstellar envelopes of carbon-rich late-type stars. The formation pathways of carbon dust particles in astrophysical environments as well as in terrestrial gas-phase condensation experiments of soot are not sufficiently understood. In astrophysical environments, PAHs represent either intermediates or side products in the carbon grain formation. Soot grains as well as neutral and ionized PAHs are discussed as carriers of various interstellar absorption and emission features including the unidentified infrared bands, the diffuse interstellar bands, the 217.5 nm extinction bump, and the blue luminescence, however, a firm identification of PAH molecules or soot grains as band carriers was not possible so far.

Carbon soots, containing PAHs and other soluble components, have been prepared by laser-induced pyrolysis of suitable gaseous precursors and by laser ablation of graphite in varying gas atmospheres. Laser pyrolysis of gas-phase hydrocarbons is not only a process which turned out to be comparable to gas-phase condensation processes in astrophysical environments but has also been shown to provide an efficient method to produce extractable components such as fullerenes, PAHs, and polyynes, together with condensed carbon nanoparticles. Based on thermo dynamical approaches, Pope and Howard [1] stated that the fullerene yield is maximized at high temperatures and low pressures, the optimum being between 1800 and 2500 K at 1 atm pressure. At lower temperatures, the pyrolysis side products are mainly PAHs, whereas at temperatures higher than 2500 K, the pyrolysis products are composed of polyyne-based compounds. In gas-phase condensation experiments, we could experimentally confirm that the formation pathways, the intermediates, by-products, and, eventually, the structure and composition of the condensed carbonaceous materials depend strongly on the temperature in the condensation zone.

In our study, we have investigated different carbon samples prepared in a low-temperature (LT) condensation regime by laser-induced pyrolysis of ethylene, acetylene, and benzene vapor with different mixing ratios using both a high- and a low-power cw CO_2 laser (800 and 60 W). High-temperature (HT) condensation experiments have been performed by laser pyrolysis using a pulsed CO_2 laser with average powers between 0.4 and 25 W and laser ablation of graphite and subsequent condensation of the grains in a quenching gas atmosphere at pressures between 2.5 and 20 torr. Nd:YAG laser pulses (5 ns) with a wavelength of 532 nm (second harmonic) were used to evaporate carbon from a rotating graphite target. The laser energies varied between 50 and 240 mJ per pulse.

High-resolution transmission electron microscopy (HRTEM) was applied to report the results on the condensation of carbon nanoparticles. Fig. 1 shows condensed nanoparticles produced in HT and LT condensation processes. Very small fullerene-like carbon nanoparticles and fullerene fragments could be observed in laser pyrolysis and laser ablation
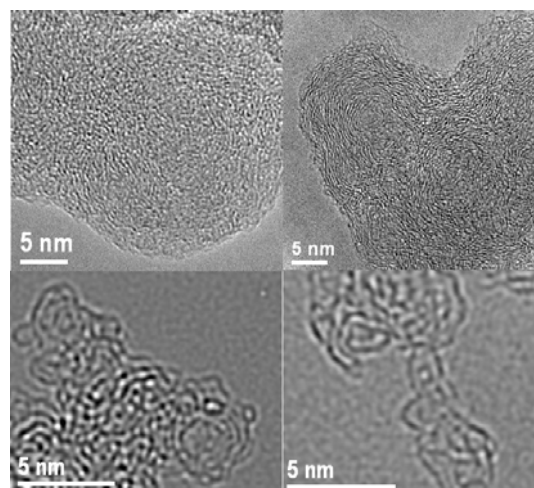

Fig. 1: HRTEM images of carbon nanoparticles. The upper two images exhibit particles produced by laser pyrolysis of benzene and ethylene mixtures in a LT condensation. The lower two panels show fullerene like carbon grains and fullerene fragments that typically condense in HT condensation regimes.

experiments performed with a pulsed laser resulting in high power densities of 4.0×10^7 to 9.0×10^9 W/cm^2 in the evaporation and condensation zone. We could outline the role of fullerene fragments as precursors for fullerene-like carbon nanoparticles [2].

In LT condensation regimes of carbon soot, the formation pathway is completely different. The condensed particles are much larger and the graphene layers are rather plane and much longer compared to the HT condensates. Interestingly, LT condensates consist of soot grains and large amounts of PAHs. In the LT regime, the amount of PAHs depends on the temperature. The lower the temperature the higher is the fraction of PAHs. Obviously, the formation process of the grains starts with small PAHs and larger PAHs are the building units for the growth of larger grains.

In circumstellar birthplaces of carbonaceous materials, PAHs and carbon soot result from one and the same gas-phase condensation process. Therefore, the analytical characterization of the PAH mixtures obtained in laboratory condensation experiments helps to understand the interstellar PAH mixtures. For an analytical characterization, we have extracted the soluble components by soxhlet extraction of the soots in toluene. Mass spectrometric characterization of the toluene extract has shown a distribution of PAHs with masses ranging from 152 to more than 650 amu [3]. The total composition of the extract was measured by a combination of gas chromatography and mass spectrometry. It has been found that the extract contains more than 64 different polycyclic aromatic hydrocarbons (PAHs). The most abundant PAH molecules are those containing 3 to 5 rings. Furthermore, we have used high-performance liquid chromatography (HPLC) to separate and identify the individual PAHs and to obtain quantitative information on the ratio between high- and low-mass PAHs [4].

In Fig. 2, HPLC chromatograms of 4 soot extracts are compared. For a better comparison between low-mass and high-mass PAHs in the different extract samples, the phenanthrene signals of all samples were normalized to the same height. The samples CP85a, CP57, and CP27 have been generated at a laser power of 650 W corresponding to a power density of 5200 W/cm^2, but with different precursor gas ratios.

The sample FK1 has been condensed at a very low laser power of 60 W (850 W/cm^2).

The total amount of aromatic soluble components depends on the temperature in the condensation zone whereas the ratio between high- and low-mass PAHs is influenced by both, the temperature and the precursor gases.

The extracted tar-like PAH mixtures will be used as a source for the preparative separation of individual compounds. For this purpose, semi-preparative HPLC columns can be employed to separate and purify specific PAHs from the extract. Gas-phase spectroscopy of large, astrophysically interesting PAHs in the visible will help to identify the carriers of the diffuse interstellar bands.
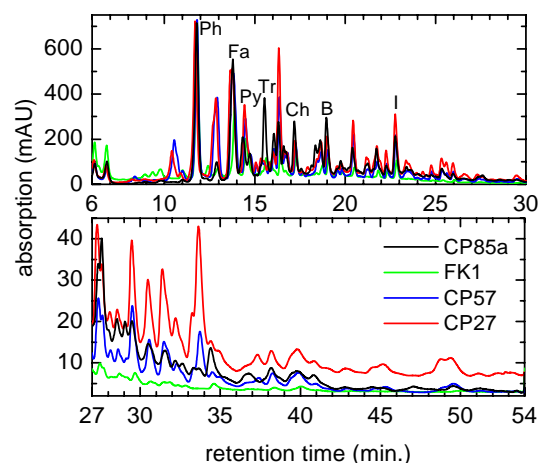
Fig. 2: HPLC of the extracts from 4 soot samples. The abbreviations mark the higher-abundance PAHs, phe-nanthrene, fluoranthene, triphenylen, pyrene, indeno-(1,2,3-cd)pyrene, chrysene, and benzo(b)fluoranthene. The astrophysically interesting high-mass PAHs appear after 24 min.

Acknowledgments

References

[1] C. J. Pope and J. B. Howard, Tetrahedron **52**, 5161 (1996).
[2] I. Llamas-Jansa, C. Jäger, H. Mutschke, T. Henning, Carbon **45**, 1542 (2007).
[3] C. Jäger et al., Astrophys. J. Suppl. Ser. **166**, 557 (2006).
[4] C. Jäger et al., Carbon **45**, 2981 (2007).

Laser vaporization of solid samples for absorption spectroscopy of jet-cooled molecules

M. Arold, G. Rouillé, Th. Henning, and F. Huisken

A number of molecular species, such as polycyclic aromatic hydrocarbons (PAHs), are claimed to be present in interstellar clouds, and thus they will contribute to the interstellar absorption features in the visible and ultraviolet range. To prove this, laboratory UV-VIS absorption spectra have to be measured for such species under astrophysically relevant conditions, *i.e.*, in a collision-free environment and at low temperature. We use cavity ring-down laser absorption spectroscopy (CRDS), a highly sensitive technique, to probe supersonic expansions of rare gases seeded with the species under study, for such expansions mimic the conditions found in the interstellar medium. The principal means of transferring solid samples to the gas phase is heating. Unfortunately, this method is too inefficient for very large PAHs and, in addition, it is not suitable for species which decompose at the elevated temperatures. To overcome this difficulty, laser vaporization (or laser ablation) of solid samples is being explored as a means to seed supersonic jet expansions with such molecules in a quantity suitable for absorption spectroscopy.
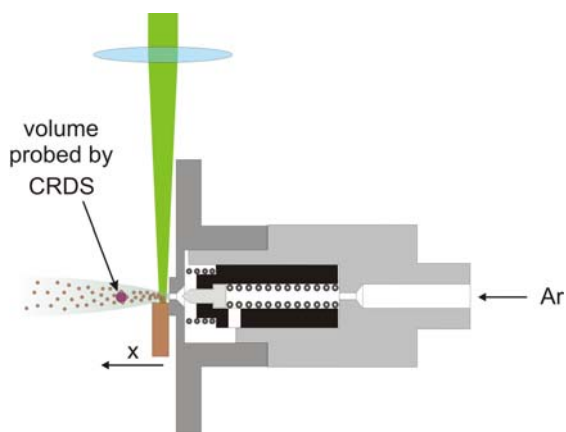
Fig. 1: Laser vaporization source with the sample (brown) in front of the electromagnetically driven pulsed valve (gray).

The solid sample, in the form of a pellet, is placed into the vacuum chamber, very close to the nozzle exit of a pulsed valve, following a design by Piuzzi *et al.* [1]. The setup used in the present study is sketched in Fig. 1. When the valve (General Valve Series 9) opens, the carrier gas (Ar) expands adiabatically above the surface of the pellet. At the same time, the focused beam from a pulsed Nd:YAG laser (Continuum Minilite 2) hits the surface of the pellet. As a result, molecules are ejected into the expanding carrier gas where they are cooled via collisions. At a variable distance x from the nozzle exit, they are probed by CRDS. In this technique, the decay of the radiation from a pulsed tunable laser at the exit of a high-quality resonator is measured. The decay time can be directly converted to an absorption cross section. Even though the quality of the resonator provides a decay time of about $10 - 20$ µs, it is sufficient to provide the sample molecules for about $4 - 5$ µs. This can be easily achieved although the laser pulse has a duration of only 10 ns.

The pellets used in this study were made by pressing approximately 600 mg of the powdered sample in a hydraulic press under a pressure of about 10 tons to form a $1 - 2$ mm thick solid disk with a diameter of 12 mm. The resulting disk is cut into 2 parts to obtain a flat surface at the edge.

Using anthracene ($C_{14}H_{10}$) as a test molecule, we have varied the conditions for laser ablation using different vaporization laser wavelengths (532, 355, and 266 nm) and fluences. In Fig. 2, the stronger bands and the weaker ones are respectively the origin band (0) and a sequence band (α) of the $S_1 \leftarrow S_0$ transition [2]. For each vaporization wavelength, the absorption signal increases with the laser fluence, and a threshold is observed for the fluence necessary to vaporize the sample. The level of this threshold decreases with decreasing vaporization wavelength. By comparison with experiments using thermal heating [3], it is noticed that the intensity of the sequence band relative to the origin band is stronger and that the band profiles are broader. This indicates higher vibrational and rotational temperatures. By varying the vaporization fluence so as to achieve very similar rotational and vibrational temperatures at all
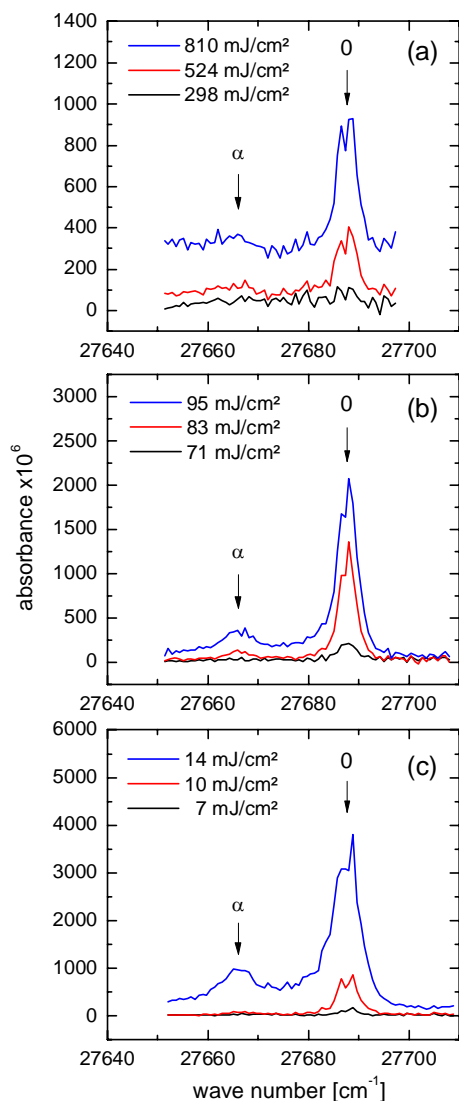
Fig. 2: Laser vaporization of anthracene at 532 nm (a), 355 nm (b), and 266 nm (c) as a function of laser fluence. The wavelength was scanned from 360.8 nm to 361.7 nm

wavelengths, it is found that the vaporization at 355 nm yields the strongest signal. Thus, the 3rd harmonic of the Nd:YAG is the best choice to bring anthracene into the vapor phase

When, as in the present case, laser vaporization is performed outside the nozzle, the process leads to higher rotational and vibrational temperatures. However, in contrast to thermal heating inside the valve, considerably less sample is consumed, making laser vaporization the preferred method if expensive or scarce samples are to be investigated in the gas phase. To obtain lower rotational and vibrational temperatures, the laser-vaporized molecules should be mixed with the carrier gas before it starts to expand, *e.g.*, inside the nozzle. We have recently built such source where the laser vaporization occurs inside the nozzle. This source is currently tested.

In order to improve the efficiency of laser vaporization, an assisting material with enhanced absorption properties like graphite can be mixed with the molecules under study. It could be shown that lower temperatures and longer pulse durations favorable for CRDS (> 10 µs) are obtained. For comparison, the $S_1 \leftarrow S_0$ origin band of fluorene was scanned using a pure sample and a pellet containing a 4:1 mixture of fluorene and graphite. Lower rotational and vibrational temperatures are observed with the mixed pellet. However the absorption signal (and the fluorene density) was 3 times weaker. This is because the evaporation of fluorene proceeds on a longer time scale.

With the laser vaporization source, we also succeeded to measure the absorption spectrum of an important biomolecule, the amino acid tryptophan. This molecule decomposes at relatively low temperatures, and laser vaporization has been shown to largely prevent its decomposition.

References

[1] F. Piuzzi, I. Dimicoli, M. Mons, B. Tardivel, and Q. Zhao, Chem. Phys. Lett. **320**, 282 (2000).

[2] A. Staicu, G. Rouillé, O. Sukhorukov, Th. Henning, and F. Huisken, Mol. Phys. **102**, 1777 (2004).

[3] G. Rouillé, M. Arold, F. Huisken, and Th. Henning, Proc. of Molecules in Space & Laboratory conference, ed. J. L. Lemaire and F. Combes (Paris), (in press) (http://www.u-cergy.fr/Mol_Spa_Lab/)

Preparation and characterization of metallic nanoparticles on substrates as catalysts for the synthesis of carbon nanotubes

Michael Blech, Bernd Schröter

Metallic nanoparticles have attracted a great interest in materials science due to their unique properties, which can be very different from that of bulk metals. Various applications have been demonstrated, including spintronics [1], biotechnology [2] and sensors [3].

It has been found that nanoparticles from transition metals such as iron, cobalt and nickel are able to catalyze the synthesis of carbon nanotubes (CNTs) by means of catalytic chemical vapor deposition (CCVD). This is associated to their electronic structure, i.e. their non-filled d orbitals, and their high carbon solubility [4]. The catalysis itself is thought to occur in the following steps: (i) Decomposition of carbon precursor, (ii) carbon solution in the catalyst, (iii) supersaturation of carbon and precipitation at particle surface, (iv) formation of CNT caps. Furthermore it has been shown that the particle size determines the CNT diameter [5]. Therefore, a crucial challenge to achieve CNTs with well-defined parameters like density and diameter is to produce catalyst particles with control over size and distribution.

A great variety of techniques has been developed in order to prepare catalyst particles on surfaces. One commonly applied approach is for example the *impregnation method*, where a solution of a catalyst precursor (e.g. iron oxalate, [6]) is coated on a support. The solvent is then evaporated and the catalyst dried.
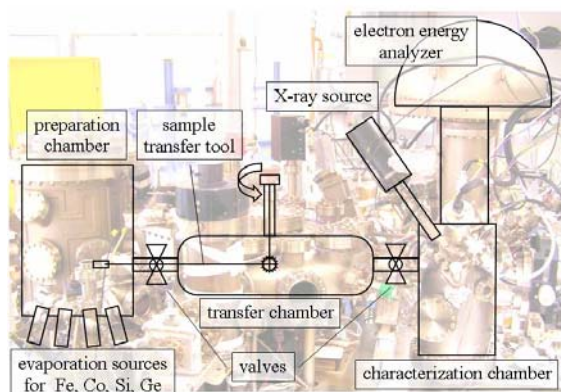
Fig. 1: UHV multichamber equipment for nanoparticle preparation and characterization by angular dependent X-ray photoelectron spectroscopy (XPS).

In our group, the preparation of catalyst layers is performed in an ultra high vacuum (UHV) multichamber arrangement with the possibility

of in-situ characterization via X-ray photoelectron spectroscopy (XPS), see Fig. 1. Thin films of iron or cobalt, with a thickness of about one monolayer, are deposited on the substrates, usually silicon dioxide (SiO_2) or sapphire (Al_2O_3), by means of thermal evaporation from effusion cells. Various experiments to prepare nanoparticles have been performed, e.g. heating the samples under UHV conditions or in air. Additionally, the development of catalyst particles during the CVD process, as it is described in Ref. 7, has been simulated by heating samples in the CVD reactor under atmospheres of hydrogen and/or argon. The single crystalline sapphire substrates have been annealed in air prior to the catalyst deposition in order to achieve atomically flat terraces. This should elucidate the influence of the crystalline surface on the catalyst behavior.
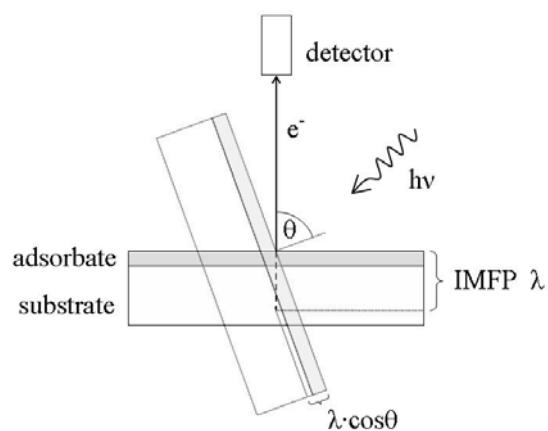
Fig. 2: Angular dependent XPS measurements. The information depth determined by inelastic mean free path λ decreases with increasing escape angle relative to surface normal.

Characterization with XPS provides information about the chemical composition of the sample surface as well as the chemical environment of each element, e.g. state of oxidation. Furthermore, it allows a quantification of the amount of deposited catalyst material, i.e. layer thickness and surface coverage. Conclusions about the surface morphology, for example a distinction between two-dimensional layers and separate nanoparticles, can be drawn by angular dependent XPS measurements (Fig. 2, 3).
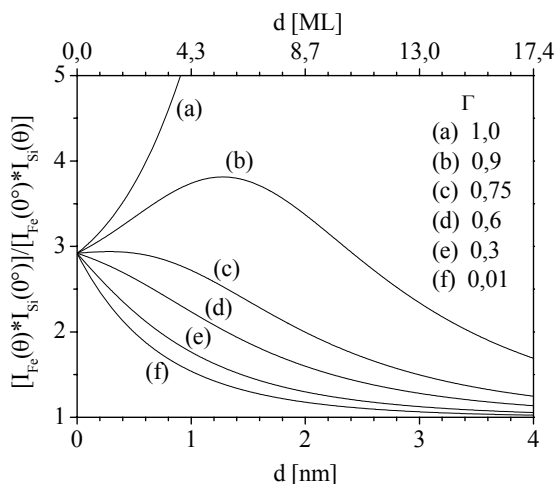
Fig. 3: Theoretical dependence of intensity ratio $[I_{Fe}(\theta)\cdot I_{Si}(0°)]/[I_{Fe}(0°)\cdot I_{Si}(\theta)]$ on layer thickness d for Fe on SiO$_2$ for different coverages Γ and $\theta = 70°$.

Further characterization occurred by means of atomic force microscopy (AFM), which revealed the topography and roughness of the sample surface plus nanoparticle sizes, size distribution and density.

As mentioned above, some experiments have been accomplished in order to investigate the development of the catalyst during CVD. Therefore, the process was aborted after several stages, of which two are of particular interest: (i) Reduction of catalyst under H$_2$ atmosphere (5min, 90mbar) and (ii) heating under H$_2$ and Ar (5min, 90 + 210mbar). After this second stage of catalyst preparation, the methane inlet starts the CNT growth during the standard CVD process. The following results have been obtained starting with an iron layer of about 0,5nm thickness on SiO$_2$. Similar tendencies were observed using sapphire substrates or cobalt as catalyst material.
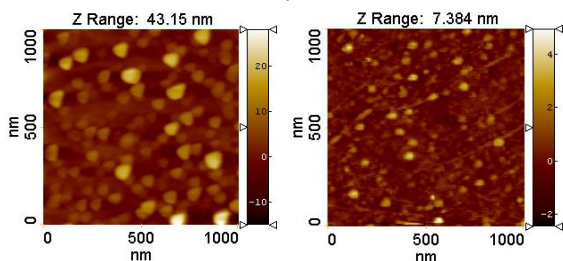
Fig. 4: AFM images of Fe nanoparticles on SiO$_2$
left: after H$_2$ reduction
right: after further heating under H$_2$ and Ar

AFM measurements have shown that heating under H$_2$ breaks the catalyst layers and leads to relatively large particles with a mean height of about 8nm (Fig. 4). Hydrogen at high temperatures is supposed to reduce metallic oxides to the metal state and thus improve their catalytic activity [4]. This reductive effect could not be verified because of the absence of in-situ characterization. However, it has been shown by XPS that heating under UHV-conditions at comparable temperatures reduces Fe$_2$O$_3$ to FeO.

By further heating under H$_2$ and Ar the particle size decreases to a mean height of about 2nm, which is suitable for the growth of single-walled carbon nanotubes (SWCNTs). This was verified by XPS measurements which show a decrease in intensity of the Fe2p spectral lines and additionally reveal a decreasing surface coverage. In contrast, there is no significant decrease in particle density (Fig. 5).
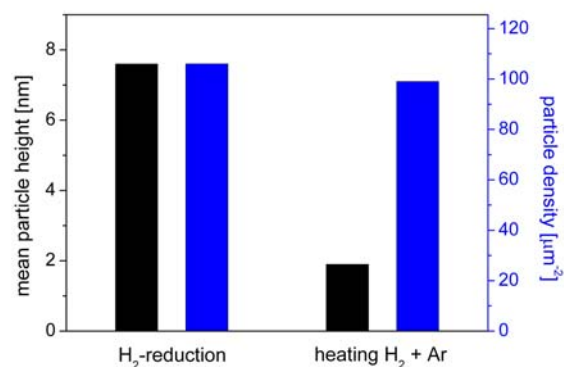
Fig. 5: Mean particle height and number density after reduction under H$_2$ and further heating under H$_2$ and Ar.

Experiments are in progress in order to prove the results for other types of substrates and catalyst materials, too. Further investigations are in progress to better control the nanoparticle parameters like size, number density and size distribution.

References:
[1] A. H. MacDonald et al., Nature Mater. **4**, 195 (2005)
[2] M. Sarikaya et al., Nature Mater. **2**, 577 (2003)
[3] D. Grosso et al., Nature Mater. **3**, 787 (2004)
[4] A.-C. Dupuis, Mater. Sci. **50**, 929 (2005)
[5] Y. Li et al., J. Phys. Chem. B **105**, 11424 (2001)
[6] V. Ivanov et al., Chem. Phys. Lett. **223**, 329 (1994)
[7] M. Steglich, Diploma thesis (2007) and elsewhere in this annual report
[8] M. Blech, Diploma thesis, 2007

Growth and characterization of carbon nanotubes on 6H-SiC(000-1) surfaces

Alexander Hartung and Bernd Schröter

Various characteristics of carbon nanotubes (CNTs) are already known but a reproducible growth process to control all these properties is still missing. The established growth processes as arc discharge, laser ablation and chemical vapour deposition produce CNTs in sufficient quantities but without any selectivity in diameter, chirality, alignment or position which is essential for commercial applications.

In search of such a process, the growth of CNTs on the carbon face of silicon carbide (SiC) could potentially pick out some of these parameters. Simple heating of this single-crystalline surface at temperatures above 1600°C can lead to a film of close-packed CNTs perpendicular to the surface [1]. There is the assumption that under certain conditions the crystallographic surface orientation has a direct influence on the chirality of the carbon nanotubes. Our achievements in this field of research will be presented in the following.

One problem of the verification of CNTs is to distinguish between all possibly grown modifications of carbon like amorphous carbon, graphite or nanotubes. Because of the similar type of bonding between carbon atoms in graphite and in carbon nanotubes, all spectroscopic methods analyzing the energetic levels of electrons can hardly differentiate these carbon modifications.
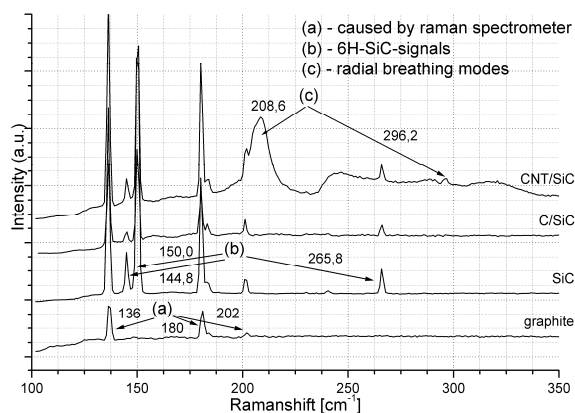
Figure 1: Raman spectra of silicon carbide, graphite and CNTs. In contrast to other carbon modifications, single-wall carbon nanotubes show characteristic radial breathing modes.
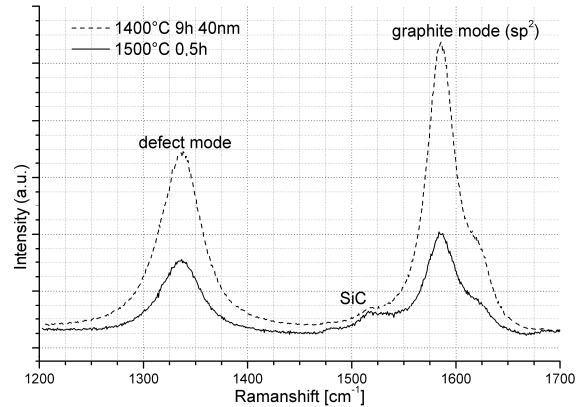
Figure 2: D- and G-mode of CNT layers on SiC(000-1) grown at different conditions. The intensity ratio of defect to graphite mode shows only a minor difference: $I_D/I_G \approx 0.65$.

The method of choice is the investigation of optical phonons with Raman spectroscopy* whose behaviour shows noticable differences for CNTs in contrast to other carbon modifications, so called radial breathing modes generated by the in-phase oscillation of atoms perpendicular to the tube axis [2] (Fig. 1).

The purity of the grown nanotube material can easily be observed by the defect mode (D) intensity of the Raman spectrum [2] (Fig. 2).

We used high-temperature hydrogen-etched SiC samples with atomically flat terraces. Heating samples at various temperatures up to 1600°C occurred in our molecular beam epitaxy (MBE) chamber at a pressure of 10^{-6} Pa or in our chemical vapour deposition (CVD) chamber at a pressure of 10^{-2} Pa. The grown carbon films were investigated with Raman spectroscopy*, scanning electron microscopy, scanning tunnelling microscopy as well as with atomic force microscopy. Depth profiles of the chemical composition were created by sputter etching in our Auger electron spectrometer.

Monitoring the surface structure during heating by reflection high-energy electron diffraction (RHEED) allows an accurate control of the growth conditions. The change from SiC to a graphitic surface occurred at temperatures above 1100°C. Higher temperatures lead step by step to a disappearance of graphite in RHEED and to a surface without diffraction pattern.

Investigations on the impact of growth temperature und duration on the layer quality indicate only a minor dependence. The quality can be specified by the intensity ratio of defect mode to graphite mode and remains at around $I_D/I_G = 0.65$ in all cases (Fig. 2).

The effect of the surface crystallinity and perfection was explored by comparing the above mentioned high-temperature hydrogen-etched SiC samples with samples sputtered by a krypton ion beam with a current density of 20 $\mu A/cm^2$ and an ion energy of 2keV. The sputtered samples reach a significant higher layer thickness of carbon compared to the hydrogen-etched samples at equal growth temperature and growth time but generate an increased number of defects with $I_D/I_G = 1.3$ (Fig. 3).

This implies that the purity of the grown nanotube material is strongly influenced by the surface conditions before Si sublimation and less by growth temperature and duration.

All attempts to grow CNTs on SiC in high vacuum rather than in ultra-high vacuum have not been successful up to now although high attention was paid to use similar substrates and heating conditions in both cases. The carbon films grown in high vacuum always consist of amorphous carbon and exhibit no graphitic structures.
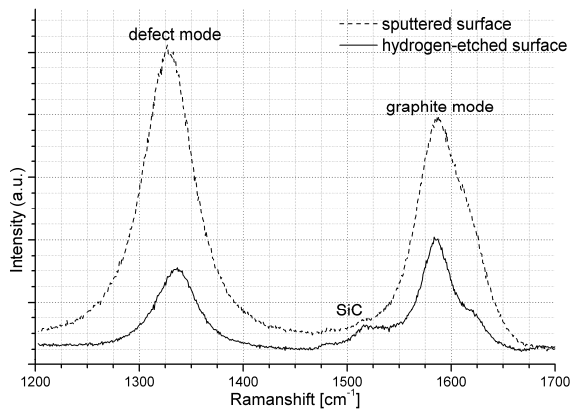
Figure 3: D- and G-mode of CNT layers on SiC(000-1) grown at equal temperature but with different surface preparation before growth. A thinner carbon layer but less amorphous carbon has been detected at the hydrogen-etched surface compared to the sputtered one.

These results are contradictory to observations published by Kusunoki et al. [1]. They reported that the additional oxygen atmosphere in the high vacuum should enhance the formation of CNTs motivated by the following chemical equation: $2SiC(s) + O_2(g) = 2C(s) + 2SiO(g)$ [3].

Furthermore, an obstruction of the nanocap formation, the precursors of carbon nanotubes, by graphite layers without defects and therefore a suppressed CNT formation has been reported in [4].

References:

[1] M. Kusunoki, T. Suzuki, T, Hirayamam N. Shibata, K. Kaneko: A formation mechanism of carbon nanotube films on SiC(0001), Appl. Phys. Lett. **77**, 531 (2000)

[2] A. Jorio, M. A. Pimenta, A. G. Souza Filho, R. Saito, G. Dresselhaus, M. S. Dresselhaus: Characterizing carbon nanotube samples with resonance Raman scattering, New Journal of Physics **5**, 139.1-193.17 (2003)

[3] T. Maruyama, H. Bang, N. Fujita, Y. Kawamura, S. Naritsuka, M.Kusunoki: STM and XPS studies of early stages of carbon nanotube growth by surface decomposition of 6H-SiC(000-1) under various oxygen pressures, Diamond Relat. Mater. (2007) doi: 10.1016/j.diamond.2007.01.004

[4] T. Yamauchi, T. Tokunaga, M. Naitoh, S. Nishigaki, N. Toyama, F. Shoji, M. Kusunoki: Influence of surface structure modifications on the growth of carbon-nanotubes on the SiC(000-1) surfaces, Surf. Sci. **600** 4077-4080 (2006)

[5] A. Hartung, Diploma thesis, 2007

Growth of Single-Walled Carbon Nanotubes by Chemical Vapor Deposition and their Characterisation by Scanning Electron Microscopy, X-Ray Photoelectron and Raman Spectroscopy

Mathias Steglich, Bernd Schröter

Carbon Nanotubes (CNTs) are in the focus of scientific interest for more than 15 years. Besides the great demand for isolated nanotubes assembled at well defined positions there are still some interesting applications for so-called CNT networks. These networks can be used as transparent and flexible electrodes or transistors in the growing field of plastic electronics, as conducting paths in flat screen monitors or as biochemical sensors.

We used chemical vapor deposition (CVD) to produce such networks of high-quality single-walled carbon nanotubes (SWCNTs) on fused quartz and sapphire substrates. Our CVD facility (see fig.1) consists of an inductively heated quartz tube furnace where we can supply different hydrocarbon gas mixtures. It allows to grow nanotubes at temperatures of 900°C typically, using argon and hydrogen as carrier gas and methane as carbon source [1].
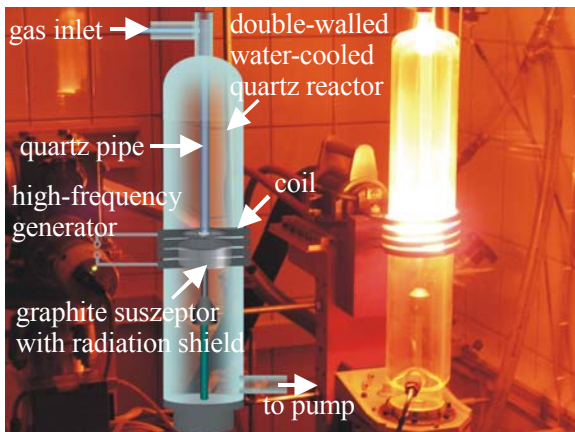
Figure 1: Our CVD facility

Before CVD a thin film of iron or cobalt (0.1-1nm) catalyst is vacuum evaporated onto the substrate. It can be patterned by lithography or direct masking. During the first stage of CVD the catalyst layer is broken up under low-pressure hydrogen atmosphere (90mbar), followed by the formation of small clusters.

XPS measurements indicate that the oxidized metal (in case of Fe) needs to be reduced in order to initiate CNT formation. Iron carbide can be measured after CVD in case of successful CNT production. Without hydrogen mostly amorphous carbon and iron oxid are observed.

By variation of CVD process parameters (partial pressure and temperature) or by changing the catalyst (Fe, Co) it is possible to achieve different CNT densities.
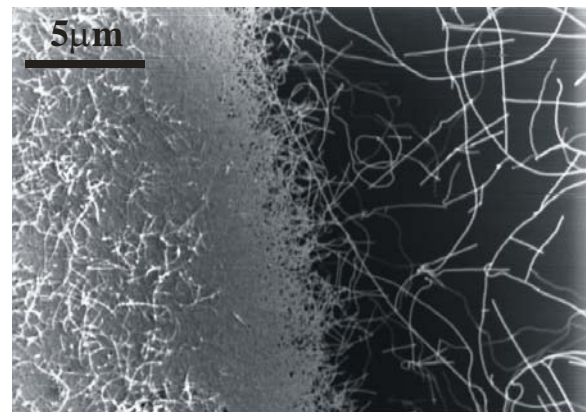
Figure 2: SEM image of SWCNTs on SiO_2 substrate with high (left) and low (right) density.

SWCNTs with diameters smaller than 2nm shouldn't be observable in conventional scanning electron microscopes (SEM) due to limited resolution. Anyhow it is possible. Atomic force microscopy measurements show the absence of bundled nanotubes. The SEM imaging is based on a special contrast mechanism. Charge transfer between the (isolating) substrate and the nanotubes can leed to a local enhanced emission of secondary electrons. That's why the CNT diameter cannot be obtained from the SEM picture. Combined measurements of SEM and Raman spectroscopy allowed us to estimate the maximum CNT yield under CVD conditions which came out to be $3.5 \cdot 10^{-16} g \cdot \mu m^{-2}$ respectively in terms of nanotube length $0.1 mm \cdot \mu m^{-2}$. The final product consists of more than 99% pure SWCNTs, less than 1% catalyst residuals and almost no amorphous carbon. The loss of metallic catalyst during CVD is based on desorption but also diffusion into the substrate cannot be excluded. The process of catalyst loss depends on the substrate material as can be seen in fig.3. The metallic nanoparticles have a

longer "lifetime" on sapphire in direct comparison with SiO$_2$.
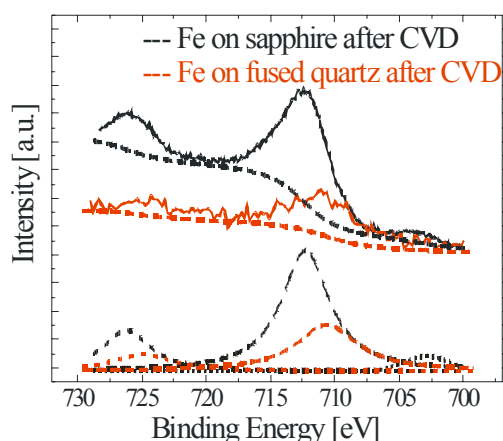
Figure 3: XPS spectrum of the Fe2p line after CVD growth. Both substrates contained the same amount of catalyst before CVD.

Raman measurements revealed the quality of our samples. The G band is typical for all sp^2 carbon modifications. By its shape amorphous carbon, graphite and CNTs can be distinguished from each other. The so-called D mode arises from defects in the graphene walls. As degree for the defect concentration the intensity ratio between D and G mode is often used. The ratio of our samples amounts about $I_D : I_G \approx 0.04$. CNTs with values smaller than 0.1 are usually designated as high quality.
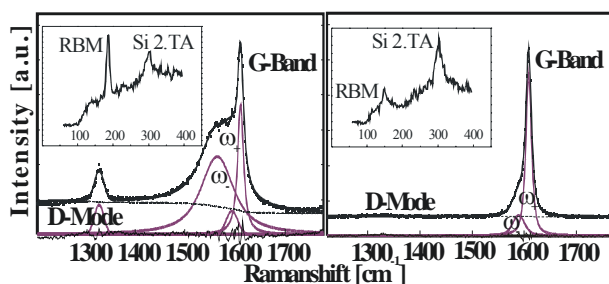
Figure 4: Raman spectra of single isolated CNTs: left: a metallic nanotube (d=1.3nm), right: a semiconducting nanotube (d=1.7nm). The differences in the G band can be clearly seen. Inset: RBM and Raman signal from the substrate used for calibration.[1]

On samples with low nanotube density we have measured Raman spectra[1] of single isolated

SWCNTs (see fig.4). The chirality (n,m) of the nanotube can be estimated using the RBM (radial breathing mode) signal, a characteristic mode of SWCNTs, and a Kataura plot [2].

There is a theoretical prediction that at the single nanotube level only metallic CNTs exhibit the D mode feature [3]. So far, this prediction could be confirmed by our measurements.

From the RBM frequency the CNT diameter can be obtained through the relation $d[nm]=248/\omega_{RBM}[cm^{-1}]$[2]. Fig.5 is showing the measured RBM signal intensity plotted over the calculated CNT diameter. This is not a real diameter distribution as it is dominated by two resonantly enhanced features at 1.3 and 1.7nm. These resonances arise from electronic transitions in metallic (1.3nm, transition E^M_{11}) and semiconducting tubes (1.7nm, E^S_{33}) caused by the He-Ne laser excitation (1.961eV). As diameter range can be stated (1.5 ± 0.4)nm.

Further analysis of the G band revealed a statistically speaking too high proportion of semiconducting CNTs of more than 66%. This could be due to hydrogen etching of metallic CNTs during CVD [4]. Anymore, spectra from CNT samples with different amounts of catalyst before CVD showed no qualitative difference. This comprises especially the diameter distribution indicating that CNT growth under these conditions is not initiated until the right size of catalyst particles is reached. (There is a close connection between the cluster size and the CNT diameter.)
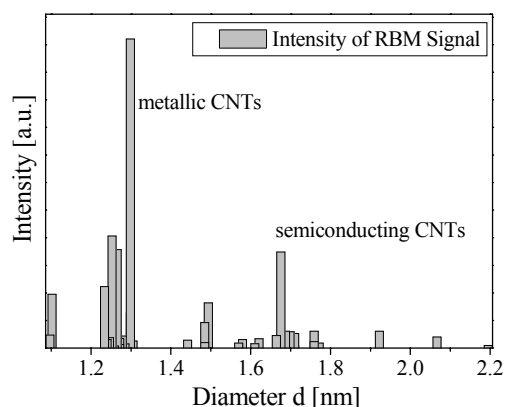
Figure 5: Mesured intensity of the RBM signal over CNT diameter.

References
[1] M. Steglich, Diploma thesis, FSU Jena 2007
[2] M. S. Dresselhaus et al., Carbon 40, 2043-2061, 2002
[3] J. Maultzsch et al., Physical Review B64, 121407, 2001
[4] A. Hassanien et al., Nanotechnology 16, 278-281, 2005

---

[1] We gratefully acknowledge the cooperation with the Astrophysics Institute and the IPHT Jena in the field of Raman spectroscopy.

Treatment of Carbon Nanotubes on Oxide Substrate Surfaces

Manuela Janietz, Bernd Schröter

Carbon nanotubes (CNTs) are carbon allotrops with unique properties [1]. Their thermal stability and extreme tensile strength make them a very promising material for electronic devices and sensors as well as biological applications like artificial muscles.

In order to combine these properties with those of other materials it becomes necessary to functionalize the CNTs.
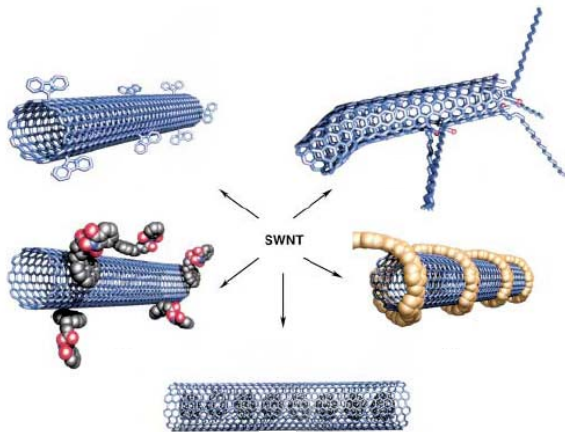
Figure 1: Various ways of carbon nanotube functionalization [2]

There are several ways of functionalization: functional groups can be attached both covalently and non-covalently to CNT sidewalls, caps or defects. Even endohedral functionalization is possible.

Depending on the synthesis method, the starting material often contains residual metallic nanoparticles and amorphous carbon which makes a purification inevitable.

An established routine comprises oxidation in air at 350°C to remove amorphous carbon. After this, catalyst particles are dissolved in hydro-chloric acid and the tubes are annealed at 900°C under vacuum condition.

Analyses were carried out with scanning electron microscopy (SEM), X-ray photoelectron (XPS) and Raman spectroscopy[*].

The success of a purification treatment as described above is shown in figure 2: Heating in air at 300 °C completely removed amorphous carbon. The presence of oxygen is necessary to form carbon monoxide and dioxide.
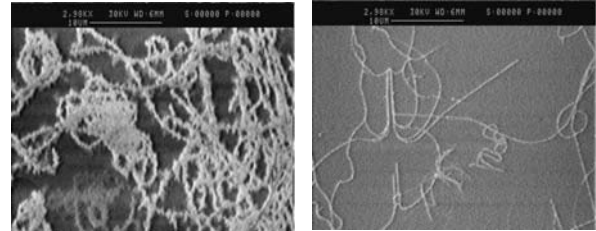
Figure 2: SEM images showing removal of amorphous carbon by heating samples in air

XPS provides information about bonding states and morphology of a sample surface. Also functional groups are detectable.
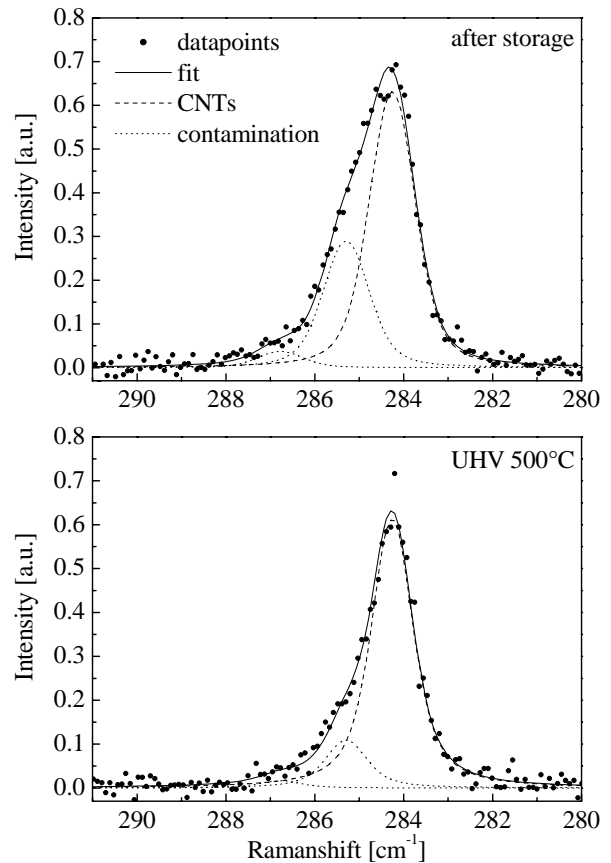
Figure 3: XPS carbon C1s peaks showing a decrease of contaminations due to heating in UHV
Above: CNTs and contamination after storage in air
Below: After heating at 500 °C in UHV

Figure 3 shows changes in the composition of the XPS C1s peak caused by heating in ultra-high vacuum (UHV): CNTs are not affected but the amount of hydrocarbon and oxygen-containing contaminations is reduced.

Raman spectroscopy is the most common characterization tool for nanotubes since their electronic and phonon properties can be investigated fast and nondestructively.

Raman spectra of CNT samples (figure 4) typically allow to distinguish between carbon modifications like amorphous carbon or fullerenes and even between single- and multi-walled CNTs. Also the defect concentration can be estimated using the disorder induced D-band at $1330\,cm^{-1}$. The G-band at around $1580\,cm^{-1}$ results from tangential vibrations. In case of metallic nanotubes the peak of vibrations along the circumference is broadened and shifted towards lower energies. So not only the quantification of CNTs but also the distinction between metallic and semiconducting tubes is possible by analyzing the G-band.

It has been found that a gas-phase plasma reaction selectively etches metallic nanotubes, retaining semiconducting tubes in near-pristine form [3]. To verify this result a sample was treatened with H_2 at $1000\,°C$. Figure 4 shows the narrowing of the G-band due to reduction of the metallic component. In addition the D-band decreases, proving the purification effect of this treatment.
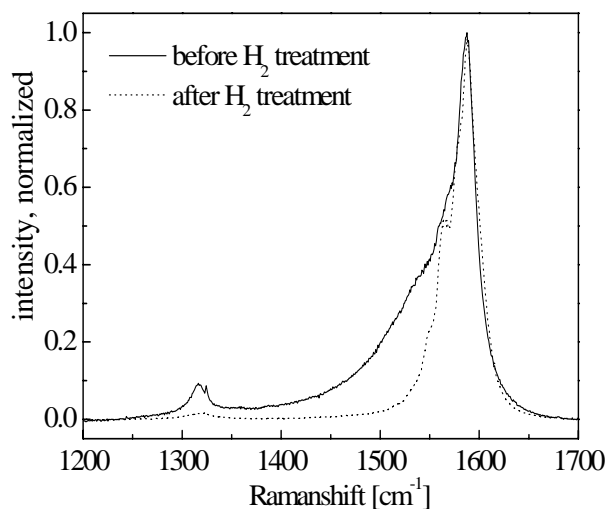
Figure 4: Raman spectra* showing G-band narrowing due to H_2 treatment

In order to bind functional groups covalently, it is necessary to attach defect groups to the CNTs, which can be substituted later. There are two common ways to induce for example carboxyl groups (-COOH): oxidation in air at elevated temperatures or treatment with acids, mainly nitric acid. The first alternative is not suitable for CNTs on substrates because of their great loss at temperatures above $400\,°C$.

However, after sonication in nitric acid (68%) for ten minutes some 3 % of the carbon atoms have bound carboxyl groups (figure 5).
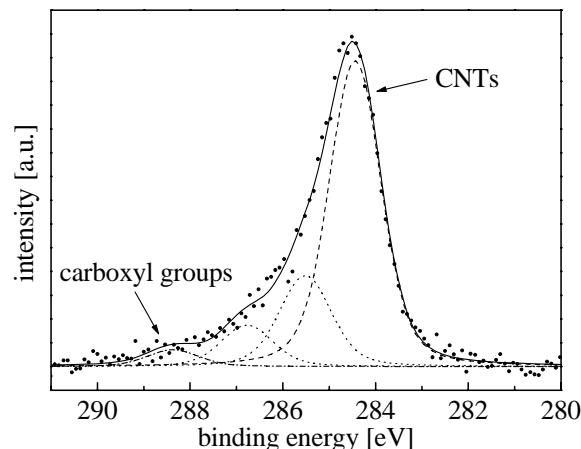
Figure 5: XPS C1s peak after sonication a CNT sample in nitric acid showing carboxyl groups attached to CNTs

Studying further functionalization steps and developing applications of functionalized CNTs such as biochemical sensors will remain future challenges.

References:

[1] M. S. Dresselhaus, G. Dresselhaus, and P. Avouris, Carbon nanotubes: Synthesis, Structure, Properties and Applications, Berlin, Springer-Verlag, 2001.
[2] A. Hirsch, Angew. Chem. **114** Nr. 11 (2002) 1933
[3] G. Zhang, P. Qi, X. Wang, Y. Lu, X. Li, R. Tu, S. Bangsaruntip, D. Mann, L. Zhang, H. Dai, Science **314** (2006) 974
[4] M. Janietz, Diploma thesis, 2007

Growth and characterization of carbon nanotubes and graphene layers on SiC(0001) surfaces

Reinhard Volkmer, Bernd Schröter

Silicon carbide (SiC) has excelled as a promising substrate for the growth of graphene and carbon nanotubes (CNT) as it provides a clean, catalyst-free surface, which is advantageous for the utilization of the CNTs in future nanoelectronics and nanooptics applications. Annealing SiC samples in ultra-high vacuum (UHV) at increasing temperatures leads to a surface decomposition silicon evaporation leaving a carbon-rich surface. Depending on the substrate polarity, the very thin layers of graphite (so-called graphene) that emerge on top of the crystalline SiC can alter into CNTs with their tube axis perpendicular or parallel to the surface in the case of $(000\bar{1})$ C face or (0001) Si face orientation, resp. [1,2].

Our preparation of $SiC(0001)$ substrates that form a suitable basis for the growth of graphene and CNTs starts with high-temperature hydrogen etching resulting in clean, atomically flat terraces on the surface. Afterwards, designated surface reconstructions can be obtained by heating the samples under a tunable silicon vapor flux, and verified by low energy electron diffraction (LEED) in our multi-chamber UHV facility (fig. 1). After the SiC (1×1) pattern has vanished due to heating to about 850°C, a silicon-rich (3×3) surface structure appears which converts into more carbon-rich structures during further annealing

Figure 2:

LEED patterns of SiC(0001) after several annealing steps.
a) (3×3)
b) $(\sqrt{3} \times \sqrt{3})R30°$
c) $(6\sqrt{3} \times 6\sqrt{3})R30°$

before the (1×1) graphite lattice eventually becomes visible (fig. 2).

In addition to LEED, X-ray photoelectron spectra (XPS) and scanning tunneling microscopy (STM) at atomic resolution have proved that the annealing pocedure produces sp^2-bonded carbon in the form of graphene sheets on top of the SiC substrate. Graphene has also been observed in the form of folded layers with graphitic lattice structure by STM (fig. 3) [3].
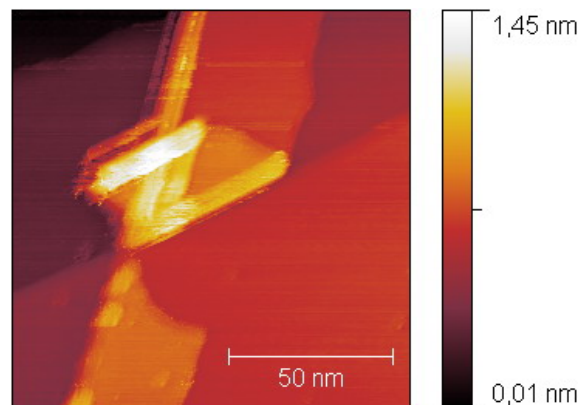
Figure 3: Folded sheets of graphene grown on SiC by high temperature annealing in UHV.

Figure 1: UHV multichamber equipment for surface preparation and characterization by STM, XPS and LEED.

At temperatures above 1500°C, CNTs could be produced on samples with different polytypes

and surface cutting angles, and afterwards investigated by in-situ and ex-situ STM (fig. 4).
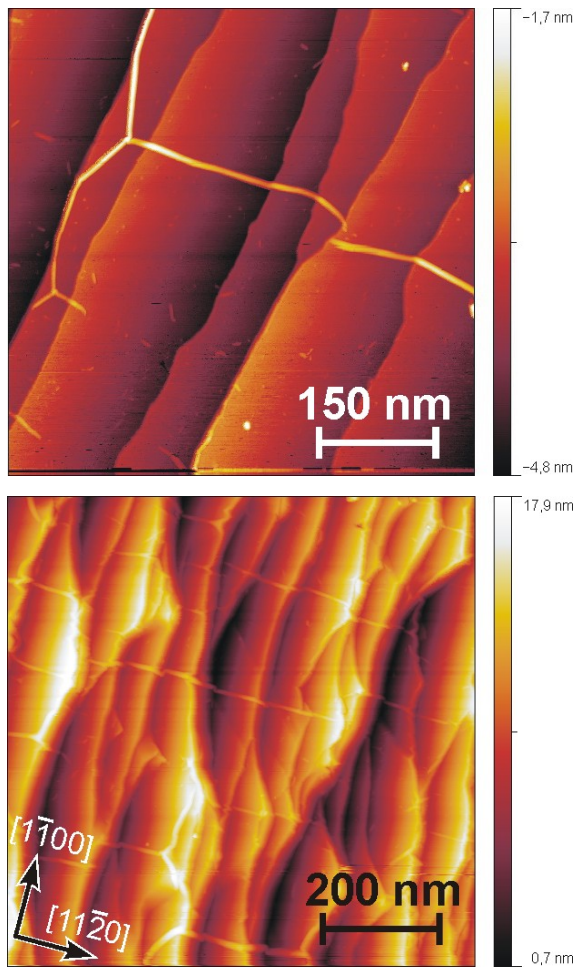
Figure 4: STM images of SiC surfaces covered by an ultra-thin graphite layer. The narrow bright lines indicate CNTs lying on top. CNTs occurred on on-axis (upper image) as well as on off-axis substrates.

We have not found CNTs on each SiC sample prepared as described, which could mean that the growth process may only take place in a small range of conditions.

Nevertheless, we have grown CNTs on both 4H and 6H substrates without any obvious differences in nanotube characteristics.

The strings at the surface we have viewed by STM, and which we consider to be either single CNTs or bundles of CNTs, usually show a height distribution between 1nm and 4nm, and are between 6nm and 15nm wide due to broadening caused by the tunneling tip.

In principle, CNTs can arrange arbitrarily on the sample surface, but there are preferred directions and places for longer, straight parts of the tubes. Often they are found to be attached to SiC step edges, or realign at edges during the imaging scan process. A further preference for tube alignment is given by the substrate's honeycomb lattice. It results in six favored directions with an angle distance of 60°. Further, it gives rise to typical CNT Y-junctions with 120° between each arm that we have found on all CNT samples (fig. 5). These junctions might be of particular interest as building blocks for potential electronic networks on a nanoscale.
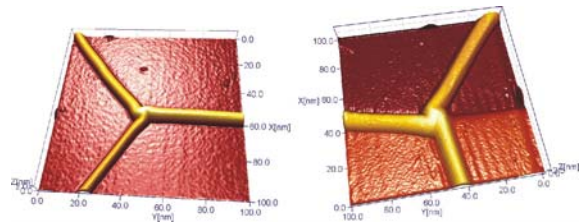
Figure 5: STM images of typical Y-junctions of CNTs grown on SiC surfaces on flat terraces (left image) and at a substrate step.

Occasionally, atomic resolution in STM has been achieved both on the substrate and on parts of a nanotube, which has enabled chirality determination to a certain degree. Improved scanning conditions would help in gaining valuable additional information about the CNTs' atomic structure and their arrangement with respect to the substrate orientation.

Most tubes turn out to be single-walled with diameters of 1-2 nm. In comparison to other techniques, CNTs grown on SiC tend to show a high purity, which results from the high growth temperature and the omission of catalysts that otherwise typically remain as defects in the tube structure.

References:

[1] M. Kusunoki, T. Suzuki, T, Hirayamam N. Shibata, K. Kaneko: A formation mechanism of carbon nanotube films on SiC(0001), Appl. Phys. Lett. **77** (2000) 531

[2] V. Derycke, R. Martel, M. Radosavljević, F.M. Ross, Ph. Avouris: Catalyst-Free Growth of Ordered Single-Walled Carbon Nanotube Networks, Nano Lett. **2** (2002) 1043

[3] R. Volkmer, Diploma Thesis, 2007

Characterization of photoconductive THz-Antennas

M. Voitsch, R. Hohmuth, W. Richter
Institut für Festkörperphysik, Arbeitsgruppe Physik dünner Schichten

Terahertz radiation has recently been rated as one of the 10 most promising technologies in the 21 century. One popular way to generate and detect THz radiation are photoconductive antennas (PCA).

PCAs are devices with two gold electrodes on top of a semiconductor surface. Possible geometries are shown in fig. 1.
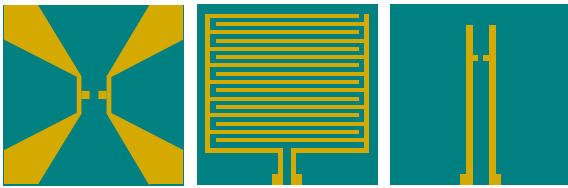
Fig. 1.possible geometries for PCA electrodes

To generate and detect THz pulses a femtosecond laser beam is focused in the gap area between the electrodes exciting free charge carriers. In emitting mode these carriers are accelerated by an external bias voltage set across the electrodes. The resulting current pulse emits electromagnetic radiation in the THz range. A couple of parameters like laser pulse duration, antenna geometry and material specifications are determing the spectrum. In detecting mode no external voltage is used. The incoming THz field is operating as a bias for the mobile charge carriers. The emerging current can be detected by a sensitive current meter. A delay line secures the temporal overlap of laser excitation and THz pulse and allows sampling of the latter. A typical THz pulse with the fourier generated spectrum is shown in figure 2.

In this work the material parameters of photoconductive THz antennas were investigated.

Two types of PCAs were manufactured using low temperature molecular beam epitaxy. Materials of choice were low temperature gallium arsenide (LT-GaAs) and a LT-In$_{0.25}$Ga$_{0.75}$As/GaAs quantum well heterostructure. The devices were grown at 270°C and 330°C respectively.
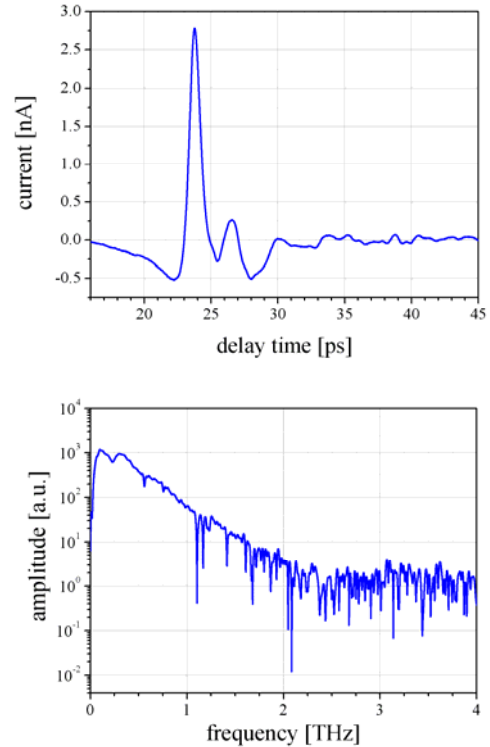
Fig. 2.Typical THz pulse and corresponding spectrum

Excitation energy

The analysis of the excitation energy of the two PCAs was based on the thermal activation of the semiconductor. For this purpose the antenna chip was applied on a TEC. The resistance of the PCA was then measured at different temperatures. The results were plotted in an Arrheniusplot shown in fig. 3.

The fit curve shows the expected dependency $R(T) = R_{0*}\exp(E_A/kT)$. Based on this fit E_A may be determined. The antenna based on the In$_{0.25}$Ga$_{0.75}$As/GaAs heterostructure and the plain LT-GaAs antenna show activation energies of 660 meV and 163 meV respectively. The key reason for the difference is not the material (E_A should be smaller for InGaAs than for GaAs) but the growth temperature. This parameter governs the type of conductivity inside the

semiconductor crystal. The LT-GaAs wafer was grown at approx. 270°C. The growth related density of defects becomes rather large at these low temperatures allowing the single defect states to overlap in their wave functions and forming a defect band circa in the middle of the band gap. [1] In this case
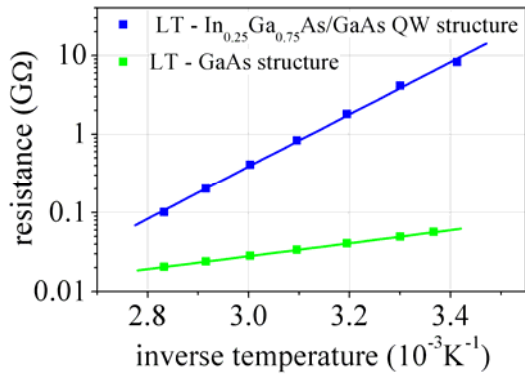
Fig. 3. Arrheniusplot to determine the excitation energy

the activation energy describes the maximum amount of energy needed by the electrons to hop from one defect to the neighbour defect. In other words the activation energy is a measure of the defect band width. The InGaAs heterostructure was grown at 330°C causing fewer defects. The formation of the described defect band is suppressed under these conditions. Hence a different type of conductivity appeared. The electrons are moving in the conduction band like in the classical picture of a semiconductor. The excitation occurred from EL2-like defect states 600-700 meV below the conduction band in GaAs.

Recombination time/ Carrier mobility

The other main parameters of the semiconductor were obtained by using optical excitation. Therefore a 532nm cw laser beam was focussed between the PCA electrodes. Again the resistance R is measured depending on the used optical power P_{opt}.
The product of charge carrier mobility μ and recombination time τ can be obtained from this curve shown in fig.4.
The slope α in this figure depends only on well known parameters like the electrode
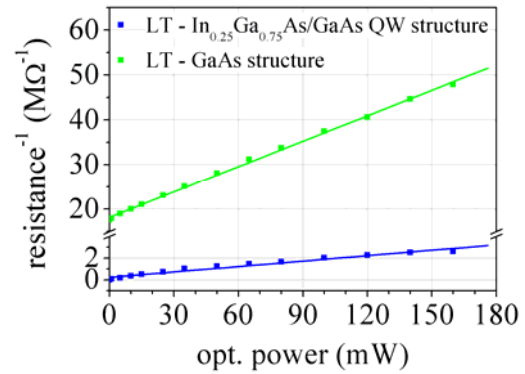
Fig. 4. Conductivity as a function of optical Power focussed on the antenna

gap distance l, the photon energy $h\upsilon$ of the laser and the mentioned product $\tau*\mu$.

$$\alpha = \frac{R^{-1}}{P_{opt}} = \frac{e \cdot \tau\mu}{h\nu \cdot l^2}$$

Unfortunately both figures can not be measured separately with this method. To distinguish the product further investigations have to be done, like Hall measurements or pump-probe experiments. From the experimental results we can determine $\tau*\mu = 2,31*10^{-9}$ cm²/Vs for the InGaAs structure and $\tau*\mu = 0,96*10^{-9}$ cm²/Vs for the plain LT-GaAs. Comparing these results with reference [2] a good agreement shows. Recombination times of 660 fs and electron mobilities of 2250 cm²/Vs are reported for GaAs grown at 250°C.

Ref.: [1] F.W.Smith: *The device applications and characterization of nonstoichiometric GaAs grown by MBE* (1990)
[2] H. Nêmec et. al.: *Carrier dynamics in LT-GaAs by terahertz emission spectroscopy* (Journal of Applied Physics 90 1306, 2001)

Growth of Carbon Nanotubes with buried catalyst films

M. Büenfeld, C. Pansow, F. Schmidl, A. Tünnermann* and P. Seidel

Institute of Applied Physics, FSU Jena

Carbon nanotubes (CNTs) are still of great interest in research although they had been discovered more than 10 years ago. The possibility of different conductivity (metallic and semiconducting behaviour) as well as different diameter and chirality give the CNTs a wide range of possible applications (e.g. optical and electrical) [1]. Additionally a nanotube can have more than one graphene layer. This circumstances increase the possible use of the carbon nanotubes. Actually, the problems to grow a specific type of carbon nanotube go up.

A lot of applications need aligned CNTs on the substrate. While many researchers try to put the CNTs as a suspension on the substrate and align them by an electrical field, we use a multilayer system with a buried catalyst film, structure this system by means of photolithography and use CCVD to grow the nanotubes [2 - 4].
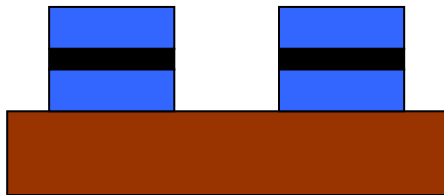
Fig. 1: scheme of the structured $SiO_2 - Co - SiO_2$ multilayer system on a substrate

The first used system of $SiO_2 - Co - SiO_2$ (fig. 1) showed diffusion of the cobalt through the upper silicon dioxide layer. Nanotubes started to grow from this layer [2]. We tried to produce a multilayer system with two cobalt layers.
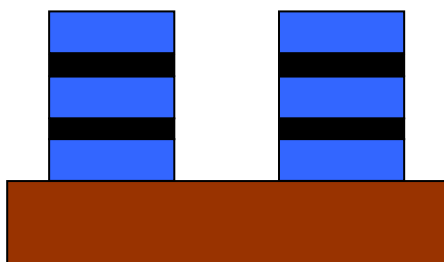
Fig. 2: scheme of the structured $SiO_2 - Co - SiO_2 - Co - SiO_2$ multilayer system on a substrate

Figure 2 shows the scheme of this system.

This system could be used in different was. At first, you can have a controlled distance of the nanotubes by the thickness of the silicon dioxide. Secondly, this system can be used to get a higher density from bird's eye view. Optical absorption could be one application.
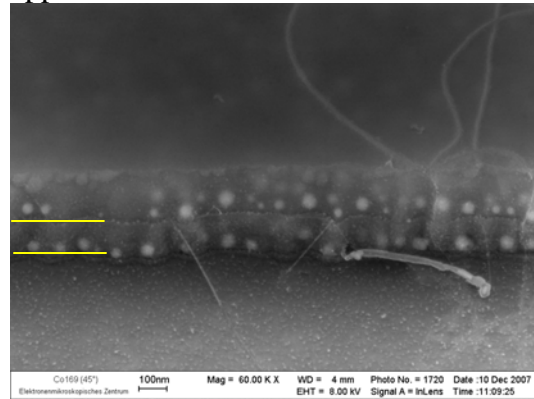
Fig. 3: SEM picture of the structured $SiO_2 - Co - SiO_2 - Co - SiO_2$ multilayer system under a tilt of 45 °. The yellow lines show the position of the two cobalt layers.

The growth behaviour is shown in figure 3. There are also nanotubes on the surface of the upper silicon dioxide layer, but the figure also shows nanotubes and nanofibers grown from the edge of the cobalt layers (yellow lines in figure 3). The nanotubes are quite short and have a low density.

To repress the diffusion of cobalt, we tried titan as a diffusion buffer.

Figure 4 shows the new layer system. The thickness of both SiO_2 layer was 100 nm each. The titan layers had thicknesses between 5 and 20 nm.
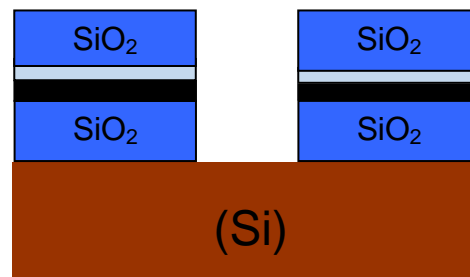
Fig. 4: scheme of the multilayer system with an additional titan layer between Co (black) and the upper SiO_2 layer (blue)

The cobalt layer had a thickness of about 1 to 3 nm.

Figure 5 shows a typical SEM picture of the used structure. The thickness of the titan layer was about 5 nm and the thickness of the cobalt layer about 1nm. Single CNTs grow from these multilayer systems, but there was no hint of CNTs starting to grow from the SiO$_2$ surface.
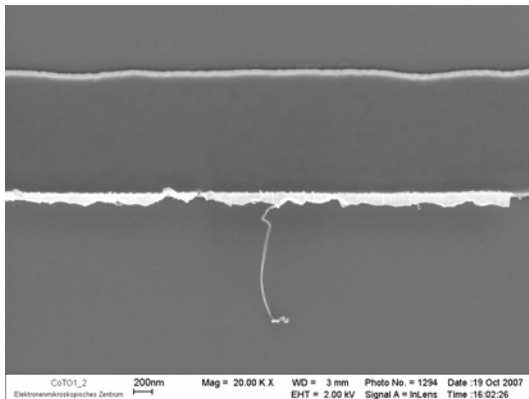
Fig. 5: *SEM picture of a short carbon nanotube by the multilayer system with titan (5nm Ti, 1nm Co)*

This shows that titan with a thickness down to 5 nm the diffusion of cobalt was repressed.

The cobalt layer was complete at a thickness of about 6 nm using thermal evaporation. Therefore cobalt layer with a lower thickness do not have to be a completely filled layer at the edge of the structure. This could be the reason for the low density of nanotubes especially with a cobalt thickness of 1 nm.

While this nanotube is quite short, figure 6 shows a nanotube on the same probe with a length of more than 2 µm. This picture shows that this layer system can produce quite straight nanotubes. The growth of the nanotube starts from the edge of the layer system.

The described multilayer systems show that aligned carbon nanotubes can be synthesized by this method. The length of carbon nanotubes (figure 6 and [2]) should allow to contact single nanotubes by means of photolithography. New masks are in preparation to study contacts with single aligned carbon nanotubes as well as arrays of aligned nanotubes.
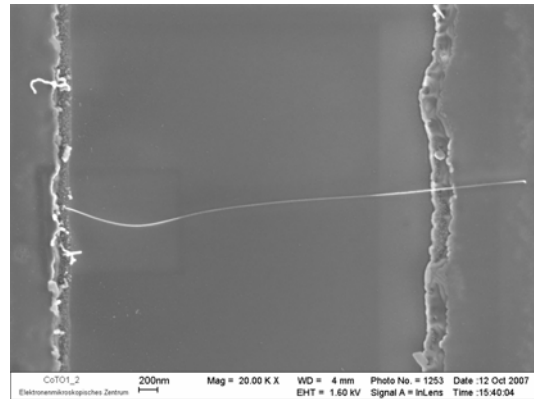
Fig. 6: *SEM picture of a long nanotube on the same probe described at figure 3*

Additionally figure 3 shows that the density of nanotubes can be increased. Optical applications with aligned nanotubes seem to be possible.

The length and the density of carbon nanotubes vary. This seems to depend on the used evaporation technology for the cobalt catalyst layer. Therefore, a new method to fabricate the catalyst layer is in progress.

References
[1] M. Anantram and F. Leonard, Reports on Progress in Physics 69 (2006) p. 507
[2] M. Büenfeld, M. Grube, F. Schmidl, A. Tünnermann and P. Seidel, Annual Report 2006
[3] Th. Reichel, H. Rudolph, M. Steglich, B. Schröter, Annual Report 2006
[4] A.-C. Dupuis, Progress in Materials Science 50 (2005) p.929

Dielectrophoretic alignment of zinc oxide nanowires using microelectrodes

A.-K. Meyer, J. Salfi*, U. Philipose*, H. E. Ruda*, P. Seidel

*Energenius Centre for Advanced Nanotechnology, University of Toronto, Canada

When a polarizable object is subjected to an electric field, a dipole moment is induced. In inhomogeneous fields, the field strength and thus the force acting on each side of the particle will be different, causing the particle to move with respect to the medium. This force is called dielectrophoretic (DEP) force and strongly depends on the frequency and strength of the ac applied electric field [DB04].

In this work, a process to fabricate microchips has been established and the dielectrophoresis (DEP) force was analyzed in respect to variations of the ac electric field and frequency. These relations were examined by aligning semiconductor zinc oxide (ZnO) nanowires (NWS) on microelectrodes.
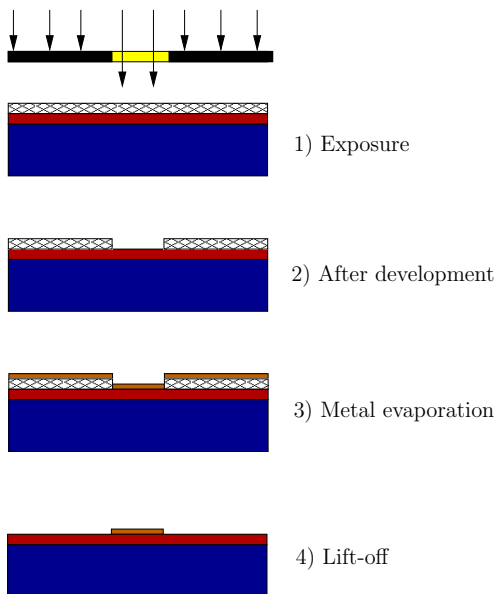
Figure 1: Schematic photolithography and lift-off sequence using positive photoresist.

1) Exposure

2) After development

3) Metal evaporation

4) Lift-off

To fabricate samples for testing nanowire assembly, metal electrodes were prepared with a standard photolithography process (see figure 1) on a thermally oxidized Si wafer. The positive resist AZ 4330 was used to transfer patterns from the mask onto the substrate.
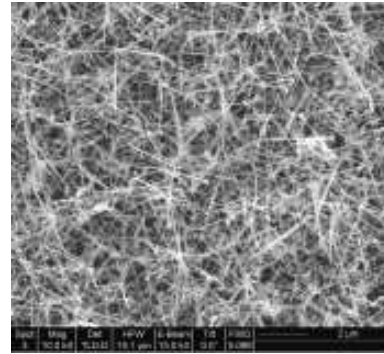
Figure 2: High magnification SEM image of ZnO wires on Si substrate. Long wires with length up to several micrometers grow.

ZnO nanowires, as seen in figure (2), were synthesized by a standard vapor phase growth method. The nanowires, about $5\mu m$ to $15\mu m$ in length and 50nm to 100nm in diameter, were immersed in methanol and ultrasonicated for 45 seconds. A drop of nanowire suspension ($\sim 5\mu$l) was then placed onto the selected gap using a micropipette, while the electric field was applied across the electrodes (one of them grounded and the other one applied with sinusoidal ac voltage). The electric field was continuously applied until the suspension completely dried out.

66

Figure 3: Alignment setup under optical microscope.

Figure (3) shows a dielectrophoresis experiment setup. Alignment experiments were conducted at frequencies between 100Hz and 10MHz and driving voltages between $1V_{pp}$ and $20V_{pp}$ (peak-to-peak) in electrode gaps of $10\mu m$ to $50\mu m$ spacing.

During alignment, ZnO NWS were trapped at electrode edges and aligned along the electric field lines. Longer nanowires even bridged across electrode gaps. Figure (4) shows an optical microscopy picture of aligned nanowires.
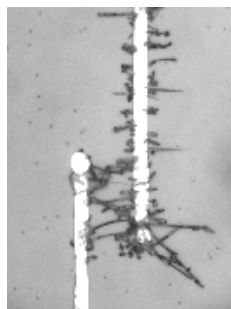
Figure 4: Aligned ZnO NWS between electrodes of $15\mu m$ spacing at $U=20V_{pp}$ and f=1MHz.

It is known that ZnO nanowires generally behave as an n-type semiconductor [LZML06].

Figure (5) shows the current-voltage characteristic of a set of trapped ZnO nanowires measured in the dark and under UV light exposure with an HP4140B picoammeter. Its nonlinear curves are typical for a semiconducting nature and resemble those of a rectifying diode.When having turned on the lamp, free carriers were generated inside the nanowire by absorbing the incident light, of which the photon energy is higher than the bandgap of the ZnO nanowires ($E_g = 3.37eV$ [LZML06]). The resulting shift of the I-V curve in figure (5) indicates the amount of photocurrent being generated.
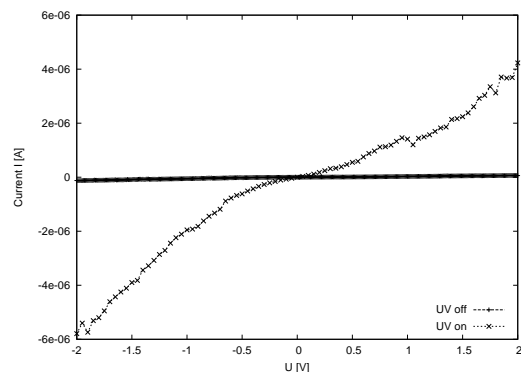
Figure 5: Current-voltage characteristic with and without UV-light excitation.

References

[DB04]   M. Dimaki and P. Boggild. Dielectrophoresis of carbon nanotubes using microelectrodes: a numerical study. *Nanotechnology*, 15:1095–1102, 2004.

[LZML06] Lei Luo, Yanfeng Zhang, Samuel S. Mao, and Liwei Lin. Fabrication and characterization of ZnO nanowires based UV photodiodes. *Sensors and Actuators A*, 127:201–206, 2006.

Laser deposition of metals

Christian Pansow, Markus Trautmann, Veit Große, Frank Schmidl, Paul Seidel

I. Introduction

We use pulsed-laser deposition (PLD) to grow thin films of niobium and cobalt. The source of energy in our deposition systems is a Lambda Physics LPX3051 KrF excimer laser with a wavelength of 248 nm which can produce short pulses ($\tau = 25$ ns) with a pulse energy of 250…1200 mJ and a repetition rate up to 50 s^{-1}. The laser beam is focused on the target when entering into the vacuum chamber.

II. Deposition of niobium thin films

For serious studies on carbon nanotubes (CNTs) it is essential to perform electrical characterizations. Because of the high temperature while processing the CNTs it is important to use refractory metals as contacts. So far there are no physicals on niobium as contact material grown on silicon. Therefore it is interesting to investigate the pulsed-laser deposition of this metal.

We investigated the influence of different laser energies and target treatment to ensure a high film quality particularly to generate a good conductivity and a low droplet density.

A major problem in PLD of niobium is the low metal removal from the target. To get a higher deposition rate actually it is possible to raise the laser energy, the ablation time and the pulse frequency [1].
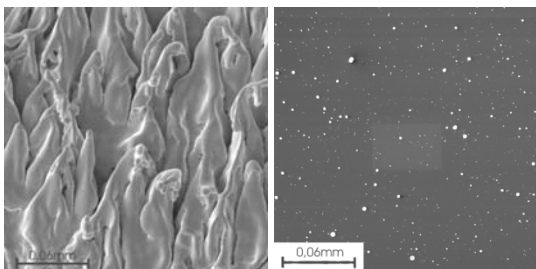
Fig. 1 - Melted cones of the target after 15 hours of deposition

Fig. 2 - Droplets on the substrate

Each alternative leads to a bigger target roughness (fig.1) followed by a higher droplet density (fig.2).

To remove the cones the target must be smoothed after four to five hours of deposition. Therefore the surface has to be lapped with Al_2O_3 and polished with SiO_2 (fig.3). After this treatment the droplet intensity strongly decreases (fig.4).
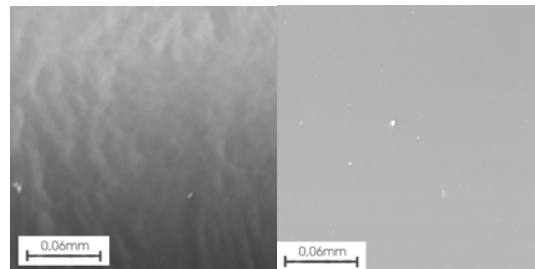
Fig. 3 - Smooth target surface after lapping and polishing

Fig. 4 - Decreased droplet intensity after lapping and polishing the target

III. Deposition of cobalt thin films

Besides iron and nickel (and different iron and nickel compounds) cobalt is a catalyst material used in synthesis of carbon nanotubes.

Using pulsed-laser deposition we want to produce thin cobalt films (thickness < 3 nm) on Si substrates [2] coated with an 100 nm thick SiO_2 layer grown by sputtering technique. The deposition rate in a PLD regime is a function of different parameters as energy density, deposition geometry and substrate temperature during deposition. Typical parameters of our deposition process are shown in table 1.

energy density (target)	4,9 J/cm^2
distance target - substrate	5 cm
deposition rate	0,24 nm/min

Table 1 – PLD parameters for the growth of cobalt films on Si substrate at room temperature

Deposition on cold substrates (room temperature) leads to very plane surfaces of the cobalt films. Using atomic force microscopy (AFM), a RMS roughness of 0,2 nm for an about 145 nm thick cobalt layer could be measured.

The way to produce very thin cobalt layers is to determine the deposition rate very exactly by analyzing films with about 100 nm thickness and to extrapolate the results on films with a thickness of 3 nm and less.

Using the catalytic layers, CNTs can be grown by chemical vapor deposition (CCVD) [3, 4]. We want to study the formation of clusters during annealing in the CCVD process. Therefore the cobalt layers can be heated to about 800 °C in the PLD system under vacuum conditions so few oxidation is assured. We expect a dependence of the cluster size on the thickness and the temperature and duration of annealing [5]. There should also be a dependence on the deposition rate which we can investigate by heating during the deposition. The size of the catalyst clusters is a very important parameter because the properties of the CNTs depend on it.

IV. Analytical methods

To characterize the thin metal films different methods are used.

For the determination of the film thickness we use the profilometer *Dektak 3030ST* (fig. 5) and atomic force microscopy (AFM). Therefore the layers must be structured by photo lithography or ion beam etching (IBE).

Another method for thickness measurement is X-ray reflection (XRR) [6]. To analyze the surface of the metal layers we use AFM and scanning electron microscopy (SEM). The chemical composition of the metal films can be proved by auger electron spectroscopy (AES) and X-ray photoelectron spectroscopy (XPS).

Furthermore the analysis of electrical properties is very important for the characterization of the niobium films which should be used as contact layers.

V. References

[1] D. B. Chrisey, G. K. Hubler (ed.), *Pulsed laser deposition of thin films*, Wiley & Sons, 1994

[2] M. Löffler, J. Cordón, M. Weinelt, J. E. Ortega, T. Fauster, Appl. Phys. A **81**, 1651 – 1655 (2005)

[3] B. Schröter, T. Reichelt, H. Rudolph, W. Richter, *Directed growth of carbon nanotubes on solid surfaces*, Annual Report, 2005

[4] L. Huang, B. White, M. Y. Sfeir, M. Huang, H. X. Huang, S. Wind, J. Hone, S. O'Brien, J. Phys. Chem. B **110**, 11103 – 11109 (2006)

[5] K. K. Nanda, S. N. Sahu, S. N. Behera, Phys. Rev. A **66**, 013208 (2002)

[6] M. Mildner, *Komplexe Röntgen-diffraktometrie an Dünnschichtsystemen*, Diss., TU Chemnitz, 2005

Fig. 5 - (a) Schematic of the stylus method, (b) the used structured substrate and (c) measurement result for a 60 nm thick cobalt film.

Current Transport and Ferroelectric Transition in Epitaxial Grown Strontium Titanate Thin Films

V Grosse, F Schmidl and P Seidel

Multinary oxides show a wide range of electrical properties depending on doping, intrinsic stress or external fields. Strontium titanate ($SrTiO_3$) is considered as a prototype for this class of materials. Depending on the defect structure the electrical conductivity can be varied between p-type and n-type semiconducting to metallic conductivity [1]. Like many other perovskites it shows bistable resistive switching by application of electric fields [2]. Single crystalline $SrTiO_3$ bulk material is further on known to remain paraelectric down to temperatures in the range of 0.035 K [3]. However, recently the ferroelectric phase transition in thin $SrTiO_3$ has been reported [4]. This phase transition can also be induced by electric fields [5].

This work is focused on the analysis of the electric properties of epitaxially grown $SrTiO_3$ thin films in the temperature range between 4.2 and 300 K. After a short introduction in sample preparation we summarize our results on the current transport properties for different film thicknesses. The main part concentrates on the dielectric behavior of these films at low temperatures. We discuss a theoretical model that describes this behavior as a ferroelectric transition induced by intrinsic electric fields.
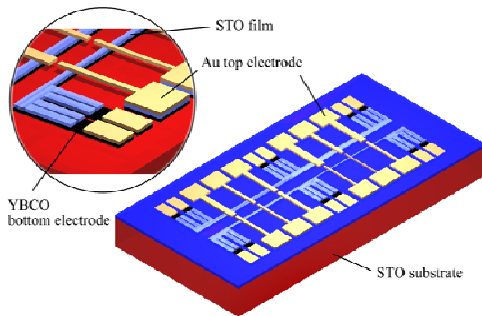
Figure 1: 3D model of the structure used for the electrical measurements of our samples.

Our $SrTiO_3$ films were analyzed in a capacitor like structure shown in figure 1. First we grow a trilayer of $YBa_2Cu_3O_{7-x}$ (YBCO, bottom electrode), $SrTiO_3$ and gold (top electrode)

epitaxially by pulsed laser deposition on single crystalline $SrTiO_3$ substrates. This trilayer was patterned utilizing Ar ion beam etching to form the bottom electrode and its bond pads. After the planarization with SiO_2 the top electrode was deposited by DC sputtering perpendicular to the bottom electrode.
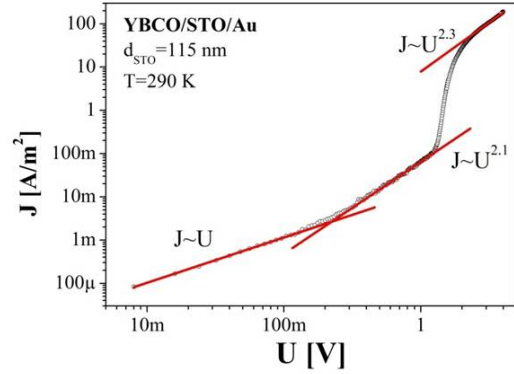
Figure 2: Typical I-V characteristic of the system YBCO/$SrTiO_3$/Au. For low voltages the conduction is ohmic. For higher voltages it changes to the square law typical for SCLC with traps in the insulator. Between 1 and 2 V the trap-filled limit is reached. The current rises dramatically such that the I-V characteristic obeys the trap-free square law.

From the analysis of the I-V characteristics we determined the dominant current transport mechanism in our samples. For films with thicknesses below 30 nm the leakage current is limited by an inelastic hopping process via localized states, namely variable range hopping. For higher temperatures this behavior changes to space charge limited conduction (SCLC). The samples with thicknesses above 30 nm show SCLC at all temperatures. A typical I-V characteristic is shown in figure 2. Additionally, one sample showed bistable resistive switching at room temperature and below. In the conductive state the sample showed metallic conductivity while the current transport in the resistive state was space charge limited. The origin of this behavior is discussed in detail by Szot et al.[2] and can be summarized as electrochemical

reduction and reoxidation of dislocations in the crystal.

To investigate the dielectric properties of SrTiO$_3$ thin films we measured the capacitance of our samples with different contact areas A in the temperature range from 4.2 K to 300 K. We used the Keithley 3330 LCZ-meter at a frequency of 5000 Hz and a signal level of 50 mV. From the evaluation of the formula $C = \varepsilon_0 \varepsilon_r {}^A\!/_d$ for the parallel plate capacitor (d is the SrTiO$_3$ film thickness) we determined the dielectric permittivity ε_r in this temperature range. With that approach we were able to eliminate the effect of offset capacitances due to stray fields in the substrate. The results are shown in figure 3.
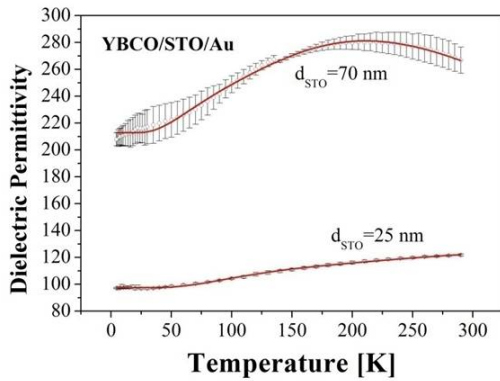
Figure 3: Temperature dependence of the dielectric permittivity of SrTiO$_3$ films with thicknesses of 25 and 70 nm. The red lines represent the fits of the measured data according to the model described in the text.

To fit the temperature dependence of the dielectric permittivity we used the model given by Hemberger et al.[5]. This model well describes an effect found in SrTiO$_3$ single crystals which they call electric field induced ferroelectric phase transition. This effect is characterized by a drop of the dielectric permittivity below a certain temperature in the presence of an electric field. This behavior we also observe for our samples (see figure 3). In our case the origin for the electric field is the difference in the work functions Φ of the electrodes which can be estimated to 1.2 eV (see figure 4). This results in an internal electric field of $E = \Phi / ed$.
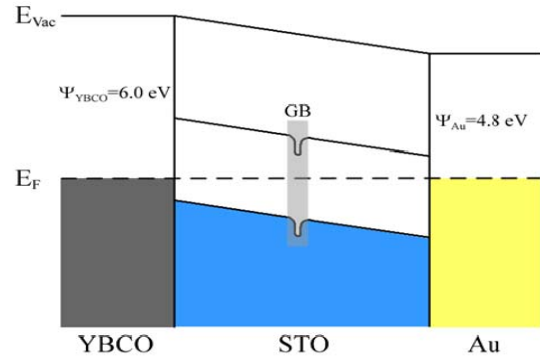
Figure 4: Energy diagram of the YBCO/SrTiO$_3$/Au system. The difference in work function of the electrode materials leads to a band bending in SrTiO$_3$ which results in an internal electric field. Grain Boundaries (GB) cause an additional band bendings.

To explain the relatively small values of ε_r we have to consider grain boundaries and dead layers at the interface SrTiO$_3$/electrode. Therefore, we calculated the effective dielectric permittivity using a brick wall model. The resulting curves are plotted as red lines in figure 3. Despite the good agreement between theory and experiment the influence of internal stress due to lattice mismatch, depolarization fields or grain boundaries is still unclear. A better knowledge about these effects would help to improve the model to better describe especially the behavior very thin SrTiO$_3$ films.

References

[1] C. Ohly, S. Hoffmann-Eifert, X. Guo, J. Schubert, R. Waser, J. Am. Ceram. Soc. **89**, 2845 (2006).

[2] K. Szot, W. Speier, G. Bihlmayer, R. Waser, Nature Materials **5**, 312 (2006).

[3] K. A. Muller, H. Burkhard, Phys. Rev. B **19**, 3593 (1979).

[4] J. H. Haeni et al., Nature **430**, 758 (2004).

[5] J. Hemberger, P. Lunkenheimer, R. Viana, R. Bohmer, A. Loidl, Phys. Rev. B **52**, 13159 (1995).

Long-time stable HTSC DC-SQUID gradiometers with silicon dioxide passivation

C Becker, A Steppke, M Buettner, H Schneidewind[*], V Grosse, F Schmidl and P Seidel

[*] Institut für Photonische Technologien (IPHT) e.V., Albert-Einstein-Straße 9,
D-07745 Jena, Germany

Introduction

Long-term sensor stability is a requirement for the application of high temperature superconducting DC-SQUID gradiometers. Changes in the electrical characteristics of sensors lead to decreased performance and a higher cost of the final system. The most sensitive areas of the gradiometer are the Josephson junctions, which we create using a single layer bicrystal technology [1]. A possible cause for degradation of superconducting thin films is the diffusion of oxygen in the YBCO layer. In monocrystalline films the oxygen transport occurs along the a-b plane of the crystals [2]. At growth defects or grain boundaries a significant oxygen diffusion appears along the c-axis of the epitaxially grown film [3,4]. Therefore a passivation at the sides and on top of the superconducting thin film is necessary to reduce diffusion. We developed a process to compensate for height differences during fabrication and protect our sensors using different materials to achieve stability over a period of more than one year.
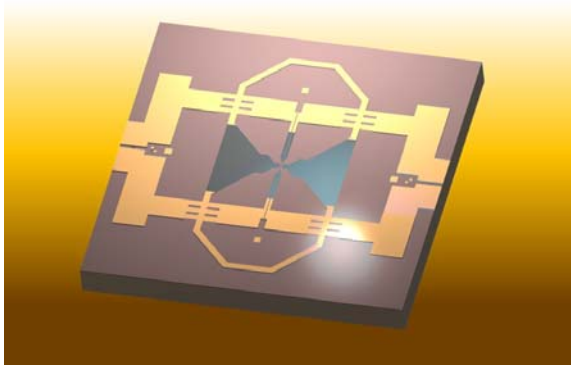
Fig. 1 Schematic of the planar DC-SQUID gradiometer.

Fabrication

The sensors described here are galvanically coupled DC-SQUID gradiometers (for layout see figure 1). The YBCO thin films having a thickness of 150 nm are grown along the c-axis on $SrTiO_3$ bicrystal substrates with pulsed laser deposition [5]. The thin films are patterned with Ar-ion beam etching and planarized *in situ* via the deposition of 150 nm amorphous YBCO with RF-sputtering. For repeated measurements

with different combinations of readout gradiometers and flux transformers the sensors need to be protected against mechanical damage and require high-quality bond contacts.

The direct contact between readout gradiometer and flux transformer in the flip-chip package can lead to damages in the thin films which influence the electrical properties of the system. A protective layer is also necessary to reduce diffusion of oxygen and to avoid contact between the superconducting thin film and environmental humidity. In our current setup we use SiO_2 for this layer on the top of the YBCO film [6].
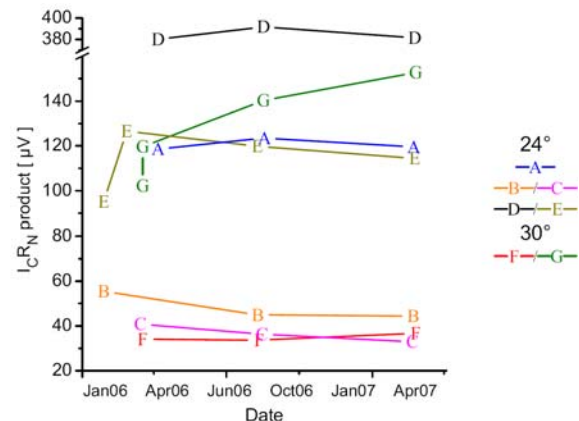
Fig. 2 Time dependence of the critical current and the normal state resistance of seven readout gradiometers with grain boundary angles of 24° and 30°.

Measurement

The sensors were evaluated over a period of one year in a magnetically shielded environment (two layers of μ-metal) to reduce the influence of external disturbances. During this period each sensor was cooled (77,4 K) and then heated to room temperature ten times to simulate environmental stress during the normal sensor lifetime. Between the measurements the gradiometers and flux transformers were stored at room temperature with a humidity of 40-45%.

To measure their *I-V* characteristics, the DC-SQUID gradiometers were biased with different currents and the resulting voltage signal was amplified and recorded. With this information
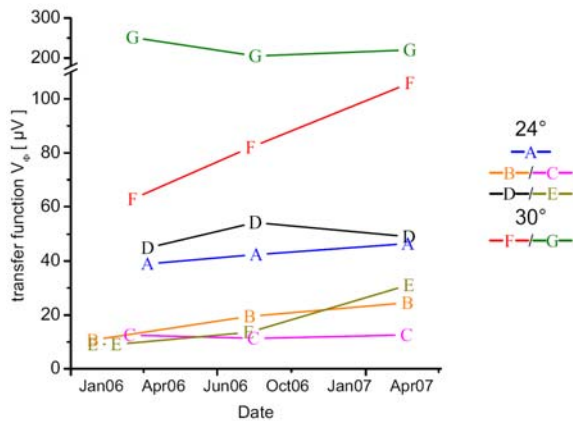
Fig. 3 Time dependence of the transfer function of the readout gradiometers in figure 2.

we calculated the critical current I_C, normal state resistance R_N and the $I_C R_N$ product (see figure 2). The $I_C R_N$ product allows to compare different types of Josephson junctions independent of the junction geometry. This parameter should change significantly if degradation between the measurements occurs. To evaluate the response to external magnetic fields we calculated the transfer function of the sensors over time (see figure 3). At a fixed bias current the maximum voltage modulation V_{pp} is measured as a function of the current in a small copper coil I_M. Assuming a sinusodial $V(I_M)$ characteristic the transfer function V_ϕ can be calculated as $V_\phi = \pi \cdot V_{pp}$.

Results

As a first step we examined whether there is a negative influence of the passivation on the superconducting properties of the sensors. With all tested sensors the SiO_2 thin film did not change the electrical characteristics and the dielectric influence is negligible compared to the influence of the substrate material ($SrTiO_3$).

The planarisation of the structures with amorphous YBCO deposited by hollow cathode sputtering does not lead to a large change of the superconducting properties of bicrystal Josephson junctions. In some cases we observed a slight increase of the critical current, compared to bicrystal junctions without planarisation. This can be caused by oxygen diffusion between the planarisation layer consisting of $YBCO_{7-x}$ with $x \approx 0$ and the crystalline thin film with $0.1 > x > 0$. An increase of the critical current is primarily observed for bicrystal angles of 30° and above.

During the the processing of the gradiometer, especially during the dry etching and photolithography steps a temperature increase of the thin film up to 100°C accelerates the diffusion of oxygen into the area of the Josephson junctions instead of out of this area as observed

without amorphous YBCO planarisation thin films. To lower the rate of diffusion out of the antenna areas the substrate is cooled by liquid nitrogen during the dry etching procedure [7,8]. The comparison among gradiometers (see figure 2) shows a large spread of the $I_C R_N$ product due to different current densities of the grain boundary junctions used for these experiments. All of these junctions show the typical scaling behaviour for grain boundary junctions [9]. Compared to previous experiments by other groups only the $I_C R_N$ value of 30 μm for the 30° grain boundary junction (curve F) is relatively low [10]. The experimental investigations of the long term stability shows no relevant changes or signs of degradation in most cases (see figure 2). Only small changes of the $I_C R_N$ product were measured. In all of these cases the reason for this behaviour was a decrease of the respective critical current.

The fabricated gradiometers display a large spread in the transfer function with a minimum of 10 μV. However, all sensors were able to operate in unshielded environment with commercially available SQUID electronics (e.g. Magnicon, Philips).

Summary

The developed and fabricated sensors were successfully protected by a combination of an amorphous YBCO and SiO_2 layers against oxygen diffusion. After a period of one year no significant signs of degradation were detected.

References:
[1] Gross R 2005 Physica C 432 105–115
[2] Aarnink W A M, Ijsselsteijn R P J, Gao J, van Silfhout A and Rogalla H 1992 Phys. Rev. B 45 13002–13007
[3] Kittelberger S, Bolz U, Huebener R P, Holzapfel B and Mex L 1998 Physica C 302 93–101
[4] Tian Y J, Linzen S, Schmidl F, Matthes A, Schneidewind H and Seidel P 1999 Thin Solid Films 338 224–230
[5] Seidel P, Schmidl F, Wald H, Mans M, Peiselt K, Baldeweg U, Beck M, Biering S, Becker C, Uhlig J and Grosse V 2005 IEEE Trans. Appl. Supercond. 15 161–164
[6] Seidel P, Becker C, Steppke A, Foerster T, Wunderlich S, Grosse V, Pietzcker R and Schmidl F 2007 Physica C 460 331-334
[7] Schneidewind H, Schmidl F, Linzen S and Seidel P 1995 Physica C 250 191–201
[8] Alff L, Fischer G M, Gross R, Kober F, Beck A, Husemann K D, Nissel T, Schmidl F and Burckhardt C 1992 Physica C 200 277–286
[9] Seidel P, Foerster T, Schneidewind H, Becker C, Grosse V, Steppke A, Lorenz P, Pietzcker R and Schmidl F 2007 IEEE Trans. Appl. Supercond. Vol. 17 No.2 668
[10] Minotani T, Kawakami S, Kiss T, Kuroki Y and Enpuku K 1997 Jpn. J. Appl. Phys. 36 L1092–L1095

High-T$_c$ superconducting quantum interference device gradiometer for a two-dimensional magnetic field gradient measurement

A. Steppke, C. Becker, V. Grosse, L. Dörrer,
F. Schmidl, M. Djupmyr[*], J. Albrecht[*] and P. Seidel
[*]Max-Planck-Institut für Metallforschung, Heisenbergstr. 3, D-70569 Stuttgart, Germany

We present a planar SQUID structure consisting of four SQUIDs connected to antenna structures for simultaneous measurements of two magnetic field components. Using YBa$_2$Cu$_3$O$_{7-x}$ thin film technology we are able to prepare gradiometer structures on strontium titanate (SrTiO$_3$) tetracrystals containing two crossing 30° grain boundaries. This allows the production of four SQUID loops onto one substrate which can fulfill the high demands of symmetry inside the antenna structures. In our ar-
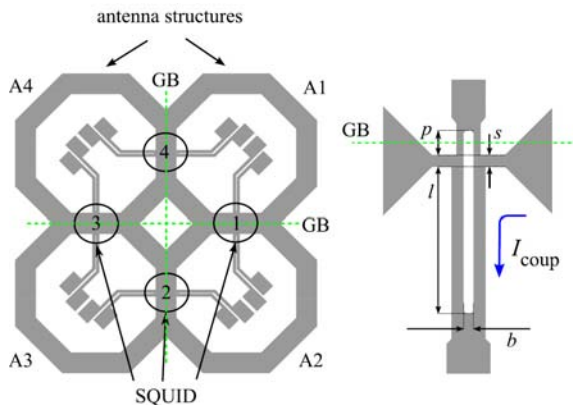
Fig. 1 Left side: Layout of the antenna structures with four superconducting loops coupled together to create four gradiometers; right side: The DC SQUID layout in U-shape with incoupling current I$_{coup}$ and the grain boundary (GB).

rangement the SQUID loops can act as independent field sensors which allow a measurement of two independent magnetic field gradient components with high accuracy.

Using our previous parallel DC SQUID gradiometer layout [1] as a starting point, the design goal was to create at least two orthogonal gradiometers on one substrate. If two unconnected gradiometers are placed on the crossed bicrystalline substrate, the individual antenna area has to be significantly reduced compared to the original layout. As a smaller antenna area corresponds to a lower field gradient resolution, this approach lowers the sensitivity com-

pared to the single gradiometer. This disadvantage can be avoided by combining the two antenna structures into a single common area (see figure 1). Each antenna structure A1-A4 is part of two gradiometers. The DC SQUIDs within the gradiometers are therefore all galvanically coupled to each other via the antennas.

To test the influence of different bias currents for the individual DC SQUIDs and the response to an external field gradient, we
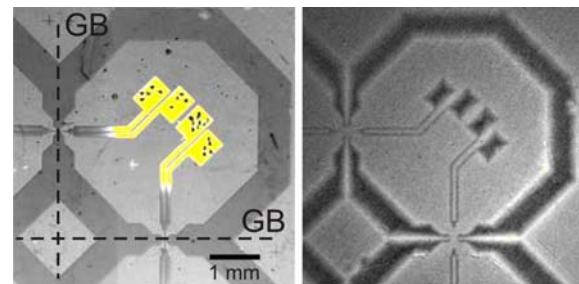
Fig. 2 Optical (left) and magneto-optical (right) image of antenna loop A1. The magneto-optical image was made at T = 77 K in an external magnetic field. Bright colors indicate high magnetic flux densities.

simulated the four gradiometers in PSCAN [2]. Parameters for the simulation were taken from previous measurements of the SQUID inductance.

The quality of the prepared structures has been investigated by magneto-optical imaging. With this technique, the penetration of magnetic flux into superconducting structures can be visualized and the corresponding critical current density can be accessed with a spatial resolution of a few micrometers [3]. The right image of figure 2 shows a magneto-optical image of antenna loop A1 at a temperature of T = 77 K, obtained after zero-field cooling in an external magnetic field of B = 1.5 mT. Bright contrast indicates a high magnetic flux density. The homogeneous black contrast proves a constant high critical current density along the antennas at T = 77 K.

The four DC SQUIDs of our first sensor exhibit critical currents in the range of

22 µA to 52 µA, which corresponds to an average I_cR_n-product of 193 µV. The voltage modulation ΔU_{pp} lies between 7 and 38 µV which allows stable operation with flux-locked-loop SQUID electronics [1]. In our first design we focused on stability in unshielded environments; however, a previous gradiometer layout has shown that tuning the inductance parameter β_L can improve sensitivity [4]. The effective area A_{eff} was measured by moving the sensor in a known
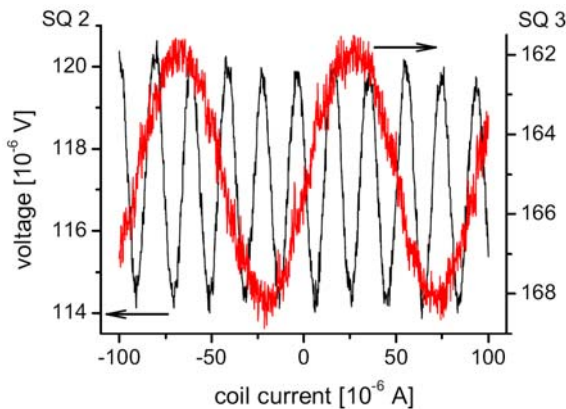
Fig. 3 Measured voltage signal from SQUID 2 and SQUID 3 in response to an applied magnetic field gradient via an induction coil under antenna A2.

magnetic field configuration and recording the SQUID response. The resulting area is 0.141 mm^2 for a single gradiometer. With a similar setup, we measured the performance in a homogeneous magnetic field to determine the balance of the sensor. The first approximation with this setup shows a balance better than 60 for the gradiometer. Further improvements can be achieved by using two SQUIDs in a gradiometric configuration[4].

In figure 3 the response to an external magnetic field gradient is shown. SQUID 2 and 3 are biased individually and the external field gradient is applied using an copper coil under antenna A2. The resulting voltage modulation of the two SQUIDs shows that the sensor can measure two field components simultaneously.

In summary, we designed and tested a new type of thin film gradiometer in a single layer high-T_c technology that is able to concurrently measure first-order field gradients dB_z/dx and dB_z/dy. Simulations showed that all four SQUIDs could operate independently and that the orthogonal gradiometers are sensitive to the direction of the applied magnetic field gradients. Magneto-optical imaging of the sensor's antenna structures showed a low flux penetration in an external field of 1.5 mT, emphasizing the high quality of the thin film. The measurement results of the sensor showed a high I_cR_n-product, underlining that Josephson junctions with a grain boundary of 30° can be used for low noise applications. The sensitivity of this two-dimensional gradiometer can be optimized based on design principles from standard gradiometers. In future work, we will investigate the possibility of signal processing to additionally measure the second-order gradient without changes to the sensor.

References:
[1] P. Seidel, C. Becker, A. Steppke, T. Foerster, S. Wunderlich, V. Grosse, R. Pietzcker, and F. Schmidl, Physica C 460, 331 (2007).
[2] S. V. Polonsky, P. Shevchenko, A. Kirichenko, D. Zinoviev, and A. Rylyakov, IEEE Trans. Appl. Supercon. 7, 2685 (1997).
[3] C. Jooss, J. Albrecht, H. Kuhn, S. Leonhardt, and H. Kronmüller, Rep. Prog. Phys. 65, 651 (2002).
[4] S. Wunderlich, L. Redlich, F. Schmidl, L. Dorrer, T. Köhler, and P. Seidel, Physica C 340, 51 (2000).
[4] P. Seidel, F. Schrey, L. Dorrer, K. Peiselt, F. Schmidl, F. Schmidt, and C. Steigmeier, Supercond. Sci.
Technol. 15, 150 (2002).

TMRX measurements on magnetosomes

M. Büttner, S .Prass, M. Röder*, C. Lang**, P. Görnert*, D. Schüler**
and P. Seidel

*Innovent Technologieentwicklung, Prüssingstraße 27B, 07745 Jena
**LMU München, Bereich Mikrobiologie, Maria-Ward-Str. 1a, 80638 München

Magnetosomes [1] (defined nano-particle mono-crystal systems) are produced by magnetotactic bacteria and serve the cells as guidance assistance in magnetic fields (magnetotaxis). Temperature dependent magnetorelaxtion measurements (TMRX) provide information about the magnetic behaviour of magnetic nanoparticles [2].

We used the temperature dependent magnetorelaxation method to analyse magnetic nanoparticles isolated from *Magnetospirillum gryphiswaldense* wild type and mutant which produces magnetosomes of a slightly reduced size. A picture of the magnetosomes is shown in figure 1.
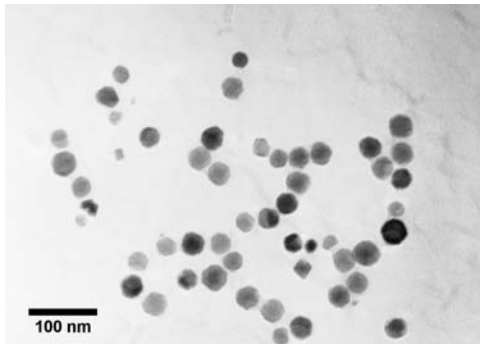
Figure 1: Transmission electron micrograph (TEM) of the magnetosomes produced by *M. gryphiswaldense.*

Figure 2 shows the measured energy barrier distribution as a function of temperature in the range from 4 K to 320 K. In both samples we find relaxation signals in the range of 4 K to 75 K and additionally at 96 K (modified) and 106 K (wild type). The Nèel relaxation appears only at temperatures above 300 K as an increase in the measured signal.

We interpret this as the lower end of the energy barrier distribution expected for particles with a diameter in the range of the magnetosomes.
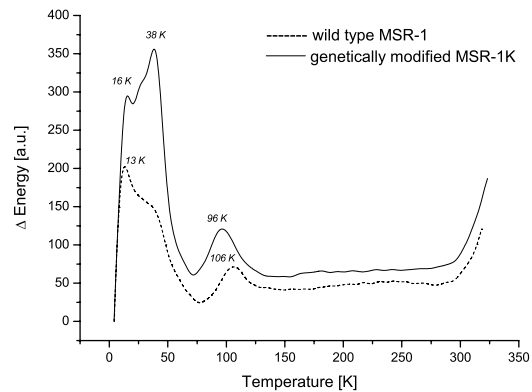
Figure 2: Energy barrier distribution of the wild type and modified bacterium in the temperature range from 4 K to 320 K.

At temperatures lower than 300 K other (than Nèel) relaxation processes are highly probable. We base our assumption that at temperatures around 100 K a Verwey transition [3] is taking place on the known effects in bulk material. The exact transition temperature is dependent on the oxygen stoichiometry. The two peaks in the measured relaxation signal at 106 K (wild type) and 96 K (modified type) can be the result of a Verwey transition. The magnetite changes its conductivity from metallic to insulating below a certain temperature, which depends on the magnetite properties. This transition is characterised by changing the crystal structure from cubic to monoclinic. The difference in transition temperature between the modified and wild type samples are evidence for structural differences of the samples. Since the Fe_3O_4 oxidation state is unstable we observed the evolution of the energy barrier distribution in repeated measurements over the course of 120 days. During this time the Verwey peaks diminished continuously and finally disappeared (fgure 3). We explain this behaviour with an oxidation of the particles from Fe_3O_4 to $\gamma\text{-}Fe_2O_3$, which does not

show a Verwey transition. This disappearance supports the hypothesis of a Verwey transition.
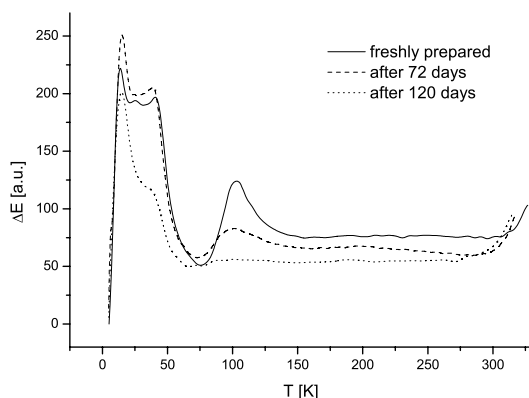
Figure 3: Disappearance of the Verwey transition over a course of 120 days due to oxidation of Fe_3O_4 to γ-Fe_2O_3.

A possible explanation for the peaks at lower temperatures between 13 K and 38 K including the substructures could be the special electronic structure of magnetite. Kronmüller and Walz [4] reported magnetic after effects in Fe_3O_4 and vacancy doped magnetite in the temperature range of 4 K to 130 K. It is yet unclear if the observed structures are related to intrinsic processes within the particle or to the interaction between a number of nearby particles.

This is the first evidence for a Verwey transition and the effect of the electronic structure on the relaxation signal of magnetic nanoparticles.

References

[1] D. Schuler 2002 Int. Microbiol 5 209-14.
[2] E. Romanus, T. Koettig, G. Glöckl, S. Prass, F. Schmidl, J. Heinrich, M. Gopinadhan, D.V. Berkov, C. Helm, W. Weitschies, P. Weber, P. Seidel 2007 Nanotechnology 18 115709.
[3] E. J. W. Verwey 1939 Nature 144 327-8.
[4] H. Kronmuller and F. Walz 1980 Philos. Mag. B 42 433-52.

Low mechanical loss materials studied by Cryogenic Resonant Acoustic spectroscopy of bulk materials (CRA spectroscopy)

A. *Schroeter, R. Nawrodt, D. Heinert, C. Schwarz, W. Vodel, A. Tünnermann*[*] *and P. Seidel*
[*]Institut für Angewandte Physik, A.-Einstein-Str.15, 07745 Jena

Low mechanical loss materials are required to decrease thermal noise in instruments with extraordinary precision like gravitational wave detectors since mechanical losses and thermal noise are related [1]. Candidate materials for substrates of optical components of future cryogenic interferometric gravitational wave detectors are crystalline silicon, sapphire, calcium fluoride, and quartz [2]. Due to the anisotropy of the crystals and the search for an optimal operating temperature of the detectors, systematic measurements of the mechanical losses have to be performed. Therefore, our novel mechanical spectroscopy method, cryogenic resonant acoustic spectroscopy of bulk materials (CRA spectrocopy), was applied in the temperature range from 5 K to 300 K. Instead of the small losses in the detection band, the reciprocals of the losses at the resonant frequencies, the mechanical quality factors Q, have been measured. Following the test of our method on the fairly well-known material crystalline quartz [3], results on silicon and calcium fluoride have been achieved [4]. For details on the measuring setup and method see refs. [5] and [6]. The reciprocals of the measured Q factors of two selected modes of a cylindrical crystalline silicon (100) sample (76.2 mm in diameter, 12 mm thick) have been plotted in Figs. 1 a) and b). They correspond to the mechanical losses at the particular resonant frequency and temperature. According to the superposition principle of low mechanical losses, the total damping curve has been decomposed into contributions (coloured lines in Figs. 1 and 2) caused by single anelastic processes of different origin. The loss ϕ related to a single relaxation process with small relaxation strength Δ at frequency f has been modelled by

$$\phi = \Delta \frac{2\pi f \tau}{1+\left(2\pi f \tau\right)^2}, \Delta = \Delta_0 d\left(\vartheta, f_r\right), \qquad (1)$$

where τ is the relaxation time, Δ_0 is a dimensionless coupling strength and $d\left(\vartheta, f_r\right)$ is in general a function of reduced (dimensionless) temperature ϑ and frequency f_r. The relaxation time was assumed to follow an Arrhenius-like law

$$\tau = \tau_0 \exp\left(E_a / \left(k_B T\right)\right), \qquad (2)$$

with relaxation constant τ_0, activation energy E_a, and Boltzmann constant k_B.

a)

b)
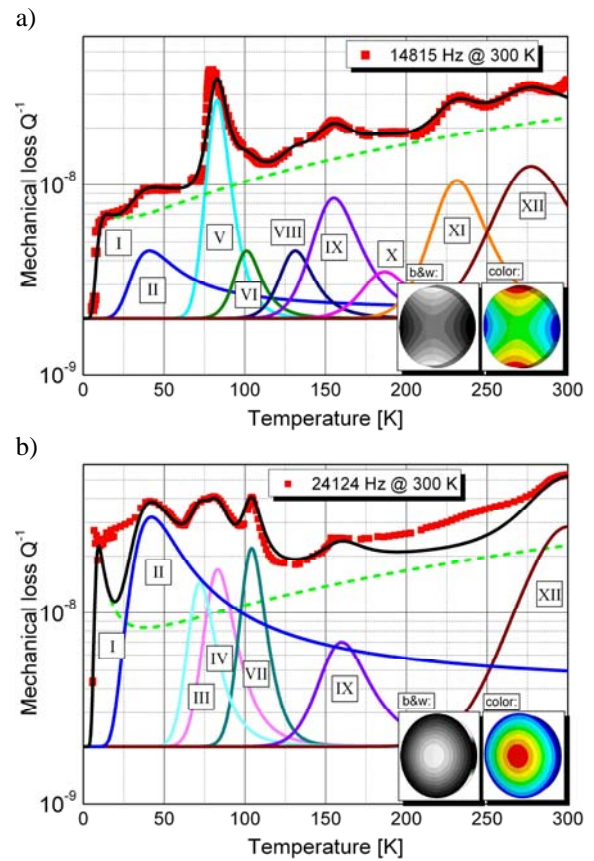
Figs. 1 a) and b) Loss vs. temperature gained by Q measurements on a silicon sample. Red squares: reciprocals of measured Q factors. For fit parameters see ref. [4]. The excited mode shape is shown as a contour plot of the displacement in direction of the cylinder axis. Red and blue denote max. displacement (in b&w: black and white), green minimum.

The mechanical losses are dominated over the whole temperature range by dissipation processes assigned to interactions of the acoustic waves with thermal phonons (peak

I) [4]. This 'phonon-peak' is well approximated by assuming Δ proportional to T. Several fit parameters of the remaining peaks have been related to formerly observed reorientation processes. For the fit parameters and the relaxation parameters, respectively, as well as the reference parameters see ref. [4]. The peak VI in Fig. 1 a) shows similar parameters to that assigned to vibrations of Si-O-Si complexes by IR measurements on oxygen-doped silicon. In the damping curves of both modes peak IX and XII might be due to an electronic redistribution and a defect reorientation of vacancy-oxygen (VO) complexes, respectively. A hydrogen atom jumping between two Si dangling bonds in vacancy-oxygen-hydrogen complexes (VOH and VOH2 defects) is probably the reason for peak VIII in Fig. 1 a). The silicon samples investigated in our experiments were grown by a Czochralski process. This method introduces a considerable amount of oxygen into the material (content of our samples: $7 \times 10^{17} / cm^3$). Since the VO as well as the VOH complex anneals out at 573 K, such a treatment might decrease the damping in the corresponding temperature regions. According to the attenuation measurements of Pomerantz [7] the sample is presumably doped with phosphorus (peak II). Regarding the relaxation strengths, the dependence on mode shape is especially visible in the low temperature region.

The variation of the mechanical losses in a sample made of CaF_2 (100) (cylindrical shape, 75 mm in diameter, 75 mm thick) is far less existent as for silicon (Fig. 3). Damping peaks with similar characteristic parameters appear in all damping curves. The results on one mode have been exemplarily plotted in Fig. 2 b). The losses in the low temperature range are dominated by thermoelastic damping (dotted line). Therefore, the 'phonon-peak' I is less visible. According to its progression at higher temperatures, the relaxation strength has been modelled to be proportional to T^2. For details see ref. [4].

A further interpretation of the damping peaks according to their characteristic parameters is in progress, as well as the application of selection rules for defect induced mechanical losses and investigations concerning the relation of mode shape and relaxation strength aided by group theory (cf. [8]).
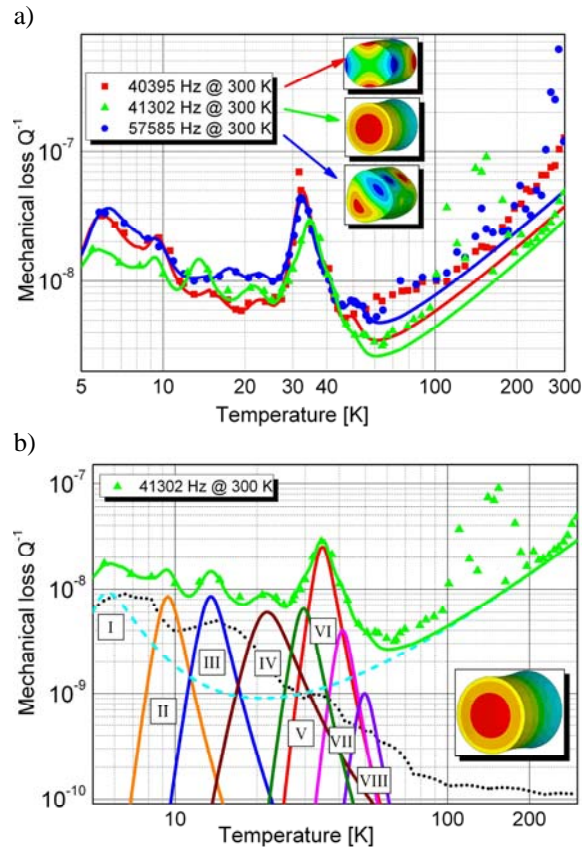
Figs. 2 a) and b) Losses gained from Q measurements on CaF_2 sample (details in text).

References

[1] H. B. Callen and T. A. Welton 1951 Phys. Rev. 83 34-40.
[2] S. Rowan et al. 2005 Phys. Lett. A 347 25-32
[3] A. Zimmer et al. 2007 Rev. Sci. Instrum. 78 pp. 063905-1 - 8.
[4] A Zimmer et al. 2007 J. Phys.: Conf. Ser. 92 012095 (4pp).
[5] R. Nawrodt et al. 2006 Cryogenics 46 718-23.
[6] D. Heinert et al. 2007 J. Phys.: Conf. Ser. 92 012183 (4pp).
[7] M. Pomerantz 1970 Phys. Rev. B 1 4029-36.
[8] A. Schroeter 2007 Mechanical losses in materials for future cryogenic gravitational wave detectors, thesis, FSU Jena.

Analysis of mechanical losses in crystalline quartz

D. Heinert, C. Schwarz, R. Nawrodt, A. Schroeter, W. Vodel,
A. Tünnermann* and P. Seidel
*Institut für Angewandte Physik, A.-Einstein-Str. 15, 07745 Jena

## Introduction

The direct detection of gravitational waves belongs to one of the most challenging tasks for nowadays experimental physics. There are mainly two concepts in use to detect them. On the one hand, the wave's influence on an optical path length is determined with an interferometer. On the other hand resonant mass set-ups are capable of registering an incident wave. Due to the weak effect of a gravitational wave onto the detectors' signals [1] the minimization of their noise is indispensable. The noise of a system is related to its losses via the fluctuation-dissipation-theorem [2]. That's why a low noise is connected with low losses of the system. The present work studies the Brownian noise caused by the substrates of an interferometer's optical components as it limits the sensitivity of the apparatus in the detection band. Therefore, the mechanical loss of crystalline quartz as a model material is under investigation concerning internal loss processes.

Experimental set up

In a special cryostat the Q-factor of two cylindrical samples with different crystal orientations have been measured in a temperature range from 5 K to 300 K. The samples were suspended as pendula and electrically excited to resonant vibrations. The free decay of these vibrations has been measured optically, leading to the Q-factor of the resonance. For further details see [3, 4].

The mechanical loss ϕ can be obtained as the reciprocal of the Q-factor

$$\phi(\omega) = \frac{1}{Q(\omega)}, \qquad (1)$$

where ω is the angular frequency of the excitation.

Theory

The model of the standard anelastic solid explains the behaviour of a non-ideal, lossy solid. It leads to an expression for the mechanical losses ϕ [5]

$$\phi = \Delta \frac{\omega\tau}{1+\omega^2\tau^2}. \qquad (2)$$

Within eq. (2) τ is called relaxation time and Δ relaxation strength, which is assumed to be athermal. The temperature dependence of ϕ arises from a further assumption - the double well potential. There, mainly thermal activation allows the crossing of the energy barrier E_a between two stable states. The mean time τ between jumps from one to another state is then given by an Arrhenius law

$$\tau = \tau_0 \exp\left(\frac{E_a}{kT}\right), \qquad (3)$$

with τ_0 as relaxation constant, k as Boltzmann constant and T as temperature. The given model applies especially well to point defects in a dynamic equilibrium between different positions. A net flow of particles to a new equilibrium occurs after a stress-induced deformation of the potential. This process is called relaxation.

Eqs. (2) and (3) allow the characterisation of a loss peak with three parameters: Δ, τ_0 and E_a.

Results

This characterisation was done for five different frequencies per sample. Eight different loss peaks could be fitted to the measured data of the two samples.

Examples for fit curves are shown in fig. 1. The given diagrams contain data belonging to one sample for different frequencies as well as the fits to the respective loss peaks. In the upper right corner the mode shape, which describes the macroscopic distortion of the substrate, is represented. The colors indicate the distortion perpendicular to the sample's surface, with red and blue areas moving and green areas resting.
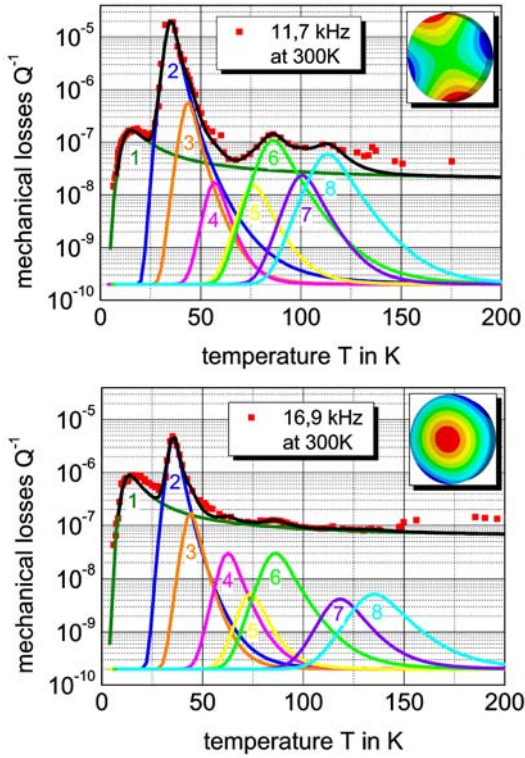
Fig. 1: Diagrams of the losses (red points) due to the Q-factor measurement over temperature for the z-cut sample ($\varnothing$ 76.2 mm × 12 mm). The black line represents the linear sum of the eight coloured single loss peaks fitted to the data.

There is a clear influence of the mode shape on the height of the loss peaks. The relaxation strengths of nearly all peaks decrease by a factor of 5 for changing to the mode with higher frequency. Only the first peak (dark green), which originates from phonon-phonon-interactions [6], shows a considerable increase. By contrast, the remaining peaks seem to belong to defects in the crystal [6]. A group theoretical treatment of the correlation between mode shape and relaxation strength in the case of defect induced losses is in progress. The influence of the crystal's orientation is negligible compared to mode shape effects. Tab. 1 supports this conclusion. Only the phonon induced losses are significantly l

frequency in kHz	Δ in 10^{-5}	E_a in meV	frequency in kHz	Δ in 10^{-5}	E_a in meV
38,4	4	55	11,7	4,4	58
54,0	2,0	51	16,9	0,98	61
62,4	0,8	55	61,4	2,5	62,5
70,9	1,2	51	123,8	1,9	50,5
95,9	1,6	50,5	321,0	2,7	58

Tab. 1: The table shows the determined values of Δ and E_a for the sample in x cut ($\varnothing$ 45 mm × 50 mm) on the left as well as for the z cut ($\varnothing$ 76.2 mm × 12 mm) on the right. All data belong to peak #2 (dark blue). Fraser [7] reports an energy of E_a=56,5 meV for the same peak, which fits well to our value.

lower for the x-cut sample. A possible explanation can be found in the different geometries of the substrates. So the x cut is more compact and thus phonons should experience fewer scatterings on the surface.

Summary

The reliability of our experimental method was proven by comparison with earlier, external measurements. Besides, the analysis of the mechanical loss data revealed two to our knowledge unpub-lished loss processes (3 and 7 in fig. 1).
Although crystalline quartz isn't a favourite candidate for a gravitational wave detector [8], it remains a perfect material for studying loss mechanisms in any case.

References

[1] R. Saulson 1994, World Scientific, *Fundamentals of gravitational wave detectors*

[2] H. B. Callen, T. A. Welton 1951, Phys. Rev. 83 pp. 34-40.

[3] R. Nawrodt et al. 2006, Cryogenics 46 pp. 718-23.

[4] D. Heinert et al. 2007, J. Phys. :Conf. Ser. 92 012183 (4 pages).

[5] C. Zener 1948, Chicago Press, *Elasticity and Anelasticity of Metals*

[6] A. Zimmer et al. 2007, Rev. Sci. Instrum. 78 pp. 063905- 1-8.

[7] D. B. Fraser 1968, Physical Acoustics Vol. 5 pp. 59-110.

[8] D. Heinert 2007, FSU Jena, diploma thesis *Mechanische Verluste in Festkörpern*

Cryogenic Q-factor measurements on silicon

C Schwarz, D Heinert, R Nawrodt, A Schroeter, R Neubert, M Thürk, W Vodel,
A Tünnermann*, P Seidel
*Institut für Angewandte Physik, A.-Einstein-Str.15, 07745 Jena

The direct detection of gravitational waves is one of the biggest challenges of mankind. To detect these weak signals enormous sensitive instruments like interferometers are developed and still under construction [1]. The sensitivity of these devices is limited by several noice sources. Within the detection band thermal noise of the detector components dominates the achievable sensitivity. To reduce the thermal noise on the one hand one can decrease the temperature of several parts of the detector down to cryogenic temperatures to reduce their thermal energy. On the other hand one can choose materials with higher mechanical Q-factors than the materials currently in use. Silicon as shown in figure 1 seems to be the most promising material in terms of this purpose.

Fig.1 - Two different samples with a diameter of 3" that are used to investigate the mechanical Q-factor.

One way to investigate the internal losses is to excite the test sample to resonant vibrations using a frequency modulated electric field of a comb-like structure [2] as shown in figure 2.
The suspension of the sample is realized by a 50 µm thick tungsten wire. So the wire is formed like a loop to suspend the sample as a pendulum to reduce seismic disturbances.
After reaching a certain amplitude of vibration the electric field is switched off and the free harmonic decay of the oscillating amplitude is recorded.
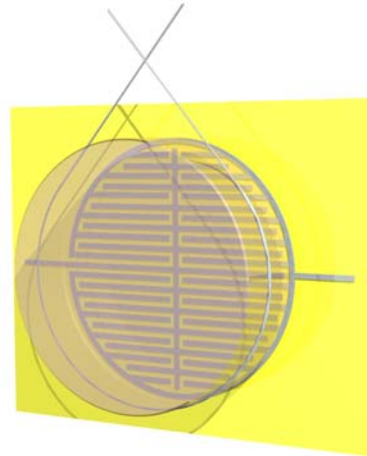
Fig.2 - Schematic view of a transparent test sample suspended by a tungsten wire and the excitation realised by a comb-like structure.

With the time τ that passes during the start-amplitude decay to 37 percent, one can calculate the mechanical loss using

$$Q = f\pi\tau \ .$$

To avoid additional damping like pressure damping the substrat is placed in a vacuum vessel which can be evacuated to a pressure lower than 10^{-3} Pa.
The whole experiment was carried out in cryostat which is temperature-stabilized between 5 and 300 K to investigate the temperature dependence of the mechanical Q-factor [3].
Figure 3 shows the Q-factor as the inverse of the losses between 5 and 300 K for three different modes (between 10 and 70 kHz). Each point represents one ring down measurement.
Between 300 and 100 K the characteristics of the Q-factor seems to be influenced by the suspension system which
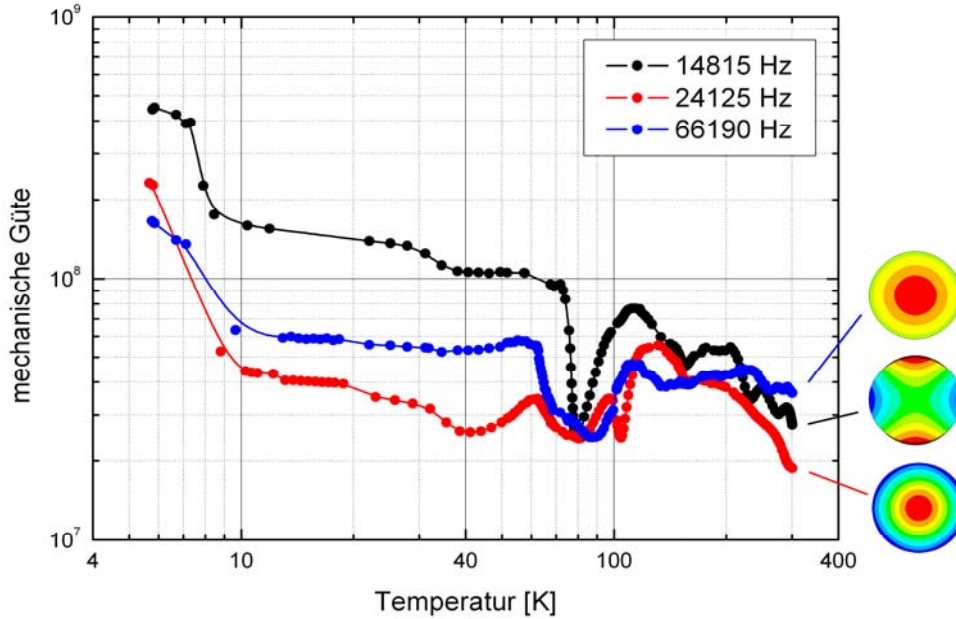
Fig.3 - Compilation of the cryogenic Q-factor measurements of three different modes between 10 kHz and 70 kHz. The Si (100) test sample's dimensions were $\varnothing$ 76.2 mm x 12 mm.

is not understood yet. Below 100 K some dips caused by relaxation pro-cesses appear.
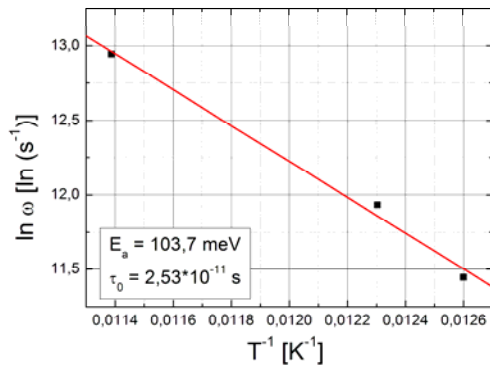
Fig.4 - Calculation of the activation energy E_a and the relaxation time τ^* using the arrhenius law.

Using $2\pi f\tau'=1$ and the Arrhenius law

$$\tau' = \tau^* e^{-\frac{E_a}{k_B T}}$$

an activation energy E_a and a relaxation time τ^* can be calculated to describe possible impurities [4]. Therefore $\ln\omega$ is plotted vs. T^{-1}. The slope of the linear fit includes the activation energy.

Below 60 K the Q-factor increases until every mode reaches its maximum Q-factor at a minimum temperature of 5.8 K. There the ring down time τ of the 14 kHz-mode lasted approximately 9700 s with a

resulting ϕ of about $2.2 \cdot 10^{-9}$. Overall the measurement at 5.8 K lasted 8 h, where a temperature stability of $\pm$ 0.1 K was reached.

The sample's Q-factor shows an improvement at temperatures below 80 K com-pared to the values at room-temperature. So silicon seems to be in principle suitable as material for components in future gravitational wave detectors.

References:

[1] V.B. Braginsky, In Quantum Physics and the Universe, 1992.
[2] A. Candez, A. Abramovici, J. Phys. E: Sci Instrum.21:453 – 456, 1988.
[3] R. Nawrodt, A. Zimmer, S. Nietzsche, M. Thürk, W. Vodel, P. Seidel, Cryogenics 46 (2006), 445 - 450.
[4] G.C. Lam, PhD thesis, The University of Rochester, 1979.

Mechanical Q-factor measurements of a test mass with a grating structure

R. Nawrodt, A. Schröter, W. Vodel, R. Schnabel[*], K. Danzmann[*], A. Tünnermann[**]
and P. Seidel

[*]Albert-Einstein-Institut, Callinstr. 38, 30167 Hannover
[**]Institut für Angewandte Physik, A.-Einstein-Str.15, 07745 Jena

Introduction

Current gravitational wave detectors are limited by different kinds of noise. One of the fundamental limits of future detectors will be the thermal noise of the test masses and their optical coatings.

Different approaches exist to overcome this limit. The most promising attempt is the use of cryogenic temperatures. In addition new interferometer topologies like grating interferometry [1] are used. Thus, it is necessary to investigate the influence of the grating structures to the thermal noise of the component at low temperatures.

Theory

Thermal noise is related to the internal mechanical losses of a system by means of the fluctuation-dissipation theorem [2]. Low mechanical loss materials obey low thermal noise within the detection band of a gravitational wave detector. The mechanical losses of a material arise from different internal processes. Among them scattering processes of phonons at the surface of the substrate play an important role. Thus, any disturbance – especially a grating etched to the surface – needs to be investigated at low temperatures.

As a measure for mechanical losses ϕ the mechanical Q-factor was used. These two properties are related in the case of structural damping by means of:

$$Q(\omega) = \frac{1}{\phi(\omega)} .\qquad(1)$$

If a combined system consisting of two different materials is used the over-all Q-factor is calculated using:

$$\frac{1}{Q_{total}} = \frac{1}{Q_{substrate}} + \frac{E_{layer}}{E_{substrate}}\phi_{layer},\qquad(2)$$

where $Q_{substrate}$ is the Q-factor of the substrate without any treatment and ϕ_{layer} is the mechanical loss of the layer applied to the surface of the substrate. $E_{layer}/E_{substrate}$ is the ratio of the vibration energies stored in the surface layer and the bulk substrate. This value can be calculated using a finite element analysis, e.g. with the software ANSYS.

Experimental Setup

The measurement of the mechanical Q-factor was done using a ring down technique [3]. The substrate is excited to resonant vibrations by means of an alternating electrical field. After having reached a sufficient high amplitude the exciter is switched off and the subsequent ring-down is recorded. The mechanical Q-factor is calculated from the resonant frequency f_0 and the characteristic ring-down time τ:

$$Q = \pi f_0 \tau .\qquad(3)$$

The setup is placed in a special built cryostat [4] to obtain temperature dependent values.

Sample Preparation

Crystalline quartz was used as substrate material. The sample was measured at different stages of the fabrication of the optical grating within a temperature range from 5 to 300 K:

1) without any surface treatment,

2) with a grating (1 µm period, 100 nm depth) etched into the surface,

3) with a 200 nm thick silica (SiO_2) layer applied to the grating,

4) with a high reflecting (HR) stack made from alternating silica (SiO_2)/tantala (Ta_2O_5) layers.

Results

Fig. 1 represents the measured Q-factors for the different fabrication steps.
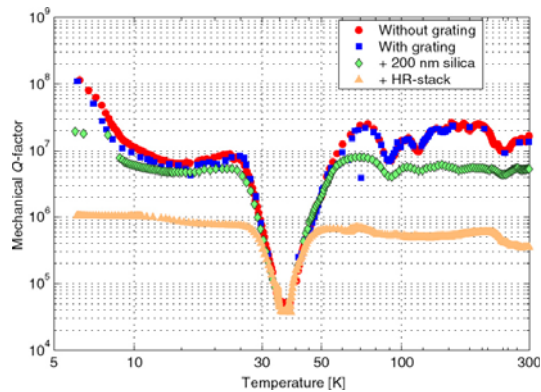
Fig. 1: Measured values of the mechanical Q-factor for different fabrication steps of an optical grating applied to a crystalline quartz sample ($\varnothing$ 76.2 mm × 12 mm, c-cut). Measuring frequency: 11.7 kHz.

The curve measured without any surface treatment shows different dips at certain temperatures. These dips could be correlated with internal loss mechanisms (e.g. interaction with impurities, phonon-phonon-interaction, see [5]). By applying an optical grating to the surface no change of the mechanical Q-factor could be observed within the measuring errors. If a dielectric layer is deposited to the surface the Q-factor decreases. Using eq. (2) it is possible to extract the mechanical loss of the grating and the dielectric layers. The calculated energy ratios between the layer and substrate can be found elsewhere [6]. Fig. 2 shows the mechanical losses of the different layers multiplied with the energy ratio. Thus, it directly represents the influence of the different fabrication steps to the over-all loss.
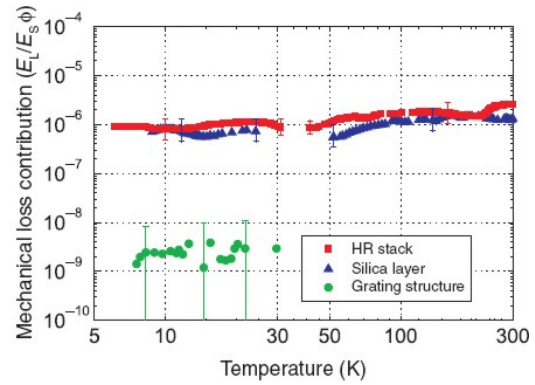
Fig. 2: Contribution of the different fabrications steps to the over-all mechanical loss extracted from the values of fig. 1.

The possible influence of a grating to the total mechanical loss of an optical component is by orders of magnitude lower than any contribution of a dielectric layer. Therefore, the influence of the grating structure can be neglected.

Summary

The measurements showed for the first time that optical gratings applied to the surface of a test mass of a gravitational wave detector does not increase thermal noise. Thus, these results open a further possibility of noise reduction by means of novel techniques for interferometric gravitational wave detectors.

References

[1] K.X.Sun, R.L. Byer, 1997 Opt. Lett. 23, pp. 567-9.

[2] H.B. Callen, T.A. Welton, 1951 Phys. Rev. 83, pp. 34-40.

[3] S. Rowan et al. 1997 Physics Letters A 227, pp. 153-8.

[4] R. Nawrodt et al. 2006 Cryogenics 46, pp. 718-23.

[5] A. Zimmer et al. 2007 Rev. Sci. Instr. 78, pp. 063905-1 - 8.

[6] R. Nawrodt et al. 2007, New Journal of Physics 9, pp. 225.

Investigation of the mechanical losses in a dielectric thin-layer in the temperature range from 5 to 300 K

M. Hudl, R. Nawrodt, A. Schröter, W. Vodel, A. Tünnermann[*] and P. Seidel

[*] Institut für Angewandte Physik, A.-Einstein-Str.15, 07745 Jena

Introduction

The aim of our investigation was to measure the mechanical losses of a silicon-flexure with a thin silica (SiO_2) layer applied to one side. SiO_2 layers are used for the multilayer coatings in the mirrors of interferometric gravitational wave detectors. Thermal noise – which is the limiting noise source within the detection band of these detectors – arises mainly from the mechanical dissipation of the dielectric layers. Thus, it is of interest to investigate the properties of such layers and understand the underlying dissipation processes.

Theory

The observed damping for the free decaying oscillation of the silicon-flexure is a consequence of several dissipation processes in the flexure and the applied dielectric layer. The mechanical loss of the layer ϕ_{layer} can be calculated from:

$$\phi_{total}(\omega) = \phi_{flexure} + \frac{E_{layer}}{E_{flexure}}\phi_{layer}, \qquad (1)$$

with E_{layer} and $E_{flexure}$ as the energy stored in the layer and in the flexure [1].

Setup

The sample was a block-shaped silicon-flexure with a 500 µm thick clamping block (D) on one side and an approx. 50 mm long (l), 8 mm width (b) and 70 µm thin oscillating silicon-flexure (d) on the other side (see Fig.1). The cantilever was produced using a reactive ion-beam etching. The dielectric layer was applied to the thin part and the sample was mounted with the clamping block on a special designed sample holder inside a cryostat. The

eigenmodes of the flexure were exited by applying an alternating electrical field to a comb-like driving plate. The oscillation of the flexure was measured using a commercial laser interferometer [2, 3].
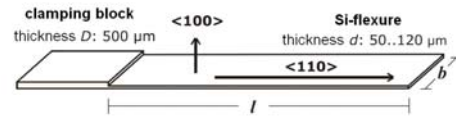
Fig. 1: Sample geometry with clamping block (left) and silicon-flexure (right).

Results

A (400 ± 50) nm thick SiO_2 layer was sputtered on the silicon-flexure. The first five eigenmodes were measured in a temperature range from 5 to 300 K. For temperatures larger 150 K the measured losses were dominated by the thermo-elastic damping of the silicon flexure [1], (see the green curve in Fig. 2) and no layer-losses could be calculated.
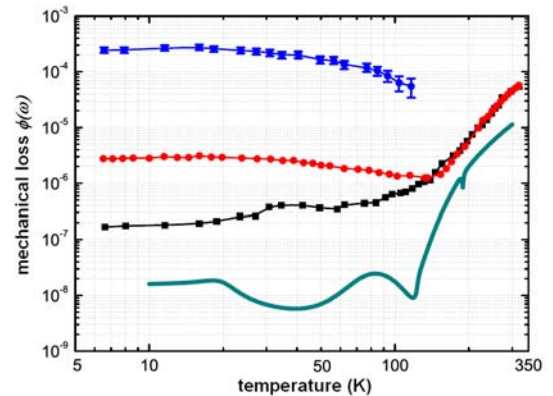
Fig. 2: Mechanical losses for the 2. mode at 2808 Hz depending on the temperature with the calculated losses in the SiO_2 layer (blue), the measured losses in the coated flexure (red) and uncoated flexure (black) and the theoretical calculated under limit.

Summary

In summary, we were able to calculate the mechanical losses associated with the SiO_2 layer in the temperature range from 5 to 150 K. The mechanical loss varies between 0.2×10^{-4} and 3.0×10^{-4} (Fig. 2, Fig. 3). A dependency for the mechanical losses in the layer proportional to the frequency was observed (Fig.3). Measurements of Ta_2O_5 layers show significant higher mechanical losses [4].
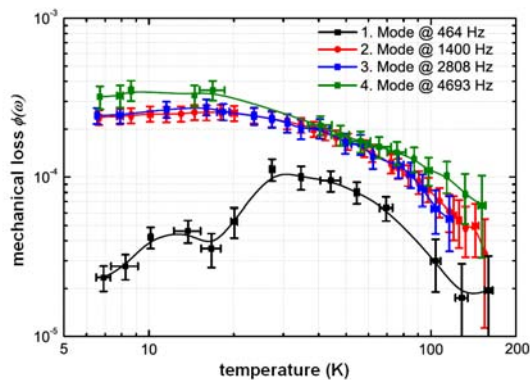
Fig. 3: Mechanical losses in the SiO_2 layer for 4 frequencies depending on the temperature - 464 Hz (black), 1400 Hz (red), 2808 Hz (blue) and 4693 Hz (green).

References

[1] S. Reid et al. 2006 Physics Letters A 351 pp. 205-11.
[2] R. Nawrodt et al. 2006 Cryogenics 46 pp. 718-23.
[3] M. Hudl, diploma thesis FSU Jena (2007).
[4] I. Martin et al. talk at the 4th ILIAS-GW Annual General Meeting Tübingen (2007).

A cryogenic current comparator for beam diagnostics in the FAIR project

A. Steppke, R. Geithner, R. Neubert, W. Vodel and P. Seidel

The non-destructive measurement of beam currents has been successfully achieved using DC beam transformers [1-3]. A much higher accuracy for the FAIR project can only be achieved using cryogenic current comparators (CCC) with superconducting technologies.

A cryogenic current comparator is based on the properties of ideal superconductors to expel magnetic flux from the bulk material through shielding currents on the surface of the material. As this effect is only depend-
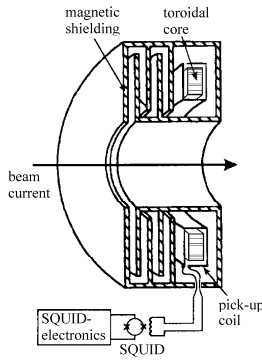
Fig. 1 Principle of a cryogenic current comparator.

ent on the magnetic field of the beam currents, they can be measured non-destructively with a high precision.

In figure 1 the main components of a CCC are shown. The magnetic field of the beam current creates shielding currents on the superconducting magnetic ring structure, which are converted with a torodial single turn pick-up coil and its ferromagnetic core. The signal from the pick-up coil is feed to a LTS DC SQUID and measured via the external electronics.

The design of a CCC requires a thorough knowledge of several noise contributions to achieve a high beam current resolution. As the SQUID and the pick-up coil are very sensitive to external magnetic fields it is necessary to shield both sufficiently against any field sources other than the magnetic field of the ion beam. Grohmann et al. [4, 5] analyzed coaxial cavity structures to suppress unwanted field components. Using this knowledge the current CCC uses a su-

perconducting niobium shield to attenuate non-azimuthal field components by a factor of 120 dB [6].

As external disturbances can be effectively reduced we looked at the influence of thermal noise and the ferromagnetic core material to the overall system resolution. The thermal noise generates a noise cur-
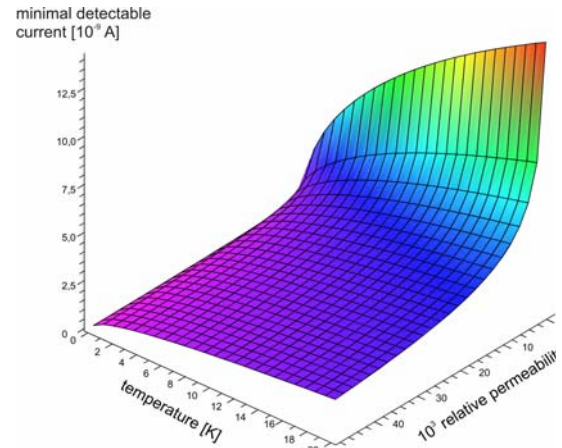
Fig. 2 Minimum detectable current in dependence on temperature and relative permeability of the core material

rent $\sqrt{\langle I^2 \rangle}$, which in connection with the inductance L generates a magnetic flux noise $\Phi_{thermal}$ which cannot exceed the magnetic flux due to the beam current for a signal to noise level of unity.

$$\Phi_{beam} = \int_A \vec{B} \cdot d\vec{f} \geq \Phi_{thermal} = L \cdot \sqrt{\langle I^2 \rangle}$$

For a given pick-up coil the minimum detectable current I_s is dependent on the geometry of the coil ($f(R_a, R_i, b)$), the temperature T, the geometric inductance L and the relative permeability μ_r of the ferromagnetic core material according to:

$$I_s = \frac{2\pi \sqrt{k_b T L}}{\mu_0 \mu_r f(R_a, R_i, b)}$$

In figure 2 we calculated the resolution which corresponds to the minimal detectable current, which can be detected for different temperatures and relative permeabili-

ties with the currently used single turn toroidal pick-up coil.

The basic analysis of the detectable current shows a strong dependency on the relative permeability of the core material. As the pick-up coil is fully embedded within the superconducting shield, the core material has to operate at temperatures in the range of 4.2 K. In standard ferromagnetic materials the permeability decreases by about two orders of magnitude from room temperature to these low temperatures. Our first measurements showed a reduction of inductance of coils using Amidon iron powder cores from 450 μH to 4 μH at 4,2 K. Using this knowledge it is necessary to investigate a wide range of ferromagnetic materials at low temperatures in respect to their permeability. The measurement setup includes a high-precision inductance bridge (Agilent E4980A LCR-Meter) connected to our dipstick in a helium cryostat. A temperature sweep can be achieved with a computer controlled stepper motor, which adjusts the level of the dipstick in respect to the helium bath. With this setup the material Vitrovac VC6025, was measured over a temperature range from 290 K to 1,9 K, which is shown in figure 3.
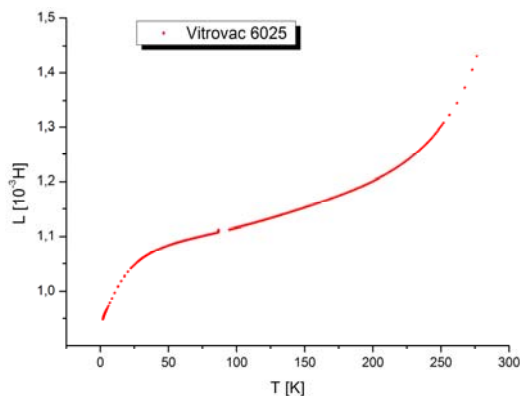
Figure 3: Inductance of a test coil with Vitrovac VC6025 as the core material in dependence on temperature

The inductance of the test coil decreases by 52% over the whole temperature range which shows that the currently used material is already a large improvement over sintered iron powder cores. The high permeability in group of Vitrovac materials is highly dependent on the heat treatment of the final material which influences for example the size of the magnetic domains.

Frequency dependencies have also been measured in nanocrystalline materials, e.g. Magneperm. The current results show the different ferromagnetic materials exhibit significant temperature- and frequency dependencies, which have to be evaluated to achieve a high accuracy of the CCC in the final application.

The theoretical investigations showed that with a strong attenuation of external noise sources an improvement of the sensor performance is dependent on the ferromagnetic core material. The current approximation for the minimum detectable current needs to be further extended with the fluctuation-dissipation theorem to analyse the frequency-dependence of the thermal noise. With the first measurements of different core materials we could characterize the inductance over a wide temperature range and show first frequency dependencies. Future measurements will include a direct noise measurement using a DC SQUID to readout thermal noise signals at low temperatures.

References

[1] K. B. Unser, "The parametric current transformer", AIP Conf. Proc., 252, April 5, 1992, pp. 266-275

[2] I. K. Harvey, "A precise low temperature dc ratio transformer", Rev. Sci. Instrum., 43, 1972, p. 1626.

[3] P. Gutmann and H. Bachmair; in V. Kose, Superconducting Quantum Electronics, Springer Verlag, 1989, pp. 255-259.

[4] K. Grohmann, et. al., Cryogenics 16, July 1976, pp. 423-429.

[5] K. Grohmann, et. al., Cryogenics 16, October 1976, pp. 601-605.

[6] W. Vodel, R. Neubert, S. Nietzsche, K. Knaack, K. Wittenburg and A. Peters, IEEE Trans. Appl. Superconductivity, Vol. 17, 2007, pp. 621-624

[7] H. P. Quach and T. C. P. Chui, Cryogenics 44, 6-8, August 2004, pp. 445-449

Characterization of 3-dimensinal superconductive thin film components

S. Hechler, R. Nawrodt, R. Neubert, W. Vodel, H. Dittus[*], F. Löffler[**] and P. Seidel

[*] ZARM – Universität Bremen, Am Fallturm, 28359 Bremen

[**] Physikalisch-Technische Bundesanstalt, Fachbereich 5.5, Bundesallee 100, 38116 Braunschweig

Introduction

Superconducting Quantum Interference Devices (SQUIDs) are used for high precision gravitational experiments [1]. One of the most impressive experiments is the Satellite Test of the Equivalence Principle (STEP) [2] of NASA/ESA. The STEP mission aims to prove a possible violation of Einsteins's Equivalence Principle at an extreme level of accuracy of 1 part in 10^{18} in space [3]. In this contribution a characterization of the superconducting components like e.g. pick-up coils is necessary. This characterization is done by measurements of the transition temperature between the normal and the superconducting state.

Theory

By investigations of the superconducting transition many properties of the samples can be found. The transition temperature for example gives us a clue of the quality of the thin film. Thus advantages and disadvantages of the production processes of the thin film can be evaluated. A high transition temperature is necessary for a stable measurement operation. The width of the superconducting transition in combination of the resistivity ratio indicates the impurity concentration within the thin layer. With the help of these parameters it is possible to estimate the qualification of the sample in order to reach the given aim.

Experimental Setup

The investigation of the super-conducting transition was done using an automatically working measurement equipment. This setup was specially designed and developed for the characterization of the 3-dimensional superconducting thin film components (Fig.1). Above all the setup was designed for use in normal LHe transport Dewars. The sample camber, which has a volume of 150 cm^3, can be fully temperature controlled over a range from 4.2 K to 300 K with a resolution of better than 100 mK. In addition a heating coil, made of Manganin wire, was wrapped up the sample camber. For precise temperature control a temperature sensor is located on this cover. In Fig. 1 you can see the completed experimental assembly with an accurate calibrated LakeShore Cernox resistor as temperature sensor.

Sample Preparation

The prototype of the Niobium thin film pick-up coil for the STEP experiment was sputtered onto a cylinder (diam. 10 mm, length 10 cm) made of Zerodur, a special type of ceramic with a very low thermal expansion coefficient. After this the coil structure was mechanical grinded into the Niobium layer. The coils were bonded supersonductivly in 4-point alignment with the help of niobium wires. The temperature
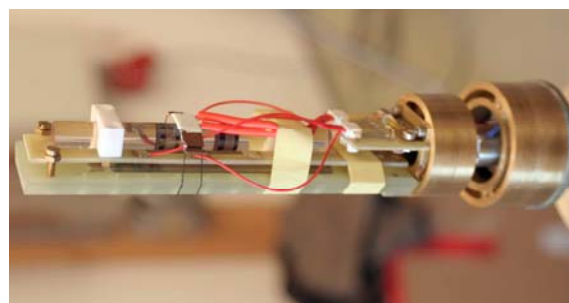
Fig. 1: Lower end of the anticryostat with the pick-up coil prototype on the career. On the right you can see the two cones, which carry the sample camber and the isolating vacuum covers.

sensor is located beside the coil. It is clamped by a clip made of tombac, a special brass alloy.

Results

Fig. 2 and 3 represent the measured transitions between the normal and the superconducting state of the two niobium coils.

Fig 2 shows the values for first coil (on the left side in Fig. 1) using various currents during the measurement. As you can see the transition performs in two steps with different heights. A part of coil 1 has differing
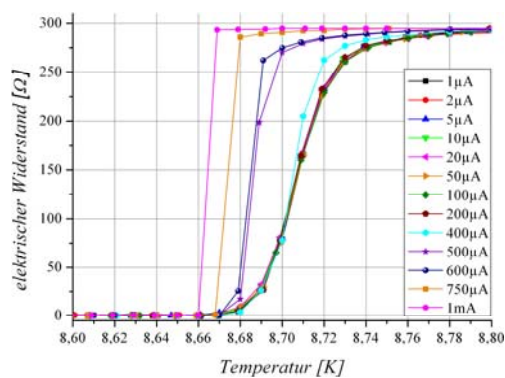
Fig. 3: Measured values of the superconducting transition of Niobium coil 1. In the caption you can find the current, which was used during the measurement. The measured critical temperature is about (8,71±0,06) K.

characteristics which results a lower critical temperature. I suppose the reasons for those disparities are inhomogenities and impurities inside the Niobium thin film resulting form the deposition process. Thus the first step between 8,50 K and 8,61 K is effected. The allover transition width is about 150 mK. For currents greater than 500 µA the critical temperature is lowered by the dissipation of thermal energy and the resultant self heating. The measured critical temperature for this coil is (8,57±0,06) K.

Fig 3 contains the measured values for the second Niobium structure. A distinction in different steps is not recognized. The structure seems to be more homogeneous than the first. The acquired critical temperature has a value of (8,71±0,06) K. Therefore there is a difference between the two coils of nearly 150 mK. Also the transition width varies. In case of the second coil it is only
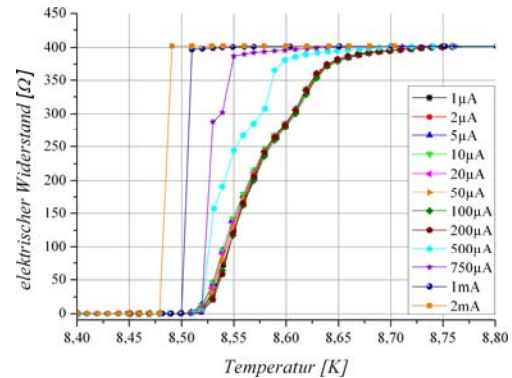
Fig. 2: The superconducting transition of the second Niobium coil. The value of the used current is located in the caption. The measured transition temperature is (8,57 ± 0,06) K.

about 50 mK wide. This is another indication for a higher purity of this Niobium structure. For currents greater than 400 µA the critical temperature is lowered by the same reason like even.

The measured values for transition width and temperature coincide with investigations by Mayadas et al. [4]. Also the resistivity ratios of 2,4 for coil 1 and 2,5 for coil 2 are matching. With the help of these values the thickness of the Niobium layer can be estimated to 30 nm to 40 nm.

Summary

The measurements showed precise values of the superconducting transition for this type of Niobium thin film structures for the first time. Thus, these results open a possibility for further development of the pick-up coils for the position detector system of the STEP-Mission.

References

[1] S. Nietzsche 2001 PhD-Thesis FSU Jena.
[2] Homepage University Stanford http://einstein.stanford.edu/step/
[3] H. Dittus, W. Vodel 2000 Praxis der Naturwissenschaften 49.
[4] A.F. Mayadas et al 1972 J. Appl. Phys 43.
[5] D.K. Finnemore et al 1966 Phys. Rev. 149.

FLOW OPTIMIZATIONS OF COMPONENTS OF A COAXIAL TWO-STAGE PULSE - TUBE REFRIGERATOR

F. Richter, T. Koettig, M. Thürk, and P. Seidel

The coaxial two-stage pulse tube refrigerator (PTR), developed at the institute of Solid State Physics, Cryogenic Department, has a number of components where the gas has to flow evenly [1, 2]. Unevenly spaced gas flow causes unintentional heat transfer or the obstruction of the gas transport in the operating cycles [3, 4]. Therefore we analyze the gas flow pattern in areas which are seen as critical in forming flow for the main components. The most important area is indicated in Fig. 1. There are other components that were analyzed too, but the most work and improvements were made here.
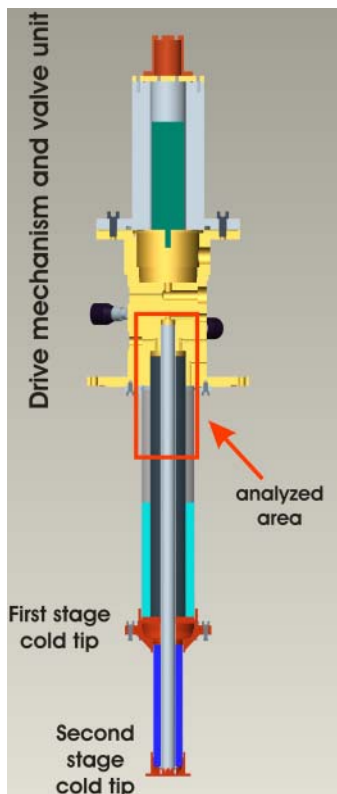
Figure 1: Sectional View of the two stage PTR in coaxial design. Highlighted square marks analyzed components.

The first step in analyzing the current status of flow in the designated component is to build up a practical measurement device.

The most suitable measurement system for the given requirements is *Hot-Wire-Anemometry* [5, 6]. To separate the effects of the flow from thermal effects in the refrigerator and to not damage or modify the PTR, a full scale replica of the selected components was made.
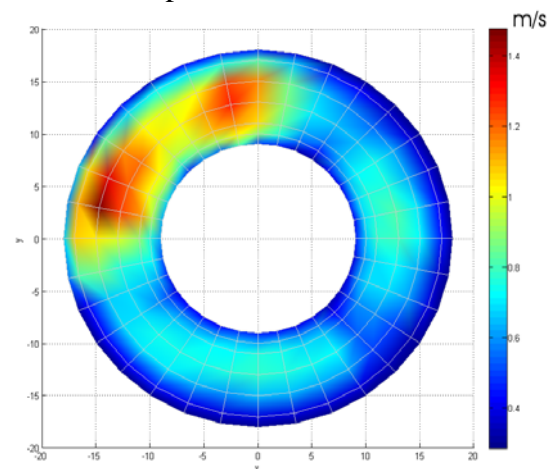
Figure 2: Gas flow spread in the first plate showing the status quo at beginning of the experiments. The velocity is measured in a depth of 11 cm.

The highlighted square in Fig. 1 contains the second and first stage pulse-tube, which have their warm end here.

Gas is blown in both tubes but in the first stage pulse tube the gas is feeded in at one side of ring-shaped space while in the second stage pulse tube the gas joins a circle space centrically. Therefore the second stage pulse tube the gas can build up a regular flow profile but in the first stage pulse tube the gas flow first has to be redirected to get a regular spread.

As shown in Fig. 2 measurements feature a highly uneven flow pattern even after eleven centimetres of undisturbed flow-stratifier. After developing new plates with different arrangements of holes, an improved plate design was constructed and is shown in Fig. 3. The associated flow profile is shown in Fig. 4. When Fig. 2 and

4 are compared, the conclusion is a visible improvement in equability of the gas flow.

Figure 3: New modified plate of brass which is orientated in Figure 4. Inflow is at the right-hand side the separated small hole.
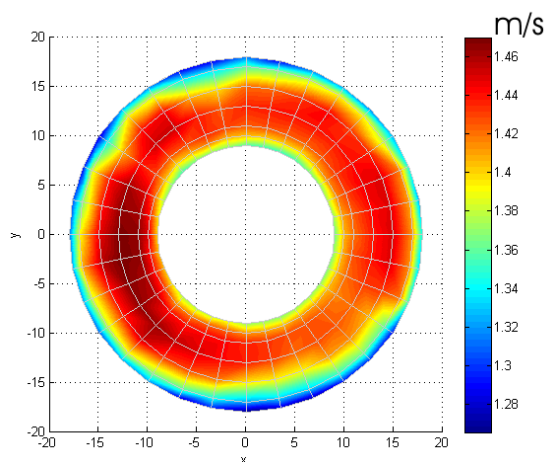
Figure 4: Gas flow spread in modified plate. The velocity in 11 cm depth within the ring-shaped space is shown.

Important to mention is that scales are different in Fig. 2 and Fig. 4, but the main statement is the plateau form in Fig. 4. At all points on the ring the gas flow velocity has nearly the same value. There were also plates tested which improve the reached top speed within the ring-shaped space but reduce equability of the gas flow. Higher top velocity doesn't improve the lowest reached temperature but often gets it worse. The accomplished changes for baffle plates and the achieved equal flow

pattern reduce the cooling temperature in both stages.

The first stage cold tip changes from 47 K to 38 K and the second stage cold tip changes its reached no-load temperature from 6.5 K to 5.7 K.

CONCLUSIONS

Forming gas flow in critical components affects first and second stage cold tip and decreases the lowest reachable temperature.

Due to the significant improvement reached in no-load temperature while improving stream in this component, further analyses and improvements should be considered. The hypothesis to evenly distribute the gas flow was a success and should be continued for other components. A maximum possible velocity isn't that desirable than a balanced flow pattern. Nevertheless both parameters are related to each other and should not be analyzed for their own while optimizing no-load temperature.

Under these aspects other components inside the PTR will be analyzed and optimized too.

REFERENCES

[1] Koettig, T.; Moldenhauer, S.; Nawrodt, R.; Thürk, M.; Seidel, P.: Two-stage pulse tube refrigerator in an entire coaxial configuration. In: Cryogenics **46** (2006), p. 888-891.
[2] Koettig, T.; Nawrodt, R.; Thürk, M.; Seidel, P.: Performance Characteristic of a Two-Stage Pulse Tube Refrigerator in Coaxial Configuration. In: Cryocoolers 14, 2007 (International Crycooler Conference), p. 171-176.
[3] Frey, H. ; Haefer, R. A.: Tieftemperatur-technologie. Düsseldorf : VDI-Verlag, 1981.
[4] Rühlich, I.: Strömungstechnische Optimierung von Regeneratoren für Gaskältemaschinen.
Düsseldorf : VDI Verlag, 1999 (Fortschr. Ber. VDI Reihe 19 Nr. 122).
[5] Bruun, H.H.: Hot-wire anemometry. (principles and signal analysis). Oxford
Science Publications, 1995.
[6] Ermshaus, Dr. R.: Hochschulkurs Hitzdrahtanemometrie Grundlagen, Grenzen,
Möglichkeiten. Institut für Hydromechanik, Uni Karlsruhe, 1995.

Thermodynamic characterization of novel material for low-temperature regenerators

T. Koettig, F. Richter, R. Nawrodt, M. Thürk, and P. Seidel

Pulse tube refrigerators require regenerators with very high efficiency. A low value of pressure drop (friction factor) of the penetrating helium gas flow through the solid state regenerator material is needed. Otherwise a high heat transfer rate at the surface and a high heat capacity have to be realized by the same regenerator stack [1]. Fig. 1 shows the novel regenerator geometry that was developed and introduced [2]. The lead coated screen material combines the advantage of screen
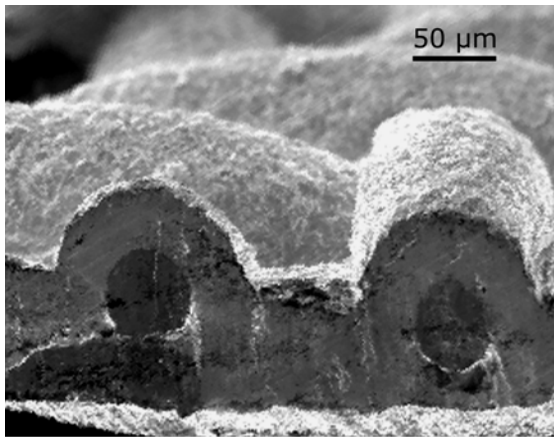
FIGURE 1 SEM picture of a electroplated screen. A sectional cut of original bronze screen with a lead coating of about 35 µm with well-developed surface.

material concerning the friction losses with the high heat capacity of lead (normally used as packed spheres with a diameter of about 200 µm) [3, 4].
The relation of the numbers of transferred heat (NTU) to the numbers of pressure heads (NPH) characterizes the ability as a regenerator material. Low values of the quotient NPH/NTU are requested.

EXPERIMENTAL SET-UP

A variable test facility was designed and built-up to compare different standard regenerator geometries with the electroplated screen material.

FRICTION FACTOR f (NPH)

Interchangeable sample tubes guarantee the zero compensation and the comparative measurement of the pressure drop of different matrix geometries [2].
The numbers of pressure heads and the friction factor are defined as follows:

$$NPH = \frac{f \cdot L}{d_h} = \frac{\Delta p}{\frac{\rho}{2} \cdot w^2} \quad , \quad (1)$$

with the length L, the measured pressure difference Δp, the hydraulic diameter d_h, the density ρ and the velocity w.
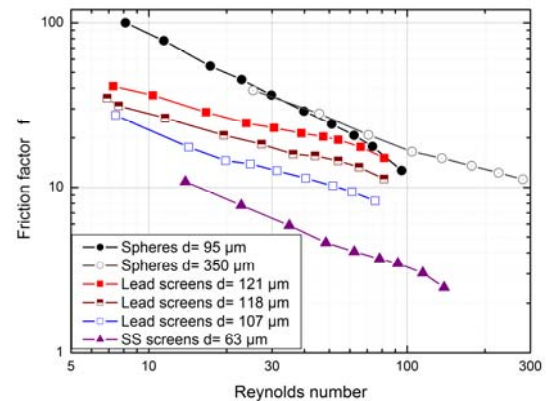
FIGURE 2 Comparison of the friction factor of selected screen geometries with packed spheres. All screen geometries consist of 160 mesh (wires per inch).

The main point of interest is the comparison of the coated screens with state of the art packed spheres and standard screens, as it is shown in Fig 2. Lead coated screens integrate between the original screen material and packed spheres. Hence, lead coated screens open up the possibility of inhomogeneous regenerator stacks and tuneable pressure drops by varying the coating thickness.

HEAT TRANSFER (NTU)

Combined with the flow involving friction through a porous media a heat

transfer between the fluid flow and the regenerator matrix occurs. The more effective this heat transfer is the less the regenerator loss is. To characterize the quantity of transferred heat the numbers of transfer units NTU are defined [1]:

$$NTU = \frac{\alpha \cdot S}{\dot{m} \cdot c_{p,Fl}} = \frac{j}{Pr^{2/3}} \cdot \frac{4 \cdot L}{d_h} \quad , \qquad (2)$$

where α is the heat transfer coefficient; $\dot{m} \cdot c_{p,Fl}$ is the heat capacity flow rate of the fluid; S is the surface of the regenerator matrix; j is the Colburn-modulus; Pr is the Prandtl number; L is the length and d_h is the hydraulic diameter.
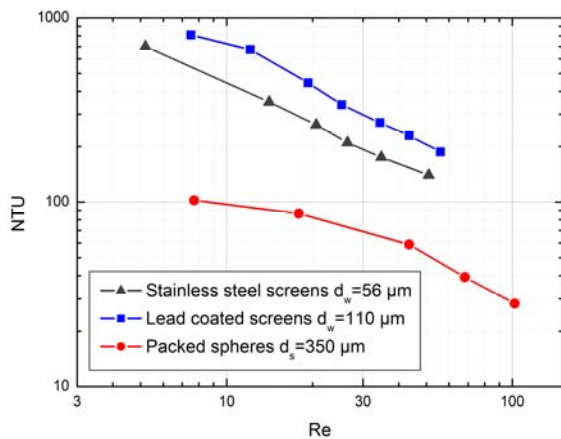
FIGURE 3 Numbers of transfer units (NTU) versus the Reynolds number Re of three different regenerator geometries.

Fig. 3 shows that lead coated screens achieved the greatest heat transfer rates, followed by the standard screens and packed spheres with the typically lower heat transfer. If one compares the numbers of pressure heads with the numbers of transfer units a dimensionless value of the suitability of a heat storage matrix can be found [2]. Low values of the pressure loss per heat transfer unit are requested. Fig. 4 shows the relation of NPH/NTU on the investigated regenerator geometries. Standard screens reach the lowest value. Lead coated screens close the gap between packed spheres and the screen geometry. In addition there is still the possibility to vary the electroplating parameters of the coated screens.
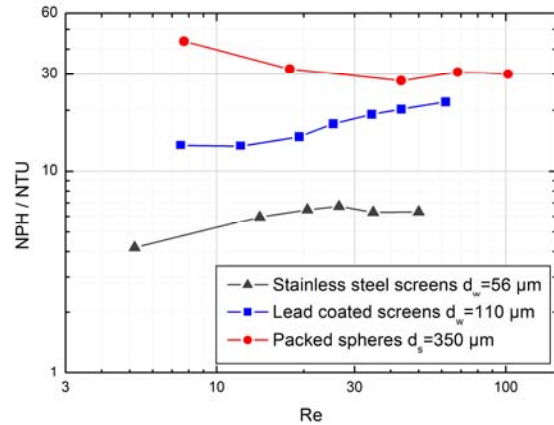
FIGURE 4 Comparison of the suitability to regenerative heat storage using the dimensionless relation NPH/NTU versus the Reynolds number. Low values of NPH/NTU characterize a good regenerator material.

CONCLUSIONS

We demonstrated the utility of lead coated screens to build up high efficient regenerator stacks. The achieved values of heat transfer per friction loss of electroplated screens are higher than these of packed spheres. Coated screens are tuneable regarding to the pressure drop and their heat transfer surface. The application in a new developed two-stage pulse tube refrigerator in a totally coaxial design of the cold finger combines the advantages of screen regenerators with the high heat capacity of lead in the low temperature region [5].

REFERENCES

[1]Ackermann, R. A., *Cryogenic Regenerative Heat Exchangers*, The international cryogenics monograph series, 1997.
[2] T. Koettig, F. Richter, R. Nawrodt, A. Zimmer, C. Schwarz, D. Heinert, M. Thürk, and P. Seidel, Application of novel regenerator material within a coaxial two-stage pulse tube refrigerator, CEC 07, Chattanooga, to be published.
[3] Wang C, Thummes G, Heiden C, Experimental study of staging method for two-stage pulse tube refrigerators for liquid 4He temperatures. Cryogenics 1997;37:857-863.
[4] Wang C, Helium liquefaction with a 4 K pulse tube cryocooler. Cryogenics 2001;41:491-496.
[5] Koettig, T. Moldenhauer, S., Nawrodt, R., Thürk, M., and Seidel, P., *Cryogenics,* **46**, pp. 888-891 (2006).

3. Technical reports and equipments

Operation of the Ion-accelerator JULIA and the Ion-implanter ROMEO

U. Barth, F. Jehn, G. Lenk, W. Wesch, W. Witthuhn

The 3 MV high current tandetron accelerator **JULIA** (*J*ena *U*niversity *L*aboratory for *I*on *A*cceleration) went in operation end of 1996. Since the beginning of the routine-operation in 1997 it has been used for different types of experiments requiring a broad spectrum of ion-beams. With the exception of Helium, where the duoplasmatron ion-source followed by a Lithium exchange channel was used, all ions were extracted from a sputter-type ion-source. The beam-on-target-time of 1438 h was in the same order of magnitude as in the preceding years. The 400 kV ion-accelerator **ROMEO** is in routine operation since 1998, here the beam-on-target-time of 1120 h was higher than in 2006.

Both accelerators can be operated separately or in combination. The ion-beams produced during the period 2006 are summarized in table 1. The ion-beam currents quoted are typical values of the ion source currents used for the experiments, the maximum currents available are significantly higher for most ions.

During 2007 both accelerators were operated routinely. Technical problems arose with (1) the vacuum system of the implanter and (2) the computer-controlling of the tandetron accelerator. In this context one has to realize that important parts of the accelerator facility are now running since 10 years. Here reinvestments will be necessary in the next future.

In 2007 some components of the 3 MV-Tandetron accelerator „JULIA" and of the 400 kV Ion-Implanter „ROMEO" were further developed:

1. At the 30° beam line of the Ion-accelerator „JULIA" a new vacuum chamber equipped with the set up for PIXE analysis was installed. This included the build-up of systems for beam guiding, beam collimation and beam current measurement. The vacuum system was equipped with computer control.

2. For the accelerator „ROMEO" a computer controlled system for spectrum analysis was developed including hard and soft ware for recording and evaluating implantation parameters.

Table 1. Ion-beams accelerated during 2007. The currents given are measured at the Q-Snout-Faradaycup after the low-energy mass separator (JULIA) and at the target position (ROMEO), respectively.

Period	Element	Julia	Romeo
1	Hydrogen (H)	5 µA	4 µA
	Helium (He)	0,2 µA	4 µA
2	Lithium (Li)	2 µA	1 µA
	Boron (B)	0,2 µA	5 µA
	Carbon (C)	9 µA	10 µA
	Nitrogen (N)	10 µA	4 µA
	Oxygen (O)	17 µA	2 µA
3	Sodium (Na)	-	6 µA
	Magnesium (Mg)	-	5 µA
	Aluminium (Al)	-	4 µA
	Silicon (Si)	16 µA	4 µA
	Phosphorus (P)	-	4 µA
	Argon (Ar)	-	200 µA
4	Calcium (Ca)	-	5 µA
	Titanium (Ti)	0,7 µA	-
	Vanadium (V)	0,2 µA	1 µA
	Manganese (Mn)	0,017 µA	5 µA
	Chromium (Cr)	0,2 µA	3 µA
	Iron (Fe)	0,8 µA	2 µA
	Cobalt (Co)	-	3 µA
	Nickel (Ni)	-	6 µA
	Zinc (Zn)	1 µA	6 µA
	Gallium (Ga)	1 µA	3 µA
	Germanium (Ge)	1,6 µA	4 µA
	Arsenic (As)	0,4 µA	10 µA
	Selenium (Se)	0,5 µA	15 µA
	Bromine (Br)	19 µA	8 µA
	Krypton (Kr)	-	10 µA
5	Rubidium (Rb)	0,075 µA	1 µA
	Zirconium (Zr)	0,3 µA	1,5 µA
	Rhodium (Rh)	0,2 µA	-
	Palladium (Pd)	0,095 µA	10 µA
	Silver (Ag)	-	10 µA
	Cadmium (Cd)	-	4 µA
	Indium (In)	5 µA	8 µA
	Tin (Sn)	-	3 µA
	Antimony (Sb)	-	4 µA
	Tellurium (Te)	-	2 µA
	Xenon (Xe)	-	10 µA
6	Praseodymium (Pr)	-	1 µA
	Samarium (Sm)	0,01 µA	1,5 µA
	Europium (Eu)	0,035 µA	2 µA
	Gadolinium (Gd)	0,03 µA	-
	Erbium (Er)	0,04µA	2µA
	Tantalum (Ta)	0,2µA	2 µA
	Tungsten (W)	0,3µA	0,01µA
	Osmium (Os)	0,05 µA	-
	Iridium (Ir)	0,3µA	6 µA
	Platinum (Pt)	0,2µA	-
	Gold (Au)	24µA	20µA
	Lead (Pb)	0,035 µA	15µA
	Bismuth (Bi)	-	3µA

[1] Strom nach LE-Massenseparator im Q-Snout-Faradaycup gemessen

[2] Strom auf Target gemessen

As in the preceding years the ion-beam facility
was used by external research groups:

3MV-Tandetron „JULIA"

University Jena
University Göttingen (Mr. Lange)
University Freiberg (Dr. Bollmann)
IPHT Jena (Dr. Diegel)
Paul-Scherrer-Institut (Dr. Grillenberger)

400kV Implanter „ROMEO"

iba e.V., Heiligenstadt
FH München (Prof. Alt)
Universität Halle (Dr. Dubiel)
University Minsk (Prof. Komarow)
University of Pretoria (Prof. Hayes, Prof. Fried-
land)

3 MV-Tandetron "JULIA"

- IFK
- Universities
- Institutes and Industry

2%
48%
50%

400 kV Implanter "ROMEO"

- IFK
- Universities
- Institutes and Industry

25%
44%
31%
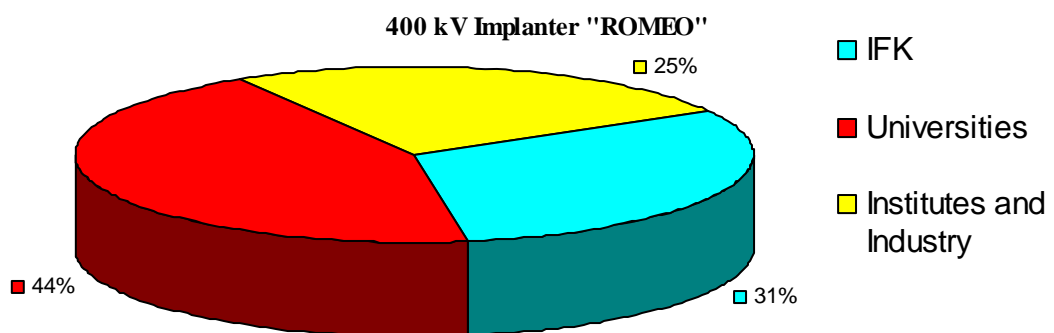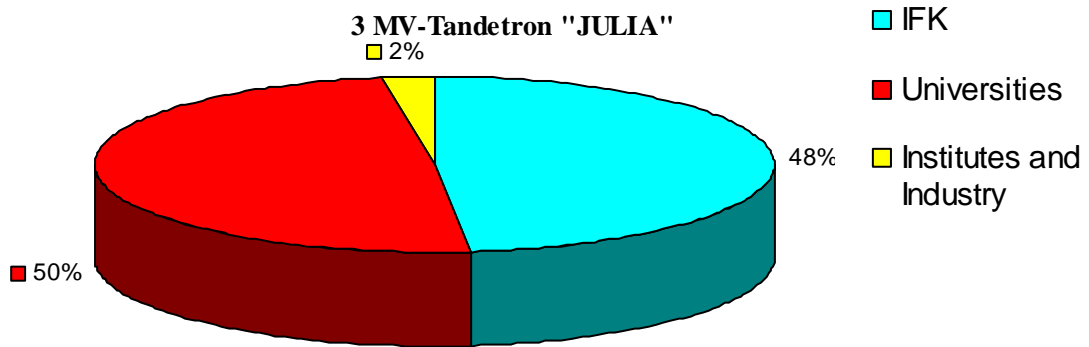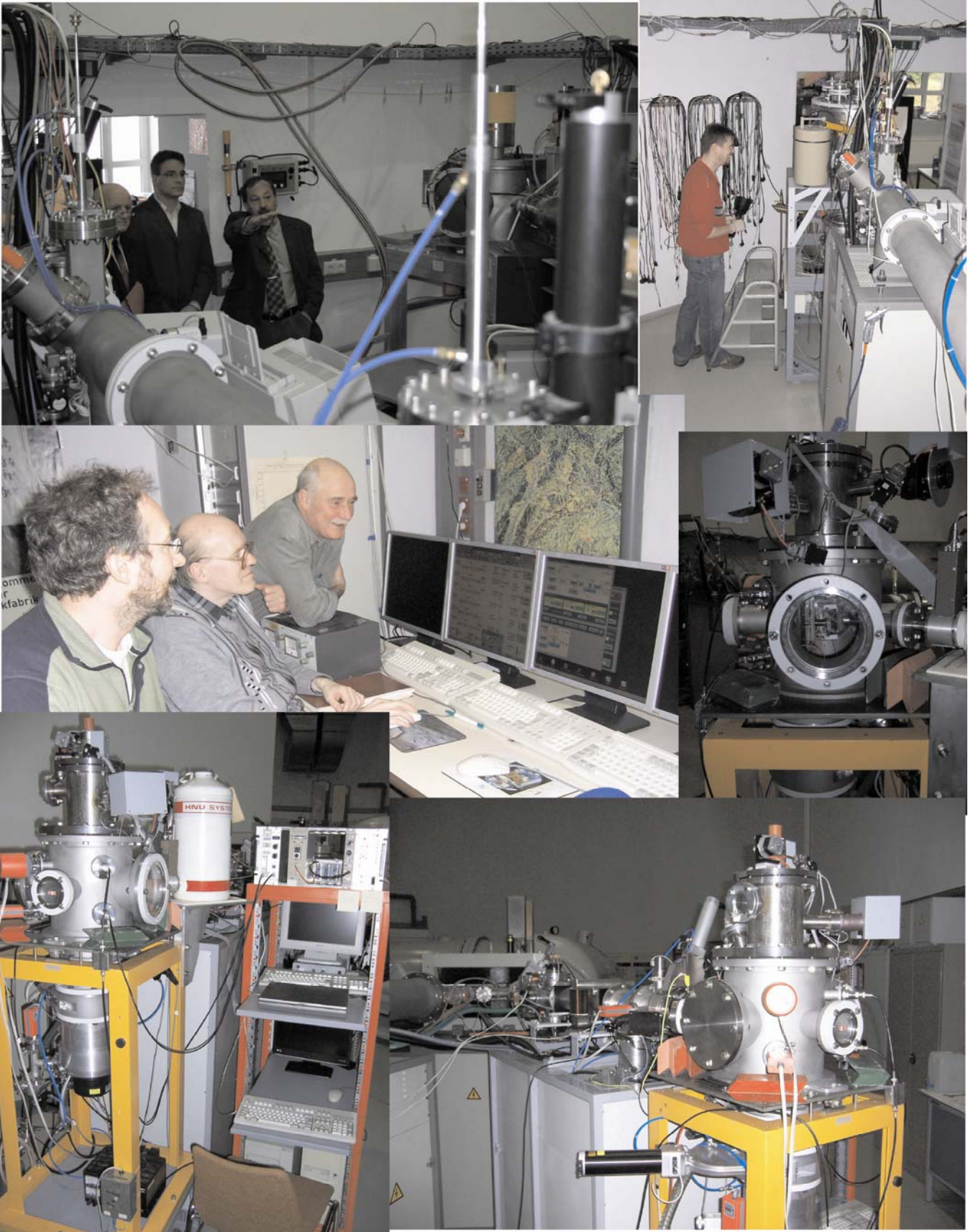
Cryogenic Services 2007

All in-house customers of cryogenic liquids which are all faculties of natural sciences, the medical division of the university, including several hospitals, and other external scientific institutes (e.g. Institute for Physical High Technology Jena, , Leibnitz Institute Hans-Knöll Jena) as well as some private customers like the Innovent e.V. Jena or some medical practices were provided with liquid Helium (LHe), high purity gases (He, N_2) and with liquid nitrogen (LN_2) by the Cryogenic Services. More than 115 000 litres of LN2 were delivered by the cryogenic services this year.
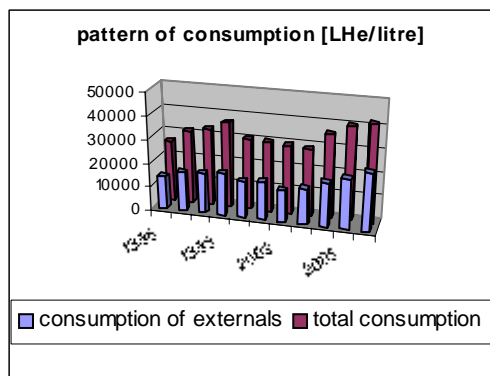
Fig. 1.: Consumption of liquid helium

As illustrated in Figure 1, the production of LHe has stabilised in 2007 at a very high production level , which is due to the increasingly modern and high technology equipment for scientific research as well as for the upgrading medical care in the high-technology region within and in the periphery of the city Jena.

Roughly **40 500** litres of LHe were produced which is near the highest value ever reached with the installed liquefier LINDE LR-20 equipment in 2006. These results were achieved by the staff in spite of expanded reconstruction periods. Merely 24% of the whole output is used by the Physic faculty themselves this year. The liquefaction capacity of the facility has been increased since the beginning of the operation of the equipment starting from the design point of 10 litres/h up to 16 litres/h these days by our staff.

In order to prevent machine downtime periods we installed a new recovery compres-

sor, fig 2, and had to expand the high pressure storage capacity, fig. 3, of the liquefier at the beginning of the year 2007. We would like to acknowledge the helpful financial backing of all users who sponsored these inevitable final repairs which was amounting to a value of roughly 27 thousand Euro.

F*ig. 2: Recovery compresso*r

Fig. 3: Extension of the high pressure tank

With a very late beginning at October the 15th we were able to start the reconstruction of the old liquefier. We acknowledge gratefully the financial backing of the reconstruction by the administration of the Free State of Thuringia with a amount of 1.2 Mio Euro.

The scheduled amount of 500.000 € which has to be spend still in 2007 were realised according to the plan. We start the reconstruction of the water supply facility, fig. 4, of the electrical equipment and first workings on the building structure, fig. 5.

Fig.4:Air conditioning   *Fig.5:Construction works*

Equipment

Preparation of thin films and devices

- HV evaporation facilities for thermal evaporation and rf-sputtering with oxidation system
- UHV evaporation facilities, including electron gun and in situ RHEED system
- Equipment for laser deposition of thin films and material systems, especially high temperature superconductors (KrF excimer laser, $\lambda = 248$ nm)
- Molecular Beam Epitaxy (MBE) facilities:
- MBE for silicon carbide (RIBER EVA 32 R&D)
- MBE for III-V-semiconductors (RIBER EPINEAT III-V S)
- dc and ac sputtering systems for thin films and multilayers
- Ion beam etching with Ar ions at sample temperatures down to 80 K
- Reactive ion beam etching with sample diameters up to 6 cm
- Ultrasonic wire bonder
- Equipment for photolithographic patterning

Surface analysis systems

- AUGER electron spectrometer
- Surface analysis system UNISPEC with XPS, UPS, AES, LEED, STM
- Atomic force microscopes (AFM and Microstructure Measuring Device VERITEKT 3 with needle sensor)
- Surface profilometer DEKTAK 100
- Scanning electron microscopes

Electrical and optical measurement techniques

- Electrical transport measurements (resistance, critical current density, point contact and tunneling spectroscopy)
- Hall-effect and Four-point probe equipment
- Current-voltage characteristics (2 K < T < 300 K, B ≤ 5 T)
- Current-voltage characteristics by microwave irradiation (2 GHz < f < 300 GHz)
- Noise measurements (frequency range 60 µHz - 100 kHz) at low temperatures
- LTS-SQUID characterization at 4.2 K (current-voltage, flux-voltage, noise, screening properties)
- HTS-SQUID characterization up to 100 K (current-voltage, flux-voltage, noise)
- 2 Deep level transient fourier spectrometers (temperature range 80 K - 690 K, 30 K - 330 K)
- 3 Admittance spectrometers (frequency range 40 Hz - 100 kHz, 20 Hz - 1 MHz and 75 kHz - 30 MHz, temperature range 30 K - 690 K)
- Optical microscopes
- Optical spectrometers, wavelength region 200 nm to 40 µm
- Low temperature photoluminescence spectroscopy
- Microwave signal generator (frequency range 1 - 20 GHz, resolution: 1 kHz)
- Electrical and optical characterization of high power diode laser arrays

Equipment for thermal treatment

- Furnace for conventional thermal treatment in inert gas atmosphere or vacuum (temperatures up to 2050 K)
- RTA apparatus (double graphite strip heater) for short time annealing (annealing time in the order of seconds, temperature range 1000 K to 1950 K, temperature rise rate 100 K s^{-1})

Ion beam techniques

3 MV Tandetron accelerator "JULIA", equipped with

- Sputter ion source and Duoplasmatron source
- Universal beam line for ion implantation and ion beam analysis
- Second beam line for ion beam analysis, combined with implantation chamber of 400 kV implanter
- Irradiation chamber with cooled and heated sample holder and four axis goniometer

Application:

- Ion implantation: energy range 500 keV - 12 MeV, temperature range 15 K - 1500 K
- Ion beam analysis: RBS and PIXE in combination with channeling, ERDA

400 kV implanter "ROMEO", equipped with

- Hot filament, hollow cathode ion source
- Irradiation chamber with cooled and heated sample holder and four axis goniometer, combined with beam line of 3 MV Tandetron accelerator

Application:

- Ion implantation: energy range 20 keV - 400 keV, temperature range 15 K - 1500 K
- Ion implantation at low temperatures and subsequent RBS analysis using H- or He-ions from 3 MV Tandetron accelerator

Low Energy implanter "LEILA", equipped with

- Colutron Ion source 100-Q
- Colutron Ion Gun System G-2-D
- Irradiation chamber with heated sample holder

Application:

- Implantation of Hydrogen: energy range sub-keV, temperature range 300 K - 750 K

Nuclear probe technique

- 2 HP Ge-spectrometers

Low temperature measuring equipment

- He-4 cryostats for temperatures down to 4.2 K
- He-4 refrigerator for the temperature range 1.3 K - 4.2 K
- He-3 cryostat for temperatures down to 300 mK
- He-3/He-4 dilution refrigerator with a base temperature of 35 mK
- He-3/He-4 dilution refrigerator with a base temperature of 7 mK
- Electronic equipment for characterization of cryoelectronic devices
- SQUID sensor systems for magnetic measurements under unshielded conditions
- SQUID sensor system for spatially resolved magnetorelaxometry
- Cryostats (2 K < T < 300 K; optical window; magnetic field)
- Cryocoolers (Gifford-McMahon and Stirling)
- Pulse tube refrigerators (for sensor cooling)

CIS-LAB

- MBE system NEBULA for $Cu(In,Ga)S_2$ layers on 4'' substrates including RHEED setup
- Two HV systems for closed-space sublimation (CSS)
- Solar simulator (AM 1.5) with Current-Voltage measurement
- RF reactive sputtering system for transparent conducting oxides (TCO's) and molybdenum
- DC sputtering system for copper and indium
- UHV system ULS400 for $Cu(In,Ga)(Se,S)_2$ on (100x100) mm^2 substrates
- Scanning electron microscope JEOL JSM-6490 with LaB_6-cathode
- Quantum efficiency measurements of solar cells
- Wet chemical processing and chemical bath deposition of photoactive layers

SQUID application laboratories

- Measurement system for non-destructive evaluation in unshielded environment based on high-T_C-SQUID gradiometers
- Heart monitoring system for biomagnetic investigation in unshielded environment based on high-T_C-SQUID gradiometers
- High precision position detection system based on low-T_C-SQUIDs
- Magnet-Relaxation-Measuring System in unshielded environment based on low-T_C SQUID gradiometers

Clean room (number of particles/cu/t < 100)

- Foto lithography
- Wet chemical etching
- minimum lateral resolution: few micrometers

Shielded rooms

- Faraday room
- Magnetic shielded room

Radionuclide laboratory

- for handling of radioactive substances

Laboratory for cryogenic measurement of mechanical quality factors of gravitational wave detector components

- room temperature stability of ± 0.2 K at best
- vibration isolation (decoupled foundation)
- acoustic isolation
- remote controlled operation of the measurement equipment
- separated room for disturbing machines (e.g. pumps)
- full supply of technical media to perform cryogenic measurements

4. Current research projects

(A) Supported by the Bundesministerium für Bildung, Wissenschaft, Forschung und Technologie (BMBF), Bundesministerium für Wirtschaft und Arbeit (BMWi), and Bundesministerium für Umwelt, Naturschutz und Reaktorsicherheit (BMU)

Characterization of irradiated GaN and ZnO
Prof. Dr. W. Wesch, Prof. M. Hayes   39.6.L1A.6.B   01/04 – 06/07

ISOLDE: Aufbau einer neuen Instrumentierung zur elektrischen Charakterisierung von Störstellen in Halbleitern
Prof. Dr. W. Witthuhn   05KK4SJ1/4   07/04 – 12/07

Ioneninduzierte Strukturumbildungs- und Ausheilprozesse in Halbleitern
Teilprojekt 4 im Verbund Hochauflösende in-situ-Charakterisierung der Strukturumbildungsprozesse in Halbleitern
Verbund Forschung mit Sonden und Ionenstrahlen im Gesamtverbund Erforschung der kondensierten Materie mit Großgeräten
Prof. Dr. W. Wesch   05KK7SJ1   07/07 – 06/10

Computational Materials Science gestützte Optimierung des Wirkungsgrades von CIGS-Dünnschichtsolarzellen
Prof. Dr. W. Witthuhn, Prof. Dr. W. Wesch   0327665E   06/07 – 05/11

(B) Supported by the Deutsche Forschungsgemeinschaft (DFG)

Vertical, strained 1D silicon nanostructures and devices
Dr. E. Wendler   WE 1648/6-1   04/05 – 06/08

Strukturierungsverfahren für mikro- und nanooptische Elemente in Lithiumniobat
E.-B. Kley, F. Schrempel   KL 1199/2-1   05/07 – 04/09

Characterization of structural and optical properties of $Si_{1-x}Ge_x$ nanocrystals produced by laser-induced pyrolysis and by ion implantation
Prof. Dr. Fr. Huisken, Prof. Dr. W. Wesch   HU 474/19-1   09/07 – 08/09

Investigation of fast processes in condensed matter by time resolved X-ray diffraction
Dr. I. Uschmann (IOQ)   DFG US 17/3-1   10/02 – 04/07

Gütemessungen bei kryogenen Temperaturen
(Teilprojekt C 4 im SFB/TR 7 „Gravitationswellenastronomie")
Prof. Dr. P. Seidel, Dr. W. Vodel   DFG – SFB/TR7   01/03 – 12/10

Strukturbildung und Lokalisierung in nichtinstantanen Medien
Prof. W. Richter   RI 650/11-2   04/04 – 06/07

Spektroskopie von astrophysikalisch relevanten Molekülen in der Gasphase und in ultrakalten Helium-Tröpfchen
Prof. Dr. Fr. Huisken   HU 474/13-4   07/03 – 02/07

Gas phase studies of astrophysically relevant biomolecules
Prof. Dr. Fr. Huisken   HU 474/18-1   07/03 – 12/07

Silizium-Nanokristallite in Matrizen und ihre Beziehung zur Extended Red Emission
Prof. Dr. Fr. Huisken, Prof. Dr. W. Witthuhn   HU-474/16-2   07/03 – 01/07

(C)   Support by the EU

TARGET Top Amplifier Research Groups in a European Team
Prof. Dr. W. Richter   IST-1-507893-NOE   01/04 – 12/07

Biological diagnostic tools using microsystems and supersensitive magnetic detection (BIO-DIAGNOSTICS)
Prof. Dr. P. Seidel, Prof. Dr. J. Haueisen   EU (6. Rahmenprogramm)   11/05 – 10/08

(D)   Supported by the Thüringer Kultusministerium (TKM)

Ionenstrahlmodifikation und -analyse von Titanoberflächen
Prof. Dr. W. Wesch   02/9125 IBA Heiligenstadt   05/02 – 12/08

Dünnschicht Solarzellen der dritten Generation: transparente Dünnschicht Solarzellen/Tandem-Solarzellen
Prof. Dr. W. Witthuhn   B 515-06012   10/06 – 09/08

Heliumverflüssigungsanlage
Prof. P. Seidel   TKM   10/07 – 03/09

(E)   Supported by other institutions

Experimente zur Labor-Astrophysik
Prof. Dr. Fr. Huisken   MPI Heidelberg   01/02 – 05/12

CdTe-CdS-Dünnschichtsolarzellen
Prof. Dr. W. Witthuhn   ANTEC Solar   09/06 – 08/07

Defekte in Solarsilizium (Defis)
Prof. Dr. W. Witthuhn   CiS Institut für Mikrosensorik   09/06 – 12/07

Entwicklung, Aufbau und Erprobung eines schnellen DC-SQUID-Systems zur Messung von Dunkelströmen in supraleitenden Kavitäten für das TESLA-Projekt
Dr. W. Vodel   DESY Hamburg   04/01 – 12/08

STEP-Mission, F & E- Vorhaben mit dem ZARM Bremen
Dr. W. Vodel   ZARM Bremen   07/05 – 12/07

Zerstörungsfreie Strahldiagnose für Linear- und Ringbeschleuniger
Dr. W. Vodel   GSI Darmstadt   01/07 – 12/09

The experimental, analytical and numerical investigation of the current – voltage character-
istics of intrinsic Josephson junctions under microwave radiation
Prof. Dr. P. Seidel, Dr. Yu. M. Shukrinov   Heisenberg-Landau Programm   01/05 – 12/07

Elektronenspektroskopische Untersuchungen der Oberflächen von Laserbauteilen
Dr. B. Schröter   LASOS GmbH Jena   02/07 – 02/09

Analyse von Schichtsystemen mittels Auger-Elektronen-Spektroskopie
Dr. B. Schröter   TU Berlin   12/07 – 11/08

5. Publications

5.1 Publications in scientific journals

C. Blank, S. Krischok, R. Gutt, M. Engel, J.A. Schäfer, J. Schawohl, L. Spieß, Ch. Knedlik,
G. Ecke, F. Schrempel, E. Hüger, G. Hildebrand, K. Liefeith
Ion implanted titanium surfaces for hard tissue replacement
Biomaterialien 8 (4) (2007) 285-292.

S. Krischok, C. Blank, M. Engel, R. Gutt, G. Ecke, J. Schawohl, L. Spieß, F. Schrempel, G.
Hildebrand, K. Liefeith
Influence of ion implantation on titanium surfaces for medical applications
Surf. Sci. 601 (2007) 3856-3860.

F. Schrempel, Ch. Beeker, W. Wesch
Waveguide barriers with adjustable refractive index produced in KTP by irradiation with He-
and Li-ions
Nucl. Instr. and Methods B 257 (2007) 484-487.

V. Milinovic, N. Bibic, K.P. Lieb, M. Milosavljevic, F. Schrempel
Interface mixing of Fe/Si bilayers by noble-gas ions: Are there effects of the ionic charge-
state ?
Nucl. Instr. and Methods B 257 (2007) 605-608.

M. Katsikini, J. Arvanitidis, E.C. Paloura, S. Ves, E. Wendler, W. Wesch
Raman and X-ray absorption near-edge structure characterization of GaN implanted with O,
Ar, Xe, Te and Au
Opt. Mater. 29 (12) (2007) 1856-1860.

P.I. Gaiduk, S.L. Prokoph'ev, N.M. Kazuchits, V.I. Plebanovich, W. Wesch, A. Nylandsted
Larsen
Nano-cluster formation in Ge+Sn implanted SiO_2 layers
Nucl. Instr. and Methods B 257 (2007) 60-63.

O. Picht, W. Wesch, J. Biskupek, U. Kaiser, M.A. Oliveira, A. Neves, N.A. Sobolev
Ion beam synthesis of Mn/As-based clusters in silicon
Nucl. Instr. and Methods B 257 (2007) 90-93.

Th. Stelzner, G. Andrä, F. Falk, E. Wendler, W. Wesch, R. Scholz, S. Christiansen
Silicon nanowire synthesis on metal implanted silicon substrates
Nucl. Instr. and Methods B 257 (2007) 172-176.

W. Wesch, A. Kamarou, E. Wendler, A. Undisz, M. Rettenmayr
Effect of high electronic excitation in swift heavy ion irradiated semiconductors
Nucl. Instr. and Methods B 257 (2007) 283-286.

M. Hayes, F.D. Auret, P.J. Janse van Rensburg, J.M. Nel, W. Wesch, E. Wendler
Electrical characterization of H^+ ion irradiated n-ZnO
Nucl. Instr. and Methods B 257 (2007) 311-314.

M. Hayes, F.D. Auret, P.J. Janse van Rensburg, J.M. Nel, W. Wesch, E. Wendler
Electrical characterization of He^+ ion irradiated n-ZnO
Phys. Status Solidi B 244 (5) (2007) 1544-1548.

Z.S. Hussain, W. Wesch, E. Wendler, M.C. Ridgway
Amorphous phase formation in ion implanted $In_xGa_{1-x}As$
Nucl. Instr. and Methods B 257 (2007) 344-347.

E. Wendler, K. Gärtner, W. Wesch
Ion-beam induced effects at 15 K in MgO
Nucl. Instr. and Methods B 257 (2007) 488-491.

C.S. Schnohr, E. Wendler, W. Wesch
Room temperature annealing of low-temperature ion implanted sapphire
Nucl. Instr. and Methods B 257 (2007) 492-495.

N. Bibic, V. Milinovic, K.P. Lieb, M. Milosavljevic, F. Schrempel
Enhanced interface mixing of Fe/Si bilayers on preamorphized silicon substrates
Appl. Phys. Lett. (2007) 051901.

J. Eberhardt, H. Metzner, K. Schulz, U. Reislöhner, Th. Hahn, J. Cieslak, W. Witthuhn, R. Goldhahn, F. Hudert, J. Kräußlich
Excitonic luminescence of polycrystalline $CuInS_2$ solar cell material under the influence of strain
J. Appl. Phys. 102 (2007) 033503

J. Eberhardt, H. Metzner, R. Goldhahn, F. Hudert, K. Schulz, U. Reislöhner, Th. Hahn, J. Cieslak, W. Witthuhn
Optical properties of strained polycrystalline $CuInS_2$ layers
Mater. Res. Soc. Symp. Proc. 1012 (2007) 419

M. Hädrich, S. Mack, H. Metzner, U. Reislöhner, W. Witthuhn
Influence of deposition parameters on the morphology of CdTe films and on the performance of CdTe solar cells
Mater. Res. Soc. Symp. Proc. 1012 (2007) 407

J. Cieslak, Th. Hahn, H. Metzner, J. Eberhardt, W. Witthuhn, J. Kräußlich, F. Wunderlich
Epitaxial CuIn$_{1-x}$Ga$_x$S$_2$ on Si(111) (0 ≤ x ≤ 1): Lattice match and Metastability
Phys. Rev. B 75 (2007) 245306

M. Hädrich, N. Lorenz, H. Metzner, U. Reislöhner, S. Mack, M. Gossla, W. Witthuhn
CdTe-CdS solar cells – Production in a new baseline and investigation of material properties
Thin Solid Films 515 (2007) 5804

U. Reislöhner, M. Hädrich, N. Lorenz, H. Metzner, W. Witthuhn
Doping profiles in CdTe/CdS thin film solar cells
Thin Solid Films 515 (2007) 6175

J. Eberhardt, K. Schulz, H. Metzner, J. Cieslak, Th. Hahn, U. Reislöhner, M. Gossla, F. Hudert, R. Goldhahn, W. Witthuhn
Epitaxial and polycrystalline CuInS$_2$ thin films: a comparison of opto-electronical properties
Thin Solid Films 515 (2007) 6147

M. Moenster, U. Griebner, W. Richter, G. Steinmeyer
Resonant Saturable Absorber Mirrors for Dispersion Control in Ultrafast Lasers
IEEE J. of Quantumelectronics **43** (2007) 147

D. Nodop, J. Limpert, R. Hohmuth, W. Richter, M. Guina, and A. Tünnermann
High-pulse-energy passively Q-switched quasi-monolithic microchip lasers operating in the sub-100-ps pulse regime
Optics Letters 32 (2007) 2115

R. Nawrodt, A. Zimmer, T. Koettig, S. Nietzsche, M. Thürk, W. Vodel, P. Seidel
High Mechanical Q-Factor Measurements on Calcium Fluoride at Cryogenic Temperatures
Phys. J. Appl. Phys. 38 (2007) 53-59

W. Vodel, R. Neubert, S. Nietzsche, K. Knaack, K. Wittenburg, A. Peters
LTS-SQUID based measurement tool for characterization of superconductive RF cavities
IEEE Transactions on Applied Superconductivity 17 (2007) 621-624

F. Schmidl, P. Weber, T. Koettig,, M. Büttner, S. Prass, Ch. Becker, M. Mans, J. Heinrich, M. Röder, K. Wagner, D.V. Berkov, P. Görnert, G. Glöckl, W. Weitschies, P. Seidel
Characterization of energy barrier and particle size distribution of lyophilized ferrofluids by magnetic relaxation measurements
Journal of Magnetism and Magnetic Materials 311 (2007) 171-175

V. Grosse, R. Bechstein, F. Schmidl, P. Seidel
Conductivity and dielectric properties of thin amorhous cerium dioxide films
J. Phys. D: Appl. Phys. 40 (2007) 1-5

Yu. M. Shukrinov, M. Mans, J. Scherbel, P. Seidel
The influence of microwave irradiation power on current-voltage characteristics of intrinsic Josephson junctions
Supercond. Sci. Technol. 20 (2007) 74-78

E. Romanus, T. Koettig, G. Glöckl, S. Prass, F. Schmidl, J. Heinrich, M. Gopinadhan, D.V. Berkov, C.A. Helm, W. Weitschies, P. Weber, P. Seidel
Energy barrier distributions of maghemite nanoparticles
Nanotechnology 18 (2007) 115709 (8pp)

T. Koettig, S. Moldenhauer, M. Matze, M.Thürk, P. Seidel
Investigation on the internal thermal link of pulse tube refrigerators
Cryogenics 47 (2007) 137 – 142

A. Zimmer, R. Nawrodt, T. Koettig, R. Neubert, M. Thürk, W. Vodel, P. Seidel
Cryogenic resonant acoustic spectroscopy of bulk materials (CRA spectroscopy)
Scientific Instruments 78 (2007) 063905-1

R. Nawrodt, A. Zimmer, A., T. Koettig, T. Clausnitzer, A. Bunkowski, E.B. Kley, R. Schnabel, K. Danzmann, S. Nietzsche, W. Vodel, A. Tünnermann, P. Seidel
Mechanical Q-factor measurements on a test mass with a structured surface
New Journal of Physics 9 (2007)**,** 225

P. Seidel, T. Foerster, H. Schneidewind, C. Becker, V. Grosse, A. Steppke, P. Lorenz, R. Pietzcker, F. Schmidl
Comparsion of High Temperature Superconducting Gradiometers Using Flip Chip YBCO and TBCCO Antennas
IEEE Trans. Appl. Supercond. 17 (2007) 668-671

T. Koettig, R. Nawrodt, M. Thürk, P. Seidel
Performance Characteristic of a Two-Stage Pulse Tube Refrigerator in Coaxial Configuration
Cryocoolers 14 (2007) 171 – 176

P. Seidel, C. Becker, A. Steppke, M. Buettner, H. Schneidewind, V. Grosse, G. Zieger, F. Schmidl
Long-time stable high-temperature superconducting DC-SQUID gradiometers with silicon dioxide passivation for measurements with superconducting flux transformers
Supercond. Sci. Technol. 20 (2007) 380–384

W. Vodel, R. Neubert, S. Nietzsche, P. Seidel, K. Knaack, K. Wittenburg, A. Peters
A new measurement tool for characterization of superconducting rf accelerator cavities using high-performance LTS SQUIDs
Supercond. Sci. Technol. 20 (2007) 393–397

D. Heinert, A. Zimmer, R. Nawrodt, T. Köttig, C. Schwarz, M. Hudl, W. Vodel, A. Tünner-mann, P. Seidel
High-sensitivity tool for studying phonon related mechanical losses in low loss materials
Journal of Physics: Conference Series 92 (2007) 012183

A. Zimmer, R. Nawrodt, D. Heinert, C. Schwarz, M. Hudl, T. Köttig, W. Vodel, A. Tünnermann, P. Seidel
Mechanical losses in low loss materials studied by Cryogenic Resonant Acustic spectroscopy of bulk materials (CRA spectroscopy)
Journal of Physics: Conference Series 92 (2007) 012195

G. Rouillé, M. Arold, A. Staicu, S. Krasnokutski, F. Huisken, Th. Henning, X.-F. Tan, and F. Salama
$S_1(^1A_1) \leftarrow S_0(^1A_1)$ *transition of benzo[g,h,i]perylene in supersonic jets and rare gas matrices*
J. Chem. Phys. **126**, 174311 (2007)

R. Alexandrescu, I. Morjan, F. Dumitrache, R. Birjega, C. Jaeger, H. Mutschke, I. Soare, L. Gavrila-Florescu, and V. Ciupina
Structural characteristics of Fe_3C-based nanomaterials prepared by laser pyrolysis from different gas-phase precursors
Materials Science and Engineering C **27**, 1181–1184 (2007)

I. Llamas-Jansa, C. Jäger, H. Mutschke, and Th. Henning
Far-ultraviolet to near-infrared optical properties of carbon nanoparticles produced by pulsed-laser pyrolysis of hydrocarbons and their relation with structured variations
Carbon **45**, 1542-1557 (2007)

C. Jäger, F. Huisken, H. Mutschke, Th. Henning, B. Poppitz, and I. Voicu
Identification and spectral properties of PAHs in carbonaceous material produced by laser pyrolysis
Carbon **45**, 2981-2994 (2007)

5.2 Conference contributions

Int. School on Structural Characterization of nanostructures, Aveiro, Portugal, January 25 - 27, 2007

N.M. Santos, N.A. Sobolev, J.P. Leitao, M.C. Carmo, D. Fuster, L. Gonzalez, Y. Gonzalez, W. Wesch
Influence of proton irradiation on the photoluminescence of InAs/InP quantum wires

Frühjahrstagung der DPG, Regensburg, March 26 - 30, 2007

C. Becker, A. Steppke, V. Grosse, H. Schneidewind, L. Redlich, F. Schmidl, P. Seidel
Untersuchung von planaren HTSL Flip-Chip DC-SQUID Gradiometern

M. Büenfeld, B. Schröter, F. Schmidl, M. Grube, R. Geithner, T. Pertsch, D. Schelle, W. Richter, A. Tünnermann, P. Seidel
Strukturierte Schichtsysteme für horizontal gerichtetes Wachstum von Kohlenstoff-Nanoröhren

F. Schmidl, M. Büttner, T. Müller, S. Prass, P. Weber, A. Steppke, C. Becker, P. Seidel
Investigation of magnetic nanoparticles by temperatur dependent relaxation measurements

S. Hechler , R. Nawrodt , W. Vodel , J. Dittus , F. Löffler, P. Seidel
Characterization of 3-dimensional superconductive thin film components for experiments in space (Poster)

D. Heinert , R. Nawrodt, A. Zimmer, W. Vodel , A. Tünnermann, P. Seidel
Analysis of mechanical loss processes for gravitational wave detectors (Poster)

C. Schwarz, R. Nawrodt, A. Zimmer, W. Vodel, A. Tünnermann, P. Seidel, S. Nietzsche,
Mechanical Loss Measurements on Calcium Fluoride Bulk Material at Low Temperatures (Poster)

A. Zimmer, R. Nawrodt, D. Heinert, C. Schwarz, M. Hudl, W. Vodel, A. Tünnermann, P. Seidel
Relaxion mechanisms in low mechanical loss materials for interferometric gravitational wave detectors occurring a lot low temperatures

M. Büttner, F. Schmidl, T. Müller, S. Prass, M. Mans, C. Becker, D. Berkov, P. Seidel
Temperaturabhängige Magnetrelaxometrie an magnetischen Nanopartikeln im Temperaturbereich von 4 K bis 325 K

R. Geithner, H. Mühlig, M. Büenfeld, M. Grube, F. Schmidl, B. Schröter, W. Richter, P. Seidel
Elektrische Messungen an Kohlenstoff-Nanoröhren

R. Pietzcker, V. Grosse, G. Zieger, F. Schmidl, P. Seidel
Herstellung mittels PLD und Charakterisierung der kristallographischen Eigenschaften von ZnO/YBa2Cu3O7-x-Schichtsystemen

A. Steppke, M. Djupmyr, P. Rudo, C. Becker, V. Grosse, J. Albrecht, F Schmidl
Characterisation of new high-Tc superconducting dc-SQUID-gradiometers for spatial resolved measurements (Poster and post-deadline talk)

R. Pietzcker, V. Grosse, G. Zieger, F. Schmidl, P. Seidel
Crystallographic characterization of pulsed-laser-deposited $ZnO/YBa_2Cu_3O_{7-x}$ bilayers (Poster)

M. Grube, M. Büenfeld, F. Schmidl, P. Seidel
Herstellung und Vermessung von Kobalt-Clustern (Poster)

A.-K. Nix, S. Müller, C. Ronning, H. Hofsäß, C. Trautmann, A. Kamarou, E. Wendler, W. Wesch
Annealing of implantation defects in GaN by swift heavy ion irradiation

R. Volkmer, A. Hartung, B. Schröter
Growth and characterization of carbon nanotubes on silicon carbide

T. Reichel, M. Steglich, B. Schröter
The growth of carbon nanotubes on prestructured substrates by chemical vapor deposition

MRS Spring meeting, San Francisco, USA, April 09 - 13, 2007

J. Eberhardt, H. Metzner, R. Goldhahn, F. Hudert, K. Schulz, U. Reislöhner, Th. Hahn, J. Cieslak, W. Witthuhn
Optical properties of strained polycrystalline CuInS$_2$ layers

M. Hädrich, S. Mack, H. Metzner, U. Reislöhner, W. Witthuhn
Influence of Deposition Parameters on the Morphology of CdTe Films and on the Performance of CdTe Solar Cells

DIPAC 2007, Mestre, Italy, May 20 - 23, 2007

W. Vodel, R. Neubert, S. Nietzsche, K. Knaack, M. Wendt, K. Wittenburg, A. Peters
Current Status of the SQUID Based Cryogenic Current Comparator for Absolute Measurements of the Dark current of Superconducting RF Accelerator Cavities (Poster)

E-MRS 2007 Spring Meeting, Strasbourg, France, May 28 - June 01, 2007

N.M. Santos, N.A. Sobolev, J.P. Leitao, M.C. Carmo, D. Fuster, L. Gonzalez, Y. Gonzalez, W. Wesch
Enhanced radiation hardness of InAs/InP quantum wires

11th International Superconductive Electronics Conference, Washington D.C., USA, June 10 - 14, 2007 (ISEC 2007)

P. Seidel, C. Becker, A. Steppke, T. Grumpelt, H. Schneidewind, V. Große, G. Zieger, F. Schmidl
Long-timestable HTSC DC-SQUID gradiometer with silicons dioxide passivation

W. Vodel, R. Neubert, S. Nietzsche, P. Seidel, K. Knaack, K. Wittenburg, and A. Peters
A new measurement tool for characterization of superconducting RF accelerator cavities using high performance LTS SQUIDs

13th Int. Conf. on Surface Science (ICSS-13); Int. Conf. on Nano Science and Technology (ICN+T 2007), Stockholm, Sweden, July 02 - 06, 2007

M. Hayes, F. Schrempel, D. Auret, J. Nel, S. Coelho
RBS investigation of annealed thin gold layers on crystalline germanium

7th Edoardo Amaldi Conference on Gravitational Waves, Sydney, Australia, July 08 - 14, 2007

R. Nawrodt, A. Zimmer, T. Koettig, C. Schwarz, D. Heinert, M. Hudl, R. Neubert, M. Thürk, S. Nietzsche, W. Vodel, A. Tünnermann, P. Seidel
High mechanical Q-factor measurements on silicon bulk samples

I.W. Martin, R. Nawrodt, H. Armandula, C. Comtet, M.M. Fejer, A. Gretarsson, G. Harry, J. Hough, J.-M. Mackowski, N. Morgado, S. Penn, S. Reid, A. Remillieux, R. Route, S. Rowan, C. Schwarz, P. Seidel, W. Vodel, S. Zappe, A. Zimmer
Measurements of the temperature dependence of the mechanical loss of single layers of ion beam sputtered doped tantala and silica coatings on thin silicon substrates

12th International Conference on Phonon Scattering in Condensed Matter, Paris, France, July 15 - 20, 2007 (PHONONS 2007)

A. Zimmer, R. Nawrodt, D. Heinert, C. Schwarz, M. Hudl, T. Koettig, W. Vodel, A. Tuennermann, P. Seidel
Mechanical Losses in Low Loss Materials Studied by Cryogenic Resonant Acoustic Spectroscopy of Bulk materials (CRASB)

D. Heinert, A. Zimmer, R. Nawrodt, T. Koettig, C. Schwarz, M. Hudl, W. Vodel, A. Tuennermann, P. Seidel (Poster)
High-sensitivity Tool for Studying Phonon Related Mechanical Losses in Low Loss Materials

11th International Conference on Magnetic Fluids, Košice, Slovakia, July 23 - 27, 2007 (ICMF 2007)

M. Bütter
Magnetic properties of magnetosomes

14th Int. Conf. on Radiation Effects in Insulators (REI-14), Caen, France, August 28 to September 01, 2007

F. Schrempel, T. Steinbach, Th. Gischkat, W. Wesch
Channelling irradiation of $LiNbO_3$

Th. Gischkat, F. Schrempel, W. Wesch
Ion beam induced effects at 15 K in $LiNbO_3$

W. Wesch, E. Wendler, K. Gärtner
Comparison of ion-induced damage formation in (110) and (100) MgO

8th European Conference on Applied Superconductivity, Brussels, Belgium, September 16 - 20, 2007 (EUCAS 07)

C. Becker, A. Steppke, T. Köttig, J. Gerster, L. Dörrer, F. Schmidl, P. Seidel
Operation of a high-T_c DC-SQUID gradiometer on a non-metallic Pulse-Tube Refrigerator

European Workshop NanoLum VII, Jena, November 05 - 06, 2007

Organized by Friedrich Huisken

52nd Conf. on Magnetism and Magnetic Materials, Tampa, Florida, USA, November 05 to 09, 2007

N.A. Sobolev, M.A. Oloveira, A.J. Neves, A.O Ankiewicz, R.M. Rubinger, M.C. Carmo, O. Picht, W. Wesch, R.P. Borges, M. Godinho, J. Biskupek, U. Kaiser, W. Gehlhoff
Magnetic and structural properties of Mn and As implanted silicon

1. Photovoltaik-Symposium, Bitterfeld-Wolfen, November 15 - 16, 2007

J. Eberhardt, H. Metzner, R. Goldhahn, F. Hudert, K. Schulz, U. Reislöhner, Th. Hahn, J. Cieslak, W. Witthuhn
Optische Eigenschaften von verspannten CuInS$_2$-Schichten

WE-Heraeus-Seminar on "Photon Management in Solar Cells", Bad Honnef, October 29 - November 01, 2007

M. Hädrich, S. Mack, H. Metzner, U. Reislöhner, W. Witthuhn
Morphology of CdTe thin films for solar cell application

2nd Workshop on ab-initio phonon calculations, Krakau, Poland, December 06 - 08, 2007

D. Heinert, C. Schwarz, A. Schroeter, R. Nawrodt, R. Neubert, M. Thürk, W. Vodel, A. Tünnermann, P. Seidel
Mechanical spectroscopy of low loss materials at cryogenic temperatures (Poster)

5.3 Theses

Diploma Theses

Daniel Heinert	*Mechanische Verluste in Festkörpern*
Stefan Hechler	*Charaktersierung supraleitender Komponenten für Gravitationsexperimente*
Matthias Hudl	*Untersuchung von mechanischen Dämpfungsvorgängen in dielektrischen Schichten*
Christian Schwarz	*Kryogene Gütemessung an optischen Substraten für Gravitationswellendetektoren*
Gabriel Zieger	*Herstellung und Charakterisierung dünner epitaktischer CeO$_x$-Schichten*
Alexander Steppke	*HTSL-SQUIDs für den Nachweis von magnetischen Nanoteilchen*
Robert Pietzcker	*Herstellung und Untersuchung von Zinkoxid-Schichten mittels Laserdeposition*

Thomas Müller	*Untersuchung magnetischer Nanopartikel (MNP) mittels optischer und magnetischer Methoden*
Rene Geithner	*Elektrische Untersuchungen an nanostrukturierten Bauelementen*
Matthias Grube	*Herstellung und Charakterisierung von Kontakt- und Katalysatorschichten für Kohlenstoff-Nanoröhren*
Matthias Schmelz	*Entwicklung tantalbasierter Schichtsysteme für die bolometrische Detektion von Röntgenspektren* (extern)
Michael Steinert	*Formierung von Compound-Nanoclustern in Silizium durch Ionenstrahlen*
Annett Schroeter	*Vergleichende Untersuchungen zur Defektbildung bei Ionenimplantation von Silizium und Germanium*
Tobias Steinbach	*Untersuchungen zur Defektbildung in Lithiumniobat bei Ionenbestrahlung in Kanalisierungsrichtung*
Tina Clauß	*Molekulardynamik (MD)-Simulationen zu ionenstrahlinduzierter Defektakkumulation in Silizium*
Christian Weidemann	*Messung der chemischen Verschiebung von $K\alpha$- und $K\beta$-Übergängen in Mangan* (extern)
Christian Kraft	*Untersuchung an CdTe-Dünnschichtsolarzellen mit unterschiedlichen transparenten Frontkontakten*
Michael Oertel	*Entwicklung eines sequentiellen Prozesses zur Herstellung von Cu-InSe$_2$-Dünnschichtsolarzellen*
Christiane Löffler	*Herstellung von CdS/CdTe-Heterosolarzellen ohne nasschemische Prozessschritte*
Matthias Steglich	*Herstellung von Kohlenstoffnanoröhren mittels Gasverfahren (CVD) und Charakterisierung der Eigenschaften und Wachstumsprozesse*
Alexander Hartung	*Untersuchungen zum Wachstum von Kohlenstoff-Nanostrukturen in einer Molekularstrahl-Anlage*
Reinhard Volkmer	*Wachstum und Analyse von Kohlenstoffnanoröhren und Graphene-Schichten auf Siliziumkarbid*

PhD-Theses

Janko Cieslak	*Epitaxie von Cu(In,Ga)S$_2$ auf Si-Substraten*
Jens Eberhardt	*Photolumineszenz epitaktischer und polykristalliner CuInS$_2$-Schichten für Dünnschichtsolarzellen*

Kerstin Riedel   Methoden zur Untersuchung biologischer Moleküle mittels Festkörper-Kernresonanzspektroskopie (extern)

Examenspreis 2007 der Friedrich-Schiller-Universität

André Hedler
Plastische Deformation von amorphem Silizium unter Hochenergie-Schwerionenbestrahlung

5.4 Invited talks and colloquia

W. Wesch
Ion beam synthesis of nanoclusters in semiconductors
Universität Aveiro, Aveiro, Portugal, January 22, 2007

F. Schrempel
Strukturierungsverfahren für mikro- und nano-optische Elemente in Lithiumniobat
Ehrenkolloquium im IFK, April 27, 2007

W. Vodel
Superconductivity - Basics and Applications in High Precision Measurements
4th German Vietnam Summer School, Hanoi and Ho Chi Minh City, September 10 - 25, 2007

W. Wesch
Swift heavy ion irradiation of amorphous silicon and germanium
Australian National University, Department of Electronic Materials and Engineering, Canberra, Australia, October 05, 2007

F. Schrempel
Strukturierungsverfahren für mikro- und nanooptische Elemente in Lithiumniobat
Universität Göttingen, II. Physikalisches Institut, November 02, 2007

Th. Hahn
Manufacturing Processes for CIGS
Kick-Off-Meeting Projekt ComCIGS, IBM Deutschland Mainz, December 13, 2007

6.   Cooperations, guests and colloquia at IFK

The Institute of Solid State Physics collaborates with a large number of Institutes and Universities in Germany and around the world and has also close connections with several companies. In the framework of these wide spread contacts in 2007 a number of scientists from various countries visited our Institute to perform experiments, discuss scientific results obtained within joint projects and to give talks in the colloquium of the Institute of Solid State Physics.

6.1   Visiting scientists

Prof. Dr. R. Alexandrescu	Institute of Laser, Plasma and Radiation Physics, Bukarest, Romania
Prof. E. Alves	Departamento de Fisica, Instituto Tecnologico e Nuclear, Sacavem, Portugal
Dr. Geppo Cagnoli	Universität Glasgow
Elisabetta Cesarini	Universität Florenz
Maxim Chukharkin	Moskauer Staatliche Universität
Dr. A. Chuvilin	Institute of Catalysis, Novosibirsk, Russia
Prof. Dr. Jan Fulara	Polish Academy of Sciences, Warszawa, Poland
Prof. P.I. Gaiduk	Faculty of Radiophysics and Electronics, State University of Belarus, Minsk, Belarus
Dr. Federico Garrido	Centre de Spectrometrie Nucleare et de Spectrometrie de Masse, Orsay, France
Prof. Ya. Greenberg	Staatl. Techn. Univ. Novosibirsk, Russia
Dr. A. Gryb	Staatliche Universität Kharkov, Ukraine
Dr. Olivier Guillois	Laboratoire Francis Perrin, CEA Saclay, Gif-sur-Yvette, France
Prof. Dr. M. Hayes	University of Pretoria, Physics Department, South Africa
Prof. Jim Hough	Universität Glasgow
Dr. Yong Gwan Kang	Kim II Sung University Pyongyang, Nordkorea
Dr. Y.-S. Kim	Korea Institute of Geology, Mining and Materials, Taejon, Korea
Dr. Istvan Kovacs	Research Institute for Technical Physics and Material Science Budapest, Hungary
Prof. Dr. Jacek Krelowski	University of Torun, Poland
Dr. Gilles Ledoux	Université Claude Bernard, Lyon, France
Iain Martin	Institute of Gravitational Research IGR, Glasgow, UK
Dr. Cécile Reynaud	Laboratoire Francis Perrin, CEA Saclay, France
Prof. Dr. N. A. Sobolev	Departamento de Fisica, Universidade de Aveiro, Aveiro, Portugal
Dr. Yuri M. Shukrinov	Joint Institute for Nuclear Research Dubna, Bogoliubov Laboratory of Theoretical Physics, Russia

6.2 Colloquia at the Institute of Solid State Physics

Dr. Heinz Hilgers
Nanotechnologie in Deutschland
PHOTONS European Photovoltaics AG in Mainz, 19. Januar 2007

Dr. Nethaji Dharmarasu
Irradiation induced effects in high efficiency III-V solar cells and materials
Universität Kassel, FB Technische Elektronik, 26. Januar 2007

Prof. Dr. Paul Seidel
Beispiele aus der Angewandten Tieftemperaturphysik
Friedrich-Schiller-Universität Jena, AG Tieftemperaturphysik, 20. April 2007

Prof. Dr. Hans Hofsäss
Mit Ionenstrahlen die Nanowelt gestalten
Universität Göttingen, II. Physikalisches Institut, 27. April 2007

Kirsten Gerth
Relevante Quellen für Fachinformationen und bibliometrische Analysen
ThULB der Friedrich.-Schiller-Universität Jena, 04. Mai 2007

Dr. Yong Gwan Kang
Arbeitsgruppe Tieftemperaturphysik der Kim Il Sung Universität
Kim Il Sung Universität, Pyongyang, Korea DVR, 11. Mai 2007

Dr. Heinrich Metzner-Fraune
Das SolarZentrum Erfurt
CiS Erfurt, Institut für Mikrosensorik, 01. Juni 2007

Prof. Dr. Werner Wesch
Festkörperforschung mit Ionenstrahlen
Friedrich-Schiller-Universität Jena, AG Ionenstrahlphysik, 08. Juni 2007

Dr. K. Potzger
Magnetic semiconductors created by non-equilibrium processes - new challenges for ion beams
FZ Rossendorf-Dresden, 22. June 2007

Dr. Aimo Winkelmann
Spinaufgelöste Mehrphotonen-Photoemission
Max-Planck-Institut Halle, 29. Juni 2007

Dr. Bernd Schröter
Wachstum und Charakterisierung von Kohlenstoff-Nanostrukturen
Friedrich-Schiller-Universität Jena, AG Physik dünner Schichten, 06. Juli 2007

Torsten Schmidt
Silizium-Nanoteilchen in biologischen Anwendungen
Friedrich-Schiller-Universität Jena, AG Laborastrophysik, 13. Juli 2007

Dr. Joachim Bollmann
Alkali und Erdalkali - korrelierte Defekte in Silizium
TU Bergakademie Freiberg, 20. Juli 2007

Ronny Nawrodt
Kryogene Gütemessungen
Friedrich-Schiller-Universität Jena, AG Tieftemperaturphysik, 09. November 2007

Prof. Günther Schatz
Hyperfeinwechselwirkungen - Erinnerungen eines Weggefährten
Universität Konstanz, 16. November 2007

PD Dr. Heiner Metzner-Fraune
10 Jahre Photovoltaik am IFK
Friedrich-Schiller-Universität Jena, AG CISLAB, 16. November 2007

Dr. Guido Fuchs
Komplexe Molekülbildung auf Oberflächen kryogener Festkörper und deren astrophysikalische Bedeutung
Leiden Observatory, NL und Wiley-VCH, Berlin, 30. November 2007

Prof. Dr. Ute Kaiser
Eine kurze Geschichte der Dünnschicht - Elektronensubnanoskopie
Universität Ulm, 14. Dezember 2007

7.   Teaching activities

7.1   Lectures

Experimentalphysik I   Prof. Dr. P. Seidel
WS 2006/2007, SS 2007, WS 2007/08

Kursvorlesung Physik der Materie I   Prof. Dr. W. Wesch
WS 2006/2007, WS 2007/2008

Experimentalphysik II Grundkurs Elektrizität, Optik   Prof. Dr. W. Witthuhn
WS 2006/2007

Kursvorlesung Physik für Nebenfach-Studenten   Prof. Dr. W. Wesch
(Biologen,Ernährungswissenschaftler, Pharmazie, Biogeo)
WS 2006/2007, WS 2007/2008

Experimentalphysik für Mediziner und Biochemiker   Prof. Dr. W. Richter
WS 2005/2006, SS 2006, WS 2006/2007

Kursvorlesung Kerne und Teilchen   Prof. Dr. W. Wesch
SS 2007

Elektronik WS 2006/2007, SS 2007, WS 2007/2008	PD Dr. F. Schmidl, Dr. W. Vodel
Einführung in die Festkörperphysik WS 2006/2007	Prof. Dr. P. Seidel PD Dr. F. Schmidl
Experimentalphysik IV: Struktur der Materie II (Physik-Diplom, Physik-Lehramt) SS 2007 (Wahlpflichtvorlesung)	Prof. Dr. P. Seidel
Dünnschichtphysik II WS 2006/2007	Prof. Dr. P. Seidel
Tieftemperaturphysik- und -technik SS 2007	Prof. Dr. P. Seidel Dipl.-Ing. M. Thürk
Grundkurs Physik der Materie II WS 2007/08	Prof. Dr. P. Seidel
Supraleitung WS 2007/2008	Prof. Dr. P. Seidel, Dr. J. Albrecht (MPI Stuttgart)
Ergänzende Kapitel der Festkörperphysik WS 2007/08 (Wahlpflichtvorlesung)	PD Dr. F. Schmidl
Ausgewählte Kapitel der Quantentheorie WS 2006/2007	PD Dr. K. Gärtner
Festkörperanalyse mit energiereichen Teilchen WS 2007/2008 (Wahlvorlesung)	Prof. Dr. W. Wesch, PD Dr. K. Gärtner, Dr. F. Schrempel
Grundlagen des Quantum Computing WS 2006/2007	PD Dr. W. Krech
Experimentalphyxsik für Mediziner, Biochemiker WS 2006/2007, SS 2007, WS 2007/2008	Prof. Dr. W. Richter
Kern- und Elementarteilchenphysik SS 2007	Prof. Dr. W. Richter
Halbleiterphysik SS 2007	Prof. Dr. W. Richter
Halbleiter-Optoelektronik, WS 2006/2007, WS 2007/08	Prof. Dr. W. Richter
Schicht- und Oberflächenanalyse (FH Jena) WS 2006/2007	Prof. Dr. W. Richter

| Nanophysik I: Cluster | Prof. Dr. Fr. Huisken |
| WS 2006/2007 | |

Cluster und Nanoteilchen II   Prof. Dr. Fr. Huisken
SS 2007

Labor-Astrophysik   Prof. Dr. Fr. Huisken,
WS 2006/2007   Dr. H. Mutschke

Solarzellen- Grundlagen und Materialaspekte   PD Dr. H. Metzner
WS 2007/2008

Oberflächenanalyse (an der FH Jena)   Dr. B. Schröter
WS 2006/2007

7.2   Seminars

Physik der Materie I   PD Dr. E. Wendler
SS 2007

Physik der Materie I   PD Dr. K. Gärtner
WS 2006/2007, WS 2007/2008

Kerne und Teilchen   PD Dr. K. Gärtner
SS 2007

Experimentalphysik I für Physiker   Dr. Ch. Hülsen
WS 2006/2007, SS 2007, WS 2007/2008

Experimentalphysik I für Physiker   PD Dr. E. Wendler
SS 2007

Experimentalphysik II für Physiker   PD Dr. E. Wendler
WS 2006/2007, SS 2007, WS 2007/2008

Physik für Biogewissenschaftler   PD Dr. E. Wendler
WS 2006/2007, WS 2007/2008

Experimentalphysik II: Grundkurs Elektrizität, Optik   Dr. F. Schrempel
WS 2006/2007

Elektronik   Dr. W. Vodel,
WS 2006/2007, SS 2007, WS 2007/2008   PD Dr. F. Schmidl
(Physik-Diplom und Informatik)

Elektronik (Lehramtsstudenten)   Dr. W. Vodel
WS 2006/2007, SS 2007, WS 2007/2008

Einführung in die Festkörperphysik
WS 2006/2007, WS 2007/2008

PD Dr. F. Schmidl,
Dipl.-Ing. M. Büttner

Tieftemperaturphysik und Supraleitung
WS 2006/2007, SS 2007, WS 2007/2008

Prof. Dr. P. Seidel

Ergänzende Kapitel der Festkörperphysik
Materialwissenschaftler 5. Semester
WS 2007/2008 (Wahlpflichtseminar)

PD Dr. F. Schmidl,
Dipl.-Ing. M. Büttner

Supraleitung
WS 2007/2008 (Wahlseminar)

Dipl.-Phys. R. Geithner,
Dipl.-Phys. A. Steppke

Grundkurs Physik der Materie II
SS 2007, WS 2007/2008

PD D. Schmidl

Institutsseminar
WS 2006/2007, SS 2007

Prof. Dr. W. Witthuhn

Institutsseminar
WS 2007/2008

Prof. Dr. P. Seidel

Nukleare Festkörperphysik
WS 2006/2007, SS 2007, WS 2007/2008

Prof. Dr. W. Wesch

Physik dünner Schichten
WS 2006/2007, SS 2007, WS 2007/2008

Prof. Dr. W. Richter

Kern- und Elementarteilchenphysik
SS 2007

Prof. Dr. W. Richter

Proseminar zum Fortgeschrittenenpraktikum
WS 2006/2007, SS 2007, WS 2007/2008

Prof. Dr. W. Witthuhn,
Dr. B. Schröter

7.3 Practica

Grundpraktikum
WS 2006/2007, SS 2007, WS 2007/2008

Prof. Dr. W. Wesch,
Dr. K. Gärtner ,
Dr. Th. Hahn,
S. Mack, M. Oertel

Fortgeschrittenen-Praktikum
WS 2006/07, SS 2007

Prof. Dr. W. Witthuhn (Leitung)

Fortgeschrittenen-Praktikum
WS 2007/2008

Dr. B. Schröter (Leitung),
Dipl.-Ing. M. Thürk,
Dipl.-Phys. M. Büenfeld,
Dipl.-Phys. R. Nawrodt

F-Praktikum (Kernphysik)
WS 2006/2007, SS 2007, WS 2007/2008

Dr. U. Reislöhner,
Dr. F. Schrempel

Elektronikpraktikum
WS 2006/2007, SS 2007, WS 2007/2008

Dr. W. Vodel (Leitung),
PD Dr. F. Schmidl,
Dipl.-Phys. R. Nawrodt,
Dipl.-Phys. F. Perner,
Dipl.-Ing. R. Neubert,
Dipl.-Ing. Mühlig,
Dipl.-Phys. V. Große

Messtechnik
WS 2006/2007, SS 2007, WS 2007/2008

PD Dr. F. Schmidl,
Dipl.-Ing. R. Neubert,
Dipl.-Ing. H. Mühlig,
Dipl.-Phys. V. Große,
Dipl.-Phys. Ch. Becker,
Dipl.-Phys. A. Steppke,
Dipl.-Phys. R. Geithner

Weihnachtsvorlesung
WS 2006/2007, WS 2007/2008

Prof. Dr. P. Seidel,
Prof. Dr. W. Wesch

8.   Personnel

Professors

Prof. Dr. habil. Wolfgang Witthuhn (to 09/07)
Prof. Dr. habil. Wolfgang Richter
Prof. Dr. habil. Paul Seidel (director)
Prof. Dr. habil. Werner Wesch
Prof. Dr. habil. Friedrich Huisken

Scientific Staff

PD Dr. habil. Konrad Gärtner	Dr. Christian Hülsen
PD Dr. habil. Heinrich Metzner	Dr. Cornelia Jäger
PD Dr. habil Frank Schmidl	Dr. Sandor Nietzsche
PD Dr. habil. Elke Wendler	Dr. Udo Reislöhner
Dr. J. Cieslak	Dr. Gaël Rouillé
Dr. Jens Eberhardt	Dr. Frank Schrempel
Dr. Olivier Debieu	Dr. Bernd Schröter
Dr. Ernst Glaser	Dr. Thomas Stelzner (to 03/07)
Dr. Thomas Hahn	Dr. Wolfgang Vodel

PhD Students

Marco Arold	Andrey Kamarou (to 02/07)
Daniel Baumgarten (Biomagn. Zentrum)	Torsten Köttig
Christoph Becker	Mario Liehr (Biomagn. Zentrum)
Matthias Büenfeld (to 12/07)	Sebastian Mack (to 12/07)
Markus Büttner	Michael Mans
Janko Cieslak (to 05/07)	Ronny Nawrodt
Jens Eberhardt	Katja Peiselt (IPHT Jena)
Rene Geithner (from 06/07)	Jakob Reinisch (from 08/07)
Thomas Gischkat	Kerstin Riedel (Fritz-Lipmann Institut)
Veit Große	Christian Schwarz (from 11/07)
Mathias Hädrich	Alexander Steppke (from 06/07)
Rico Hohmuth (to 04/07)	Anja Zimmer (to 09/07)

Diploma Students

Roland Beyer (FZ Rossendorf)	Daniel Heinert
Michael Blech	Christian Herbst (Fritz-Lipmann Institut)
Tina Clauß	Matthias Hudl
Björn Hendrik Eisenhower (IPHT)	Carsten Jähne
Sebastian Engmann	Manuela Janietz
Matthias Grube	Hans Kleemann
Alexander Hartung	Roland Koim
Stefan Hechler	Peter Kossebau

124

Christian Kraft	Annett Schroeter
Matthias Kroll	Holger Sihler
Christiane Löffler	Johannes Slotta
Johanna Malsch	Mathias Steglich
Anne-Katrin Meyer	Tobias Steinbach
Thomas Müller	Michael Steinert
Michael Oertel	Markus Trautmann
Christian Pansow	Reinhard Volkmer
Robert Pietzcker	Alexander Voigt (Strahlentherapie)
Thomas Reicher	Martin Voitsch (BATOP GmbH)
Frank Richter	Mathias Weiß (OSRAM Opto)
Uwe Schinkel	Christian Wolf
Matthias Schmelz (IPHT)	Philipp Zeigermann
Torsten Schmidt	Gabriel Zieger

Technical Staff

Ulrich Barth	Gerald Lenk
Uta Bornkessel	Holger Mühlig
Uwe Eberhardt	Anja Mittelstädt (0,9)
Lutz Föllmer	Ralf Neubert
Silke Frunzke (0,75)	Stefan Prass
Kristina Garlipp (0,5)	Helga Rudolph
Dieter Hasler	Sylvia Stender (0,75)
Torsten Hilprecht	Matthias Thürk
Frank Jehn	Carmen Voigt

Einige Bilder aus dem Institutsleben

Lange Nacht der Wissenschaften am 16. November 2007

Wandertage des Instituts